Light-guided actin polymerization drives directed motility in protocells

Hideaki T. Matsubayashi[1,2,3†], Shiva Razavi[1,2,4,5], Yuhei O. Tahara[6,7], Oghosa H. Akenuwa[8], T. Willow Rock[1,2], Daichi Nakajima[9], Rina Otsuka-Yamaguchi[3], Hideki Nakamura[1,2,10,11], Daniel A. Kramer[12,13], Tomoaki Matsuura[14], Baoyu Chen[12,13], Christopher T. Lee[8], Makoto Miyata[6,7], Satoshi Murata[9], Shin-ichiro M. Nomura[9], Takanari Inoue[1,2†]

1 Department of Cell Biology, School of Medicine, Johns Hopkins University, 2 Center for Cell Dynamics, Institute of Basic Biomedical Sciences, Johns Hopkins University, 3 Frontier Research Institute for Interdisciplinary Sciences, Tohoku University, 4 Department of Biomedical Engineering, School of Medicine, Johns Hopkins University, 5 Department of Biological Engineering, School of Engineering, Massachusetts Institute of Technology, 6 Graduate School of Science, Osaka Metropolitan University, 7 The OMU Advanced Research Center for Natural Science and Technology, Osaka Metropolitan University, 8 Department of Molecular Biology, University of California San Diego, 9 Department of Robotics, Graduate School of Engineering, Tohoku University, 10 Hakubi Center for Advanced Research, Kyoto University, 11 Department of Synthetic Chemistry and Biological Chemistry, School of Engineering, Kyoto University, 12 Roy J. Carver Department of Biochemistry, Biophysics and Molecular Biology, Iowa State University, 13 Departments of Internal Medicine & Biophysics, University of Texas Southwestern Medical Center, 14 Earth-Life Science Institute, Institute of Science Tokyo

†Corresponding authors. Email: hideaki.matsubayashi.e1@tohoku.ac.jp, jctinoue@jhmi.edu

Abstract

Motility is a hallmark of life's dynamic processes, enabling cells to actively chase prey, repair wounds, and shape organs. Recreating these intricate behaviors using well-defined molecules remains a major challenge at the intersection of biology, physics, and molecular engineering. Although the polymerization force of the actin cytoskeleton is characterized as a primary driver of cell motility, building a minimal platform to test this process in protocellular systems has proven elusive. The difficulty lies in the daunting task of distilling key components from motile cells and integrating them into model membranes in a physiologically relevant manner. To address this, we developed a method to optically control actin polymerization with high spatiotemporal precision within cell-mimetic lipid vesicles known as giant unilamellar vesicles (GUVs). Within these active protocells, the reorganization of actin networks triggered outward membrane extensions as well as the unidirectional movement of GUVs at speeds of up to 0.43 µm/min, within the range of adherent mammalian cells. Notably, our findings reveal the requirements of both branched and linear actin networks for efficient membrane protrusions. This approach offers a powerful platform for unraveling the intricacies of cell migration, designing

39 synthetic cells with active morphodynamics, and advancing bioengineering applications, such as
40 self-propelled delivery systems and autonomous tissue-like materials.

Introduction

Motility is a fundamental property of cells across biological systems, from bacteria to large animals (*1–6*). By transcending the randomness and viscosity of the microscopic world, cells move toward their destination by extending membrane protrusions and by clutching onto the extracellular environment. In amoeboid cell migration, these processes are universally galvanized by actin polymerization (*7–12*). While hundreds of biomolecules are identified to be required for cell motility (*4*, *6*, *13*), a minimal list of biomolecular components sufficient for cell motility remains elusive. This primarily reflects the inherent difficulty of eliminating all biomolecules beyond the minimal set in the context of living cells.

Cell migration is driven by the coordination of forward movement, rear contraction, and adhesion/deadhesion of the cell edges (*4*, *6*, *14–16*). Among these processes, actin polymerization at the leading edge is a strong candidate for driving overall forward displacement. For instance, *Dictyostelium*, fish keratocyte, and human neutrophil retain their motility even after myosin contractility is compromised genetically (*17*, *18*) or pharmacologically (*19*, *20*). Cells also manage to migrate even without strong adhesions especially in confined conditions (*21*, *22*). Conversely, we and others have shown that synthetic activation of the Rho family GTPase Rac1, an upstream activator of the actin cytoskeleton, induces directional cell movements toward the site of stimulation (*23*, *24*). However, it is still unclear if Rac1-mediated actin polymerization alone is sufficient for cell motility in cellular settings, as Rac1 crosstalks with other Rho small GTPases such as RhoA and triggers other cytoskeletal activities including actomyosin contraction (*25*).

In a different context, molecules necessary for force generation by actin polymerization have been identified based on the motility reconstitution assay (*26–36*). These reports demonstrated that a mixture of purified cytoskeletal proteins, such as actin, Arp2/3, profilin, cofilin, and capping protein, can reconstitute the motility of *Listeria monocytogenes* bacteria using microspheres coated with actin nucleation-promoting factors (NPFs). Furthermore, a number of studies were conducted to reconstitute actin (*37*, *38*) and other cytoskeletons (*39–41*) inside cell-sized membrane-bound liposomes. These studies demonstrated that actin polymerization generates membrane deformations (*42–45*), revealed the roles of actin-binding proteins (*46–52*), and further showed that internal reactions can be regulated by light and external environmental factors (*52–55*). However, unidirectional motion by the cytoskeletal polymerization force has remained challenging. Moreover, non-invasive and non-constitutive—thus more physiological—induction of actin polymerization has yet to be achieved, particularly within cell-sized compartments that maintain proper membrane configuration. Building on these findings, we developed a minimal membrane-bound system in which actin polymerization can be locally

controlled and tested whether such an artificial cytoskeletal activity is sufficient to induce cell-like motility.

Results

Reversible and asymmetric light control of protein localization inside GUVs

To achieve *in vitro* reconstitution of cell motility, we previously developed active protocells where chemically inducible dimerization (CID) tools were used to polymerize actin based on a bacterial NPF inside giant unilamellar vesicles (GUVs) (*56*). While the previous system efficiently produced actin polymerization, outward membrane extension necessary for driving movement was not observed. We reasoned that this was due to a lack of fast turnover of NPF recruitment to the membranes. To aim for a physiologically relevant generation of protrusive force exerted against membranes, we adopted a light-inducible protein dimerization tool for controlling the localization of proteins of interest. Among optogenetic dimerization tools (*57*–*59*), we chose iLID-SspB (*60*) as its second-scale reversible binding kinetics match the turnover of leading-edge polarization (Supplementary Text 1), its blue-light activation is compatible with standard microscope setups, and its relatively small molecular size facilitates expression and purification of recombinant proteins.

We first set out to test light-induced dimerization of purified iLID and SspB in GUVs. In our construct, iLID was membrane-tethered, and blue light exposure triggered the Jα helix to extend, revealing the binding site for SspB. In the dark, iLID returned to its closed state, releasing SspB (Fig. 1A). We visualized the localization and the light responsiveness of the proteins by fusing iLID with YFP and SspB with mCherry (fig. S1A). To anchor iLID to the GUV membrane, we tested four different protein-lipid interaction strategies to mediate light-induced translocation, including coordination bonding, electrostatic, strong non-covalent, and covalent interactions (Fig. 1A, fig. S2, Supplementary Text 2) (*61*, *62*). Among these, the SNAP-tag/benzylguanine (BG)-conjugated lipid pair provided efficient iLID anchoring with minimal nonspecific membrane binding of SspB, and was therefore used for subsequent experiments.

When GUVs were made with 2% BG-conjugated lipid in the inner leaflet, iLID localized on the membrane, while SspB remained in the lumen in the dark (Fig. 1B). Upon blue light illumination of the entire GUV, SspB translocated to the membrane within 4 seconds (Fig. 1B, C). After switching back to the dark, SspB gradually dissociated from the membrane with a half-time of 61.2 ± 13.7 seconds. The time scale is consistent with AsLOV2-based optogenetic tools measured in cells (*58*). These data confirmed that iLID-SspB enables reversible control of protein localization in GUVs.

114
115 Next, we tested the potential for spatially asymmetric control of iLID-SspB interactions. When
116 light was applied locally to one side of the GUV, SspB accumulated at the illuminated site (Fig. 1D,
117 E). In the dark, dissociation proceeded with a half-time of 41.8 ± 7.1 seconds (fig. S3A). Despite
118 faster diffusion on artificial lipid membranes compared to cell membranes (*63*–*65*), localized light
119 stimulus created an asymmetric pattern of SspB in cell-sized vesicles (Fig. 1E, F, see
120 Supplementary Text 1). Furthermore, SspB precisely and repeatedly responded to the directional
121 change of blue light illumination (Figs. 1G, S3B, C, and Movie S1). Collectively, these results
122 demonstrated that the iLID-SspB system can direct asymmetric protein distribution at regions of
123 interest on the GUV membranes.
124
125 **Light-guided control of ActA**
126 Next, we sought to manipulate the actin cytoskeleton with the iLID-SspB system. Previous studies
127 have established that the rate of actin polymerization depends on the surface density of NPFs
128 (*26*, *30*, *35*) and that clustering of NPFs accelerates actin polymerization (*66*, *67*), as further
129 demonstrated by a reconstituted optogenetic VCA system (*68*). We have recently shown that
130 chemically-induced membrane recruitment of ActA, an N-WASP homolog NPF derived from *L.*
131 *monocytogenes*, induces actin polymerization on the membrane of GUVs, leading to symmetry
132 breaking (*56*, *69*). Thus, we first tested ActA with the iLID-SspB system. To identify an optimal
133 optogenetic configuration, we tested four ActA-SspB constructs with different SspB variants and
134 fusion orders (Supplementary Text 3). These constructs were evaluated based on actin
135 polymerization activity and light-dependent membrane recruitment, leading us to select ActA-
136 $SspB_{nano}$-mCherry (fig. S4). When supplemented with actin and Arp2/3, light-induced global
137 membrane recruitment of ActA-SspB led to the emergence of actin patches on the membrane,
138 consistent with our previous findings with a chemical input (*56*) (fig. S5). With local light, the ActA
139 distribution became asymmetric, albeit the directionality of actin pattern could not be
140 maintained. In most cases, actin patches diffused randomly out of the illuminated region and the
141 GUV lost actin directionality over time (fig. S6 and Movie S2).
142
143 **Reversible control of pVCA and light-guided actin polymerization**
144 For robust maintenance of actin asymmetry, we aimed to rapidly depolymerize actin filaments in
145 the non-illuminated area while strengthening actin polymerization in the illuminated region. To
146 promote depolymerization and turnover, we incorporated factors that facilitate the actin
147 turnover process, namely profilin, cofilin, and capping protein (*13*, *33*, *70*, *71*). In
148 ultracentrifugation assays, the combined addition of profilin, cofilin, and capping protein
149 increased the pool of G-actin, supporting the notion that these factors enhance actin turnover
150 (fig. S8A, B). To enhance polymerization in the illuminated regions within GUVs, we optimized
151 the polymerization module. Among several NPF constructs evaluated, GST-tagged N-WASP pVCA

152 (proline-rich region + VCA domain) showed the fastest actin polymerization in a bulk pyrene assay,
153 which monitors actin polymerization through the fluorescence increase of pyrene-labeled actin.
154 Notably, GST-pVCA maintained its activity when fused to SspB-mCherry, making GST-pVCA-SspB-
155 mCherry (pVCA-SspB-mCherry) a suitable light-inducible activator for our GUV system (Fig. 2A,
156 S1, S8C, D).
157
158 We then encapsulated this light-inducible pVCA-SspB-mCherry with actin (10% Alexa-647
159 labeled), Arp2/3, profilin, cofilin, and capping protein in GUVs (Fig. 2B). Upon illumination, pVCA-
160 SspB-mCherry rapidly translocated to the membrane, followed by the increase in membrane
161 actin signal. Notably, the actin signal increased gradually over time with a delay of several
162 minutes after pVCA translocation, consistent with light-induced actin polymerization (Fig. 2C, D,
163 Movie S3). In contrast, in the absence of either pVCA or light stimulation, no significant change
164 in membrane actin intensity was observed (Fig. 2D, fig. S9). When Arp2/3 was omitted, the
165 membrane actin signal showed a slight increase over time. This suggested that the G-actin
166 binding property of pVCA (*72*, *73*) increased the local concentration of actin at the periphery of
167 the membrane, albeit this effect was not as intense as Arp2/3-dependent actin assembly (Fig. 2D,
168 fig. S9). These data showed that light-dependent membrane accumulation of pVCA drives
169 Arp2/3-dependent actin enrichment on the GUV membrane.
170
171 Next, we employed pharmacological perturbations to probe the dynamics of membrane-
172 associated actin. Specifically, Latrunculin A sequesters G-actin to inhibit polymerization, whereas
173 Jasplakinolide stabilizes F-actin and suppresses depolymerization. To decouple actin dynamics
174 from optogenetic kinetics, iLID-SNAP was replaced with SsrA-SNAP, in which SsrA constitutively
175 binds SspB-fused pVCA independently of light (fig. S10A). Under these conditions, actin was
176 readily observed on the membrane (Fig. 2E, fig. S10B, C). Upon Latrunculin A treatment, the
177 membrane actin signal markedly decreased, confirming that the membrane actin signal derives
178 from F-actin. Conversely, Jasplakinolide increased membrane actin fluorescence, revealing
179 additional capacity for membrane actin accumulation beyond the steady-state level observed
180 under DMSO conditions (Fig. 2E, F, fig. S10D–F). Together, these results suggest that the
181 membrane-associated actin is maintained by a balance between ongoing actin assembly and
182 disassembly.
183
184 To further characterize the dynamics of pVCA and actin on the GUV membrane, we performed
185 fluorescence recovery after photobleaching (FRAP) analysis. pVCA-SspB-mCherry exhibited rapid
186 and near-complete fluorescence recovery, indicating that membrane-associated pVCA remains
187 highly mobile even during actin enrichment (Fig. 2G, fig. S11). In contrast, FRAP analysis of Alexa
188 Fluor 647–labeled actin showed slower and partial fluorescence recovery, suggesting the
189 presence of a less mobile F-actin fraction at the membrane (Fig. 2G, fig. S11). Notably, actin

190 fluorescence recovery was significantly reduced in the absence of regulatory factors, profilin,
191 cofilin, and capping protein (fig. S11A, E), indicating that membrane-associated actin exists in a
192 dynamic steady state regulated by these factors.
193
194 To examine the ultrastructure of the actin network, we performed negative staining electron
195 microscopy (EM). For this analysis, small unilamellar vesicles (SUVs; 50–150 nm in diameter)
196 containing 2% benzylguanine-modified lipids (fig. S12A) were used to recruit pVCA-SspB-mCherry
197 to their outer surface via SsrA-SNAP. EM images revealed dense actin filament networks (Fig. 2H,
198 fig. S12B–D) with frequent Y-junctions, characteristic of Arp2/3-mediated branching (fig. S12B),
199 providing structural evidence for Arp2/3-dependent actin polymerization.
200
201 Next, we tested the reversible actin regulation by pVCA-SspB-mCherry. As shown in Fig. 2I and J,
202 both pVCA-SspB-mCherry and actin displayed reversible and repetitive changes in membrane
203 intensity in response to blue light switching (Movie S4). Notably, once switched to the dark,
204 pVCA-SspB-mCherry quickly dissociated from the membrane, whereas actin decreased its
205 membrane intensity at a relatively slower rate (fig. S13). Taken together, these results suggested
206 that the polymerization state is reversible in our system and that the balance between
207 polymerization and depolymerization can be controlled by light.
208
209 **Asymmetric and spatially controlled actin polymerization**
210 The asymmetric distribution of NPFs and actin polymerization are fundamental features of
211 directed cell migration (*9*, *74*, *75*). Thus, we next tested whether locally targeted pVCA could
212 establish asymmetric actin polymerization (Fig. 3A). As shown in Fig. 3B, C, and fig. S14A, pVCA
213 showed asymmetric patterning toward the localized light stimulus (Movie S5). About 5 minutes
214 after pVCA translocation, the actin signal also increased from the illuminated region and created
215 an asymmetric pattern. Line scans along the GUV perimeter indicated that pVCA responded
216 rapidly with a narrow peak, whereas actin accumulated more gradually and exhibited a broader
217 distribution. These results suggest that actin polymerization requires a finite time to initiate and
218 propagate, and once filaments are formed they remain associated with the membrane for a
219 longer duration (fig. S14B). With continuous local illumination, both pVCA and actin maintained
220 stable polarity for more than 100 minutes (Fig. 3B, C, S14A, B, Movie S5). Notably, at later time
221 points, the actin signal appeared as two lines in the latter time points in the kymograph. This
222 likely reflects reduced lateral diffusion of membrane-associated actin filaments, combined with
223 gradual photobleaching of Alexa Fluor 647-labeled actin under repeated blue-light excitation. We
224 next tested whether the direction of actin polymerization could be reversibly reprogrammed.
225 After establishing an asymmetric actin pattern with a local light on the right side of the vesicle,
226 we reversed it back to the dark mode and subsequently applied new light on the left. Both pVCA
227 and actin rapidly re-polarized toward the new stimulation site (Fig. 3D, E, and Movie S6). Together,

228 these results demonstrate that the light-inducible pVCA system enables reversible and spatially
229 reconfigurable polarization of actin networks.
230
231 Importantly, when locally illuminated, the front membrane of some GUVs moved toward the
232 illuminated direction (fig. S14C), albeit occasionally (2 out of 7 instances). We speculate that
233 characteristics inherent to the GUV system–such as surface-to-volume ratio of individual GUVs,
234 surface density of pVCA, and the ratio of Arp2/3 to capping protein (*33*, *76*), either individually
235 or in combination, may determine whether productive protrusive behavior emerges.
236
237 **mDia1-driven actin polymerization drives membrane protrusions in cells**
238 To enhance forward membrane protrusion, we next sought to reinforce actin polymerization. At
239 the leading edge of migrating cells, two major actin nucleators, namely Arp2/3 and formin,
240 coordinate the forward extension of the plasma membrane (*77–79*). While Arp2/3 stays at the
241 branch points of the actin filaments and does not engage in the incorporation of monomeric actin
242 into the growing ends, formin continuously binds to the growing ends and actively recruits
243 profilin-actin complexes to the elongating tips. Consequently, one subtype of formin, mDia1,
244 accelerates actin polymerization 4–5-fold (*80*, *81*) and drives motility 6–23 times faster than
245 Arp2/3 in *in vitro* motility assays using functionalized beads (*30*, *28*, *31*). Furthermore, a
246 theoretical study suggests that actin polymerization perpendicular to the membrane,
247 characteristic of formin-driven filopodia formation, more efficiently transduces the
248 polymerization force to advance the membrane (*82*). Therefore, we reasoned that the
249 integration of mDia1 could enhance protrusive activity.
250
251 To test whether mDia1 promotes membrane protrusion, we first used living cells and performed
252 a plasma membrane recruitment assay (Fig. S15A) (*83–85*). More specifically, we took FH1-FH2-
253 DAD domains from mDia1 as a constitutively active form (*86*) and recruited it to the plasma
254 membrane by the CID system. As shown in fig. S15B–H, YF-mDia1 translocation induced filopodia-
255 like protrusions (fig. S15B–H). These protrusions were positive for Lifeact signal and showed
256 coiling motions with their elongating tips labeled with YF-mDia1 (fig. S15D), consistent with
257 formin-dependent filopodia elongation (*87–90*). Together, these data suggest that membrane
258 recruitment of mDia1 generates an actin-dependent protrusive force on the membrane.
259
260 **mDia1-driven actin polymerization drives forward movement of GUVs**
261 We then constructed the light-inducible version of mDia1 (mCherry-SspB-mDia1) for *in vitro*
262 reconstitution (Fig. S1). Pyrene actin assays suggested that mDia1 had an effect of increasing the
263 initial rate of actin polymerization (Fig. S8E, F). We encapsulated mCherry-SspB-mDia1 with iLID-
264 YFP-SNAP, actin (10% Alexa-647 labeled), profilin, and cofilin in GUVs. Upon local recruitment of
265 mDia1, some vesicles showed gradual drift toward the stimulated direction, suggesting that

266 mDia1-generated actin polymerization can produce protrusive forces in the reconstituted lipid
267 vesicles (fig. S16A, B). However, the response was modest and difficult to detect.
268
269 Because mDia1 alone produced only limited protrusive activity, we added pVCA-SspB, Arp2/3,
270 and capping protein to better mimic actin network organization of migrating cells (Fig. 4A).
271 Strikingly, this full component system (pVCA + mDia1) produced robust directional movement
272 toward light stimulation in 18 out of 22 GUVs (Fig. 4B–D, fig. S16C, Movie S7, S9, S10). Polarized
273 actin accumulation at the illuminated side preceded membrane displacement, consistent with
274 actin polymerization driving forward protrusion (Fig. 4B, Movie S7). The vesicle continued to
275 move steadily for an hour until the light was turned off (Fig. 4B, D, Movie S7). Furthermore, when
276 we shifted the position of the blue light, the signals for mDia1, pVCA, and actin reoriented,
277 causing the vesicle to move in the new direction, resembling chemotactic reorientation in
278 migrating neutrophils (Fig. 4B, D, Movie S7). The speed of pVCA/mDia1 dual system was
279 approximately threefold higher than that of mDia1 GUVs (Fig. 4G, H, S16B–C). The distance the
280 front side membrane moved in 30 minutes was also significantly longer in pVCA + mDia1 GUVs
281 (Fig. 4I). Furthermore, membrane recruitment of mDia1 and pVCA occasionally showed local
282 protrusions, suggesting the generation of protrusive force (fig. S17, Movie S8). Together, these
283 results indicate that mDia1-driven actin polymerization generates protrusive force that is
284 substantially enhanced by cooperative activity with pVCA and Arp2/3.
285
286 When mDia1 and pVCA were replaced with an equivalent amount of mCherry-SspB, vesicles did
287 not move even with the local blue light illumination (fig. S18A). In addition, the kymograph
288 analysis revealed that the timing and direction of membrane protrusions correlated with actin
289 intensity and its polarity, consistent with actin-driven dynamics (Fig. 4E, F). Notably, the
290 kymographs also revealed that protrusions at the front often coincide with retractions at the rear.
291 Corroborating this, the actin sequestering compound Latrunculin A and the formin inhibitor
292 SMIFH2 substantially compromised the motion of vesicles (Fig. 4J). Furthermore, deletion of the
293 DAD domain from mDia1, which is responsible for efficient actin nucleation by mDia1 (*91*),
294 abolished this motion (Fig. 4J). Together, these results indicate that membrane protrusion and
295 motion of the vesicles are driven by actin polymerization.
296
297 **The pVCA–mDia1 combination forms a fast-turnover, actively polymerizing actin network**
298 To elucidate the mechanistic basis of the distinct actin architectures generated by pVCA, mDia1,
299 and the pVCA–mDia1 dual system and their contributions to vesicle motion, we combined
300 ultrastructural, pharmacological, and FRAP analyses of reconstituted actin networks.
301
302 To examine ultrastructure, we performed EM on actin assemblies formed on SsrA-coated SUVs.
303 Although assemblies deposited onto a solid support may not fully represent filament

organization within GUVs, micrometer-scale filaments were observed under all conditions, with the highest filament density observed when pVCA was used as the sole NPF (fig. S12D, E). However, filament density alone did not explain the observed differences in vesicle motion, underscoring the importance of actin network dynamics.

To probe network dynamics, we examined the pharmacological responses of actin assemblies in a system where NPFs were constitutively tethered to the GUV membrane via SsrA. Consistent with EM observations, pVCA generated the highest basal level of membrane-associated actin but showed only modest additional F-actin accumulation upon Jasplakinolide treatment (fig. S10B–F). In contrast, mDia1-driven assemblies exhibited a progressive increase in membrane-associated actin in response to Jasplakinolide, with the most pronounced effect observed in the combined pVCA-mDia1 system (fig. S10E, F), consistent with the enhanced polymerization capacity of the dual condition observed in bulk pyrene–actin assays (fig. S8F). Notably, Jasplakinolide treatment of mDia1 and pVCA-mDia1 GUVs was occasionally accompanied by outward membrane deformation, consistent with polymerization-generated forces acting on the membrane (fig. S10G). Moreover, the pVCA-mDia1 dual system was least susceptible to Latrunculin A, indicating a shift in network behavior toward sustained polymerization (fig. S10E, F).

FRAP analysis further distinguished network dynamics. pVCA-driven actin networks displayed rapid fluorescence recovery, suggesting highly dynamic actin turnover (fig. S11C, E). In contrast, actin assemblies generated by mDia1 showed minimal fluorescence recovery of actin and mDia1 itself (fig. S11B–E). This slow recovery is consistent with processive filament elongation at the membrane, where mDia1 remains persistently associated with growing barbed ends. Importantly, the pVCA–mDia1 dual system—despite exhibiting strong Jasplakinolide-induced actin accumulation—retained rapid fluorescence recovery in FRAP (fig. S11C, E), indicating that the dual network maintains dynamic turnover while sustaining high polymerization activity.

Together, these observations indicate that the pVCA–mDia1 system exhibits high polymerization capacity and rapid turnover, properties potentially well suited for efficient force generation and directional vesicle movement.

Deformation and adhesion of GUVs

Quantitative analysis revealed that the initial velocity of each GUV was strongly correlated with its net displacement after 30 minutes (R = 0.89; fig. S19A). In addition, displacement showed a moderate positive correlation with vesicle diameter, suggesting that larger vesicles can accommodate greater chemical and cytoskeletal resources and may also be more favorable for generating light-induced asymmetry. In contrast, vesicles showing membrane localization of

342 pVCA and mDia1 prior to blue light illumination tended to exhibit smaller displacement. This
343 suggests that nonspecific membrane binding limits the light-dependent establishment of
344 asymmetry (fig. S19B, C).
345
346 We next analyzed changes in velocity and vesicle shape. The vesicles initially moved at an average
347 velocity of 0.43 µm/min, but their speed gradually decreased over time (Fig. 4G, H, fig. S16C).
348 Concomitant with this deceleration, the contact area of the bottom side of the vesicles
349 progressively increased during the movement, stabilizing the vesicles in a dome-like shape (Fig.
350 4C, K). This increase in the contact area was not seen in the GUVs when pVCA and mDia1 were
351 replaced with mCherry-SspB (fig. S18B). Thus, we speculate that the contact to the bottom
352 substrate was induced by the protrusive reaction and that the adhesion and the concomitant
353 deformation led to cumulative tension increase (*92*) which in turn counteracted the protrusive
354 force. The force exerted by actin polymerization may not be enough to detach the GUV from the
355 BSA-coated glass substrate. This is consistent with the observation that an initial contact site
356 remained adherent even in a GUV that traveled farthest (Fig. 4K, fig. S20B, C, Movie S9, S10).
357 Additionally, actin recycling in the system may be insufficient and the force gradually diminishes
358 over time (*71*). Despite these potential resisting factors, the combination of mDia1 and pVCA
359 induced movement consistently (Fig. 4, fig. S16C, S20). Together, these observations support the
360 conclusion that asymmetric actin polymerization mediated by pVCA–mDia1 is sufficient to drive
361 forward vesicle movement under the tested conditions.
362
363 **Computational modeling of actin network dynamics underlying membrane deformation**
364 To dissect the mechanisms underlying actin-driven membrane deformation, we constructed a
365 computational model of actin network dynamics in a minimal vesicle system. We hypothesized
366 that membrane deformation could arise from intrinsic mechanical bracing within the actin
367 network. Accordingly, we considered two candidate mechanisms: Arp2/3-dependent network
368 organization and frictional interactions between actin filaments (*93*, *94*). The model was
369 implemented using the actin-network simulation framework Cytosim (*95*) and coupled to a
370 deformable membrane (*96*, *97*) (Supplementary Text 4 and Methods).
371
372 The simulations captured distinct NPF-dependent behaviors (fig. S21A, B, Movie S11, S12). pVCA
373 produced short, branched filaments that frequently detached from the membrane, whereas
374 mDia1 drove rapid filament elongation while remaining membrane-associated. Without inter-
375 filament steric interactions, the pVCA + mDia1 condition yielded marginal but reproducible
376 forward membrane motion (fig. S21A, C, Movie S11), indicating cooperativity between mDia1
377 and pVCA. Incorporating inter-filament interactions resulted in robust membrane deformation
378 (fig. S21B, D, Movie S12), with extension increasing in the order pVCA < mDia1 < pVCA+mDia1,
379 consistent with experiments (Fig. 4G–I). These results support a minimal internal bracing

380 mechanism in which membrane-anchored polymerization, Arp2/3-dependent branching, and
381 inter-filament interactions collectively generate protrusive force.
382
383 The simulations also revealed substantial retrograde flow of actin filaments (fig. S21A, B, Movie
384 S11, S12). This provides a mechanistic explanation for why the observed vesicle motility (0.1–1.0
385 µm/min, Fig. 4G–J, fig. S16) is more than an order of magnitude slower than the actin
386 polymerization rate (1–10 µm/min) (*80*, *81*) and neutrophil migration (~10 µm/min) (*98*).
387 Incorporating additional backing mechanisms that provide mechanical resistance to the actin
388 network, such as external anchoring or confinement (*21*, *22*), is therefore predicted to enhance
389 protrusive efficiency and bridge minimal synthetic systems toward cellular modes of amoeboid
390 migration.
391

392 # Discussion

393 In the present study, we developed a fully reconstituted system to achieve light-guided
394 directional movement in a protocell. We leveraged mDia1-mediated actin polymerization to
395 establish the forces that drive movement. Our findings not only corroborate recent cell biological
396 findings on formin's significant roles in cell migration (*87*, *98–103*) but also show that the mDia1-
397 mediated actin polymerization can drive the forward movement of lipid vesicles in a minimal,
398 reconstituted system, overcoming challenges thus far posed by genetic redundancy and cellular
399 complexity. Formin-mediated actin polymerization exhibits several unique features compared to
400 free barbed end elongation in Arp2/3-dependent polymerization, including processive
401 elongation (*31*, *80*), accelerated polymerization rate (*80*, *81*), rotation, and coiling motion (*89*, *90*,
402 *104*). These characteristics could contribute to the effective propulsion of the vesicle. Remarkably,
403 our minimal system further indicated a functional interplay between pVCA and mDia1. Although
404 further investigation is required, this cooperative effect likely arises from coordination between
405 the two nucleators: mDia1 generates mother filaments required for Arp2/3 nucleation, and, in
406 turn, Arp2/3-mediated branching increases the number of growing ends available for mDia1
407 elongation (*100*, *101*). To further elucidate the mechanical coupling to force generation and
408 membrane protrusion, unveiling the nanoscopic architecture of the actin network in the
409 migrating protocell will be crucial. Our protocell approach, which bridges the gap between
410 cellular and biochemical domains, opens new avenues for comprehensively interrogating
411 modules of cellular motility.
412
413 We achieved a GUV displacement speed in the range of 0.1–1.0 µm/min, which is comparable to
414 the migration rates of typical fibroblasts (*105*) and other adherent cells including those that
415 competed in the World Cell Race (*106*). How could we make the movement even faster? *L.*
416 *monocytogenes* and NPF-coated beads in purified cytoskeletal protein solution typically move in

417 the range of 1–15 µm/min (*27*, *28*, *30–33*). Some adherent cells can migrate at 5 µm/min even
418 when actomyosin contractility is inhibited (*19*). We propose three possible ways to make artificial
419 cell migration faster. First, increasing actin concentration (*81*, *107*) and integrating additional
420 factors, such as VASP (*108*), Fascin (*109*), and NPFs (*67*, *110*), could accelerate the rate of actin
421 polymerization. Secondly, optimizing membrane tension could enhance the deformability of the
422 lipid membrane, akin to the malleable structures observed in motile cells, thereby potentially
423 promoting more efficient protrusion and motility (*50*, *111*). Finally, fine-tuning adhesion could
424 enhance migration efficiency as many cells exhibit a preference for an optimal adhesion range,
425 where both insufficient and excessive adhesion can hinder motility (*112*, *113*).
426
427 Interestingly, the phenotypes of mDia1 membrane recruitment differed between cells and GUVs.
428 In cells, mDia1 produced filopodia-like thin protrusions (fig. S12), whereas in GUVs, it pushed the
429 lipid membrane as a continuous plane structure on a much broader scale than filopodia (Fig. 4,
430 fig. S13–16). Since living cells tend to have higher membrane tension than liposomes (*114*), it
431 may appear counterintuitive that the cell membrane was more susceptible to mDia1-induced
432 local deformation. One possible explanation is that, in cells, endogenous proteins might work in
433 concert with mDia1 to amplify local membrane deformation and form long filopodia-like
434 protrusions (*100*, *115*). Alternatively, localized defects in membrane tension could predispose
435 certain areas to form thin protrusions (*116*). Additionally, cytoskeleton-bound transmembrane
436 proteins impede tension propagation in cells (*117*). Furthermore, the nuclear accumulation of
437 mDia1 in cells (fig. S12) could reduce its effective concentration and cause a heterogeneous
438 distribution on the cell membrane, resulting in focused protrusive force in regions with high
439 mDia1 concentration, similar to how pVCA-driven finger-like protrusions are formed in liposomes,
440 as demonstrated by Gat *et al.* (*118*). Since our light-inducible actuators are genetically encodable,
441 the same molecular toolkit can be deployed in both GUVs and living cells—providing a unified
442 platform to dissect cellular morphodynamics.
443
444 We have recently shown that chemically-induced membrane recruitment of ActA, an NPF derived
445 from *L. monocytogenes*, and subsequent global actin polymerization lead to eccentricity in the
446 shape of GUVs (*56*). We noted a difference in membrane deformation between the CID and LID
447 systems, as the CID could induce a clear membrane deformation given a global, non-directional
448 input. This difference could be attributed to the variations in cytoskeletal proteins and input
449 signals between the two systems. In the present study, we have incorporated profilin, cofilin, and
450 capping proteins. Since these proteins accelerate actin depolymerization (fig. S8B), they may
451 render the actin network more plastic rather than exerting force to deform the membrane.
452 Consistent with this, stabilization of F-actin by Jasplakinolide occasionally resulted in outward
453 membrane deformation in GUVs containing mDia1 or the pVCA–mDia1 combination (fig. S10G).
454 Moreover, the binding kinetics of iLID-SspB (k_{on} =1.2 × 10^3 $M^{-1}s^{-1}$, k_{off} =1.1 × 10^{-3} s^{-1}, K_d = 0.8 µM)

455 substantially differ from those of FKBP-FRB (k_{on} =1.9 × 10^6 $M^{-1}s^{-1}$, k_{off} =2.2 × 10^{-2} s^{-1}, K_d = 12 nM)
456 (*60*, *119*, *120*). This may result in different reaction dynamics between actin cytoskeleton and the
457 lipid membrane.
458
459 Our finding that internal cytoskeletal force can drive the unidirectional motion of lipid vesicles
460 offers avenues to reverse-engineer cell motility. Although we used light as an input, asymmetric
461 actin polymerization may be achievable with chemical inputs with consideration of binding
462 affinity (*83*, *121*), transmembrane signal transduction mechanisms (*122*), and self-organized
463 pattern formation (*123*–*127*). For sustained motility, it will be important to incorporate other
464 migratory forces—reconstructing myosin contractility at the rear (*128*) and regulating
465 adhesion/de-adhesion turnover (*119*, *129*) in concert with actin polymerization. Furthermore,
466 integrating synthetically engineered molecules (*81*, *130*, *131*) could enhance–motility even
467 beyond the limits of natural systems. Achieving synthetic motility in GUVs could be a step toward
468 future developments in active therapeutic agents, self-organizing artificial tissues, and synthetic
469 neural circuits.

Materials and Methods

Reagents

ATP was purchased from Gold Biology (A-081) or Nacalai Tesque (01072-82), prepared as 100 mM solution in 100 mM Tris-HCl (pH 7.4 at RT), and stored at -20°C. Creatine phosphate was purchased from Gold Biotechnology (C-323-5) or Oriental Yeast (45180000), prepared as 1 M solution in PBS (Gibco 10010-023), stored at -20°C. Creatine kinase was purchased from Sigma-Aldrich (10127566001) or Oriental Yeast (46430003), prepared as 40 µM solution in buffer V (50 mM HEPES-NaOH (pH 7.5), 150 mM NaCl, 7 mM β-mercaptoethanol, 10% glycerol), snap-frozen, and stored at -20°C. Flavin mononucleotide (FMN) was purchased from TCI (R0023) and Wako (06500171), freshly prepared as 600 µM solution in Milli-Q water before iLID expression. Alexa Fluor 647 C2 Maleimide (A20347) and Pierce™ Glutathione Agarose (16100) were purchased from Thermo Fisher Scientific. Hexadecane (H6703), Silicone oil (378348), and SMIFH2 (S4826) were purchased from Sigma-Aldrich. Latrunculin A was purchased from Wako (125-04363). Jasplakinolide was purchased from Cayman Chemical Company (11705). Benzylguanine-PEG2000-DSPE was prepared and purified as previously described (*61*). POPC (1-palmitoyl-2-oleoyl-glycero-3-phosphocholine, 850457), POPS (1-palmitoyl-2-oleoyl-sn-glycero-3-phospho-L-serine, 840034), 18:1 DGS-NTA-Ni (1,2-dioleoyl-sn-glycero-3-[(N-(5-amino-1-carboxypentyl)iminodiacetic acid)succinyl] (nickel salt), 790404), 18:1 PE-PEG2000-benzylguanine (1,2-dioleoyl-sn-glycero-3-phosphoethanolamine-N-[benzylguanine(polyethylene glycol)-2000], 880137), and 18:1 Biotinyl Cap PE (1,2-dioleoyl-sn-glycero-3-phosphoethanolamine-N-(cap biotinyl) (sodium salt), 870273C) were purchased from Avanti Polar Lipids as chloroform solution. Actin (AKL99), pyrene labeled actin (AP05), Arp2/3 (RP01P), Profilin (PR02), Cofilin (CF01), were purchased from Cytoskeleton. Strep-Tactin XT (2-4010-010, discontinued) resin, Strep-Tactin XT 4Flow (2-5010-010) resin, and purified Strep-Tactin protein were purchased from IBA. Ni-NTA agarose (30210) was purchased from Qiagen. Amylose resin (E8021S) was purchased from New England BioLabs.

Plasmid construction

pQE80L-6×His-MBP-TEVprorease(S219V)

Ser219Val mutation (*132*) was introduced by PCR with the template plasmid gifted from Dr. Yubin Zhou and the primer set of fwd: 5'-TGGTGAAACCTGAAGAACCTTTT-3' and rev: 5'-TTCACCATGAAAACTTTATGGCC-3'. TEV prorease (S219V) was then PCR amplified with the primer set of fwd: 5'-AATTGAGCTCGATGAGCGGCCTGGTGC-3' and rev: 5'-AATTGGATCCTTATTGCGAGTACACCAATTCATTCATG-3' and inserted between SalI and BamHI sites of pQE-80L MBP-SspB Nano plasmid (Addgene #60409) by using restriction digestion and T4 ligase ligation process.

pQE80L-6×His-MBP-TEVsite-mCherry-SspB(micro)

EYFP-2×SAGG linker was PCR amplified from the template plasmid YFP-FKBP (*133*)with the primer set fwd: 5'- GTATTTTCAGGGATCGCCGCTAGCGCTACCGG-3' and rev: 5'-TCGGGGAGCTGGATCCTCCGCCAGCGCTGC-3' and inserted into BamHI site of pQE-80L MBP-SspB Nano plasmid (Addgene #60409) by using Gibson assembly. EYFP part was then replaced with mCherry from pmCherry-C1 (Clontech) by restriction digestion and T4 ligase ligation process with AgeI and BsrGI. Arg73 of SspB was mutated to Gln by PCR with the primer set fwd: 5'-AACGCCCagTTTAAGGGCGTGTCTCGT-3' and rev: 5'- CTTAAActGGGCGTTGAACTGGATAA-3'.

pGEX-2T-GST-3Csite-TEVsite-6×His

Two sets of oligo DNA pairs were designed to introduce 3C protease cleavage site, TEV protease cleavage site, and 6×His tag (1st set, fwd: 5'-GGTTCCGCGTGGATCTGGTCTTGAGGTGCTCTTTCAGGGACCCGGCAGTCTCGAGGGTCTGTACAAGCGAATTCAG-3', rev: 5'-CTGAATTCGCTTGTACAGACCCTCGAGACTGCCGGGTCCCTGAAAGAGCACCTCAAGACCAGATCCACGCGGAACC-3'. 2nd set, fwd: 5'-TACAAGCGAATTCAGGAGAACCTCTACTTTCAAAGCGATCATCATCATCATCATCACTAAAAATTCATCGTGACTG-3' and rev: 5'-CAGTCACGATGAATTTTTAGTGATGATGATGATGATGATCGCTTTGAAAGTAGAGGTTCTCCTGAATTCGCTTGTA-3' (underlines indicate overhang sequences)). To anneal oligo DNAs individually, 0.5 µM each DNAs were mixed in 1× T4 Ligase buffer (NEB, B0202S) and heated at 85°C for 10 min and cooled 5°C per 2 min down to 40°C. pGEX-2T, which was kindly gifted from Dr. Miho Iijima, was digested by BamHI and EcoRI and assembled with the two annealed DNA fragments by Gibson assembly.

pGEX2T-GST-pVCA-3Csite-SspB(micro)-mCherry-TEVsite-6×His

To first construct pGEX2T-GST-pVCA-3Csite-TEVsite-6×His, pVCA (proline rich region and VCA domain) of human N-WASP was PCR amplified with the primer set fwd: 5'-CAGTCTCGAGGGAGGTGTTGAAGCTGTTAAAAATGA-3' and rev: 5'-TCCTGAATTCCGTCTTCCCACTCATCATCATCCTC-3' and inserted between XhoI and EcoRI site of pGEX-2T-GST-3Csite-TEVsite-6×His by using restriction digestion and T4 ligase ligation. Then, SspB(micro)-mCherry was PCR amplified with the primer set fwd: 5'-TGAGTGGGAAGACGGAATTGGGCAGTCGACGGTACCGCG-3' and rev: 5'-GTAGAGGTTCTCCTGAATTCCCTTGTACAGCTCGTCCATGCC-3' and inserted in the EcoRI site of pGEX2T-GST-pVCA-3Csite-TEVsite-6×His by Gibson assembly.

pET28-2×Strep-iLID-EYFP-MARCKS

First, pET28-2×Strep-iLID-6×His was constructed as follows. iLID sequence was cut out from the pLL7.0: Venus-iLID-Mito (Addgene #60413) by NheI and EcoRI and inserted between NheI and EcoRI sites of pET28-2×Strep-tag gifted from Dr. Kanemaki by using restriction digestion and T4 ligase ligation. Then, to construct pET28-2×Strep-iLID-EYFP-6×His, EYFP was PCR amplified from pEYFP-C1 (Clontech) with the primer set fwd: 5'-AATTGTCGACATGGTGAGCAAGGGCGAG-3' and rev: 5'-AATTGCGGCCGCCTTGTACAGCTCGTCCATGC-3' and inserted between SalI and NotI sites of pET28-2×Strep-iLID-6×His by restriction digestion and T4 ligation. MARCKS-ED fragment was constructed by oligo annealing (1st set fwd: 5'-GTACAAGGGAAGTGCTGGTGGTAAAAAGAAAAAGAAGCGCTTTTCCTTC-3' and rev: 5'-TTCTTGAAGGAAAAGCGCTTCTTTTTCTTTTTACCACCAGCACTTCCCTT-3', 2nd set fwd: 5'-AAGAAGTCTTTCAAGCTGAGCGGCTTCTCCTTCAAGAAGAACAAGAAGTA-3' and rev: 5'-GTACTACTTCTTGTTCTTCTTGAAGGAGAAGCCGCTCAGCTTGAAAGAC-3') and inserted into BsrGI site of pET28-2×Strep-iLID-EYFP-6×His.

pET28-2×Strep-iLID-EYFP-SNAP

SNAP tag sequence was PCR amplified from the template Phage-ubc-nls-ha-tdMCP-SNAP, a kind gift from Dr. Bin Wu, with the primer set fwd: 5'-AATTTGTACAAGTCTGCTGGCGGAAGCGCTGGAGGCAGCATGGACAAAGACTGCGAAATGAAGC-3' and rev: 5'-AATTGCGGCCGCTTAACCCAGCCCAGGCTTG-3' and inserted between BsrGI and NotI of pET28-2×Strep-iLID-EYFP-MARCKS by restriction digestion and T4 ligation.

pET28-2×Strep-SsrA-SNAP

The plasmid was constructed by replacing the iLID-EYFP part of pET28-2×Strep-iLID-EYFP-SNAP with the sequence containing SsrA peptide (AANDENY). A set of oligo DNA (5'-AGCGGGTGCCGCTAGCGCAGCGAACGACGAAAATTACGGACCGGTCGGTCTGTACAAGTCTGCTGG-3' and 5'-CCAGCAGACTTGTACAGACCGACCGGTCCGTAATTTTCGTCGTTCGCTGCGCTAGCGGCACCCGCT-3', (underlines indicate SsrA peptide region)) was annealed and inserted between NheI and BsrGI site of pET28-2×Strep-iLID-EYFP-SNAP by Gibson assembly.

mCherry-SspB(micro) (Clontech C1)

SspB(micro) sequence was PCR amplified from pQE80L-6×His-MBP-TEVsite-mCherry-SspB(micro) with the primer set fwd: 5'-GAACAGTACGAACGCGCC-3' and rev: 5'-AATTCTCGAGGACCACCAGCACTACCACCAGCACTACCACCAGCACTACCACCAGCACTACCACCAGCAC TACCAATATTCAGCTCGTCATAGATT-3' and inserted between BsrGI and XhoI sites by restriction digestion and T4 ligation. A silent mutation was introduced to BamHI site upstream of SspB by inverse PCR with the primer set fwd: 5'-GAGGATCtAGCTCCCCGAAACGCCCT-3' and rev: 5'-GGGAGCTaGATCCTCCGCCAGCGCTG-3'

583
584 pQE80L-MBP-TEVsite-mCherry-MCS
585 mCherry sequence was PCR amplified from pmCherry-C1 (Clontech) with the primer set fwd: 5'-
586 GTATTTTCAGGGATCGCTAGCGCTACCGGTC-3' and rev: 5'-
587 TCAGCTAATTAAGCTATCAGTTATCTAGATCCGGTGGATC-3' and inserted between BamHI and
588 HindIII sites of pQE-80L MBP-SspB Nano by Gibson assembly.
589
590 2×Strep-mCherry-MCS
591 mCherry sequence was PCR amplified from pmCherry-C1 (Clontech) by the primer set fwd: 5'-
592 AGCGGGTGCCGCTAGTCATATGGGTACGCTAGCGCTACCGGTCG-3' and rev: 5'-
593 GGTGGTGGTGCTCGATCAGTTATCTAGATCCGGTGGATCC-3' and inserted between NheI and XhoI
594 sites of pET28-2×Strep-tag by Gibson assembly.
595
596 2×Strep-MBP-TEVsite-mCherry-MCS
597 MBP-TEVsite-mCherry-MCS was PCR amplified from the template pQE80L-MBP-TEVsite-
598 mCherry-MCS with the primer set fwd 5'-CAAATGGGTCGGATCGACGGATCTAAAATCGAAGAAGG-
599 3' and rev: 5'-GGTGGTGGTGCTCGATCAGTTATCTAGATCCGGTGGA-3' and inserted between
600 BamHI and XhoI sites of pET28-2×Strep-tag by Gibson assembly.
601
602 pCold-6×His-2×Strep-MBP-TEVsite-mCherry-SspB(micro)-mDia1(FH1-FH2-DAD)
603 A DNA fragment 2×Strep-MBP-TEVsite-mCherry was PCR amplified from 2×Strep-MBP-mCherry-
604 MCS with the primer set fwd: 5'-TCGAAGGTAGGCATATGGGCTGGTCTCACCC-3' and rev: 5'-
605 ACAGCTCGTCCATGCCG-3'. The other DNA fragment SspB(micro) was PCR amplified from
606 mCherry-SspB(micro) (Clontech C1) with the primer sets fwd: 5'-GCATGGACGAGCTGTACAAG-3'
607 and rev: 5'-TCATTCTTGGCCATAGCTTGAGCTCGAGGACC-3'. pCold-mDia1, which was a kind gift
608 from Dr. Roberto Dominguez, was digested by NdeI and assembled with the two DNA fragments
609 by Gibson assembly.
610
611 pET28-2×Strep-mCherry-SspB(micro)-mDia1(FH1-FH2-DAD)
612 mCherry-SspB(micro)-mDia1(FH1-FH2-DAD) was cut out from pCold-6×His-2×Strep-MBP-
613 TEVsite-mCherry-SspB(micro)-mDia1(FH1-FH2-DAD) by AgeI and BamHI and inserted between
614 AgeI and BamHI sites of 2×Strep-mCherry-MCS by restriction digestion and T4 ligation.
615
616 pET28-2×Strep-mCherry-SspB(micro)-TEVsite-6×His
617 A DNA fragment mCherry-SspB(micro) was PCR amplified from mCherry-SspB(micro) (Clontech
618 C1) with the primer set fwd: 5'-AGCGGGTGCCGCTAGCGGACCGGTCGCCACCATG-3' and rev: 5'-
619 AAAGTAGAGGTTCTCAGATCCGGTGGATCCCGG-3'. The other fragment containing TEV cleavage
620 site was made by oligo annealing of a set of DNA 5'-

621 GAGAACCTCTACTTTCAAagcgatgTCGAGCACCACCACC-3’ and 5’-
622 GGTGGTGGTGCTCGAcatcgctTTGAAAGTAGAGGTTCTC-3’. These fragments were inserted
623 between NheI and sites of pET100 by Gibson assembly.
624
625 pET28-2×Strep-mCherry-SspB(micro)-mDia1(FH1-FH2-DAD)-TEVsite-6×His
626 A DNA fragment mDia1(FH1-FH2-DAD) was PCR amplified from pCold-mDia1 with the primer set
627 fwd: 5’-GGTCCTCGAGCCAAGAATGAAATGGCTTCTCTCTC-3’ and rev: 5’-
628 CGGTGGATCCGCTTGCACGGCCAACCAG-3’ and inserted between XhoI and BamHI sites of pET28-
629 2×Strep-mCherry-SspB(micro)-TEVsite-6×His by Gibson assembly.
630
631 pET28-2×Strep-mCherry-SspB(micro)-mDia1ΔDAD(FH1-FH2)-TEVsite-6×His
632 A DNA fragment mDia1(FH1-FH2) was PCR amplified from pCold-mDia1 with the primer set
633 fwd: 5’-GGTCCTCGAGCCAAGAATGAAATGGCTTCTCTCTC-3’ and rev: 5’-
634 CGGTGGATCCCTTCTCCTTGGCTAATTTTGCTCTCCG-3’ and inserted between XhoI and BamHI
635 sites of pET28-2×Strep-mCherry-SspB(micro)-TEVsite-6×His by Gibson assembly.
636
637 EYFP-FKBP-mDia1(FH1-FH2-DAD)
638 mDia1(FH1-FH2-DAD) was cut out from pCold-6×His-2×Strep-MBP-TEVsite-mCherry-
639 SspB(micro)-mDia1(FH1-FH2-DAD) by XhoI and BamHI and inserted between XhoI and BamHI of
640 EYFP-FKBP by restriction digestion and T4 ligation.
641
642 pET28-6×His-2×Strep-TEVsite-Capβ2(mouse)-Capα1(mouse)
643 First, pET28-6×His-2×Strep was constructed as follows. 6×His sequence was synthesized by oligo
644 annealing of fwd: 5’-AGGAGATATACCATGGGCCATCACCATCACCATCACATGGGCTGGTCTCA-3’ and
645 rev: 5’- TGAGACCAGCCCATGTGATGGTGATGGTGATGGCCCATGGTATATCTCCT-3’ and inserted into
646 NcoI site of pET28-2×Strep-tag. Capβ2(mouse)-Capα1(mouse) was PCR amplified from the
647 template of pET3d-Capβ2(mouse)-Capα1(mouse), gifted from Dr. Julie Plastino and Dr. Cecile
648 Sykes, with the primer set fwd: 5’-
649 CTGGAGCGGGTGCCGCTAGCGAGAACCTCTACTTTCAAAGCGATATGAGCGATCAGCAGCTGG-3’ and
650 rev: 5’- TGTCGACGGAGCTCGAATTCTTAAGCATTCTGCATTTCTTTGCCAATC-3’ and inserted
651 between NheI and EcoRI of pET28-6×His-2×Strep by Gibson assembly. TEV cleavage site was
652 designed in the forward primer and introduced between 2×Strep tag and Capβ2 ORF.
653
654 **Actin preparation**
655 Actin for GUV experiments was reconstituted from lyophilized powder as described in
656 manufacturer’s instructions, aliquoted, snap-frozen in liquid nitrogen, and stored at -80°C.
657 For actin polymerization assays, actin was dissolved in G-buffer [2 mM Tris-HCl (pH 7.5 at RT), 0.1
658 mM $CaCl_2$, 0.2 mM ATP, 0.5 mM DTT, 1 mM NaN_3] at concentration less than 65 µM and dialyzed

659 against G-buffer for 3 days with daily buffer exchange. Dialyzed actin was then purified by a
660 Superdex 200 increase 10/300 GL column (Cytiva) to separate monomer fraction from occasional
661 larger molecular size (smaller elution volume) fraction. The purified actin was stored at 4°C with
662 dialysis against G-buffer. The dialysis buffer for actin storage was exchanged twice a week**.**
663 Alexa 647 labeling of actin was performed following the previously reported method (*134*). First,
664 rabbit skeletal muscle actin (Cytoskeleton Inc., #AKL99) was dissolved in G*-buffer [2 mM Tris-
665 HCl (pH 7.5 at RT), 0.1 mM $CaCl_2$, 0.2 mM ATP] at concentration less than 65 µM. The solution
666 was dialyzed against G*-buffer overnight, followed by an additional 3 hour dialysis with fresh
667 buffer. Dialyzed actin was collected and mixed with 4 molar excess Alexa Fluor 647 C2 maleimide
668 (ThermoFisher, A20347, solubilized to 10 mM in DMSO) and incubated at 4°C overnight with
669 rotation (10 min labeling as in the original protocol did not yield efficient labeling in the case of
670 Alexa Fluor 647). The reaction was quenched by adding DTT to 10 mM. Aggregated proteins and
671 insoluble dyes were removed by ultracentrifugation at 350,000×g (90,000 rpm, TLA-100.1 rotor)
672 for 12 min. The supernatant was collected and mixed 1/10 volume of 10×KMEI buffer (500 mM
673 KCl, 10 mM $MgCl_2$, 10 mM EGTA, 100 mM Imidazole, pH 7.0) and final 1 mM ATP to polymerize
674 actin at RT for 2–3 hours. Labeled filamentous actin was collected by ultracentrifugation at
675 195,000×g (67,000 rpm, TLA-100.1 rotor) for 30 min and resuspended with G-buffer. The labeled
676 actin was dialyzed against G-buffer for 3 days with daily buffer exchange and purified through
677 size exclusion chromatography with a Superdex 200 increase 10/300. The protein was snap-
678 frozen in liquid nitrogen and stored at -80°C.
679
680 **Protein purification**
681 Protein expression~~s~~ were carried out in BL21-CodonPlus (DE3)-RIL (Agilent Technologies) and cell
682 lysis was performed by microfluidizer (Microfluidics, Model M-110Y), unless otherwise specified.
683
684 6×His-MBP-TEV protease (S219V)
685 The bacteria transformed with pQE80L-6×His-MBP-TEVprotease (S219V) were cultured overnight
686 in LB broth supplemented with 100 µg/mL Ampicillin and 25 µg/mL Chloramphenicol
687 (LB/Amp/Cam). Pre-culture was inoculated to LB/Amp/Cam and cultured at 37°C until OD_{600}
688 reached around 0.4. Protein expression was induced by adding 300 µM IPTG and allowed to
689 proceed for 17 hours at 18°C. The cells were re-suspended with 50 mM Tris-HCl (pH 7.5 at RT),
690 250 mM NaCl, 5 mM $MgCl_2$, 7 mM β-mercaptoethanol and lysed by microfluidizer. The lysate was
691 centrifuged at 20,000×g at 4°C for 30 min to remove cell debris. The protein was purified by Ni-
692 NTA, eluted around 60–100 mM imidazole, and then dialyzed against 25 mM Tris-HCl (pH 7.5 at
693 RT), 200 mM NaCl, 7 mM β-mercaptoethanol. The elution was concentrated by Amicon Ultra (10
694 kDa cutoff) and further dialyzed against 25 mM Tris-HCl (pH 7.5 at RT), 200 mM NaCl, 7 mM β-
695 mercaptoethanol, 50% glycerol. The protein was stored at -20 °C.
696

697 mCherry-SspB
698 The bacteria transformed with pQE80L-6×His-MBP-TEVsite-mCherry-SspB were cultured
699 overnight in LB broth supplemented with 100 µg/mL Ampicillin and 25 µg/mL Chloramphenicol
700 (LB/Amp/Cam). Pre-culture was inoculated to LB/Amp/Cam and cultured at 37°C until OD_{600}
701 reached 0.4–0.6. Protein expression was induced by adding 300 µM IPTG and allowed to proceed
702 for 18 hours at 22°C. The cells were re-suspended with 50 mM Tris-HCl (pH 7.5 at RT), 250 mM
703 NaCl, 7 mM β-mercaptoethanol, 20 mM Imidazole supplemented with cOmplete EDTA-free
704 protease Inhibitor Cocktail (MilliporeSigma) and lysed by microfluidizer. The lysate was
705 centrifuged at 20,000×g at 4°C for 30 min to remove cell debris. The protein was first purified by
706 Ni-NTA, eluted around 50 mM imidazole, and then dialyzed against 25 mM Tris-HCl (pH 7.5 at RT),
707 250 mM NaCl, 7 mM β-mercaptoethanol. 6×His-MBP tag was cleaved by 6×His-MBP-TEV protease
708 (S219V) (purified in house) during the dialysis. The cleaved 6×His-MBP tag and TEV protease were
709 removed through the second round of Ni-NTA column. Flow through and wash fractions were
710 dialyzed against buffer S [25 mM Tris-HCl (pH 7.5 at RT), 250 mM NaCl, 7 mM β-mercaptoethanol]
711 and concentrated by Amicon Ultra (10 kDa cutoff). The protein was snap-frozen in liquid nitrogen
712 in storage buffer [25 mM Tris-HCl (pH 7.5 at RT), 250 mM NaCl, 7 mM β-mercaptoethanol, 20%
713 glycerol] and stored at -80 °C.
714
715 iLID-YFP-MARCKS
716 The bacteria transformed with pET28-2×Strep-iLID-EYFP-MARCKS were cultured overnight in LB
717 broth supplemented with 50 µg/mL Kanamycin and 25 µg/mL Chloramphenicol (LB/Kan/Cam).
718 Pre-culture was inoculated to LB/Kan/Cam and cultured at 37°C until OD600 reached around 0.6.
719 Protein expression was induced by adding 300 µM IPTG and allowed to proceed for 17 hours at
720 23°C in the presence of 6 µM FMN. The cells were resuspended with buffer L1 [50 mM Tris-HCl
721 (pH 7.5 at RT), 200 mM NaCl, 1 mM EDTA, 7 mM β-mercaptoethanol] and lysed by microfluidizer.
722 The lysate was centrifuged at 20,000×g at 4°C for 30 min to remove cell debris. The supernatant
723 was applied to Strep-Tactin XT (IBA Lifesciences) equilibrated with buffer L1 and the protein was
724 eluted with 50 mM biotin in buffer L1. The elution was dialyzed against buffer L2 [25 mM Tris-
725 HCl (pH 7.5 at RT), 200 mM NaCl, 7 mM β-mercaptoethanol] and concentrated by Amicon Ultra
726 (10 kDa cutoff). The protein was snap-frozen in liquid nitrogen in storage buffer [25 mM Tris-HCl
727 (pH 7.5 at RT), 200 mM NaCl, 7 mM β-mercaptoethanol, 30% glycerol] and stored at -80 °C.
728
729 iLID-YFP-SNAP
730 The bacteria transformed with pET28-2×Strep-iLID-EYFP-SNAP were cultured overnight in LB
731 broth supplemented with 50 µg/mL Kanamycin and 25 µg/mL Chloramphenicol (LB/Kan/Cam).
732 Pre-culture was inoculated to LB/Kan/Cam and cultured at 37°C until OD_{600} reached around 0.5.
733 Protein expression was induced by adding 300 µM IPTG and allowed to proceed for 20 hours at
734 23°C in the presence of 6 µM FMN. The cells were resuspended with buffer L1 (50 mM Tris-HCl

735 (pH 7.5 at RT), 200 mM NaCl, 1 mM EDTA, 7 mM β-mercaptoethanol) and lysed by microfluidizer.
736 The lysate was centrifuged at 20,000×g at 4°C for 30 min to remove cell debris. The supernatant
737 was applied to Strep-Tactin XT (IBA Lifesciences) equilibrated with buffer L and the protein was
738 eluted with 50 mM biotin in buffer L1. The elution was further purified by Superdex 200 increase
739 10/300 GL column in the buffer L2 [25 mM Tris-HCl (pH 7.5 at RT), 200 mM NaCl, 7 mM β-
740 mercaptoethanol] and concentrated by Amicon Ultra (10 kDa cutoff). The protein was snap-
741 frozen in liquid nitrogen in storage buffer [25 mM Tris-HCl (pH 7.5 at RT), 200 mM NaCl, 7 mM β-
742 mercaptoethanol, 30% glycerol] and stored at -80 °C.
743
744 SsrA-SNAP
745 BL21(DE3) RP transformed with pET28-2×Strep-SsrA-SNAP were cultured overnight in LB broth
746 supplemented with 50 µg/mL Kanamycin and 25 µg/mL Chloramphenicol (LB/Kan/Cam). Pre-
747 culture was inoculated to LB/Kan/Cam and cultured at 37°C until OD_{600} reached around 0.5.
748 Protein expression was induced by adding 300 µM IPTG and allowed to proceed for 20 hours at
749 23°C. The cells were resuspended with lysis buffer [50 mM Tris-HCl (pH 7.6 at RT), 200 mM NaCl,
750 1 mM $MgCl_2$, 7 mM β-mercaptoethanol, 1 mM PMSF, 1× protease inhibitor cocktail V (Wako 168-
751 26033)] supplemented with house-purified benzonase and sonicated by Misonix Ultrasonic
752 Liquid Processor Sonicator S4000 (amplitude 30, 2 seconds ON, 10 seconds OFF, total 3 minutes
753 ON). The lysate was centrifuged at 13,420×g at 4°C for 45 min to remove cell debris. The
754 supernatant was applied to Strep-Tactin XT High Capacity (IBA Lifesciences) equilibrated with
755 buffer L3 (25 mM Tris-HCl (pH 7.6 at RT), 200 mM NaCl, 1 mM $MgCl_2$, 7 mM β-mercaptoethanol,
756 1 mM PMSF) and the protein was eluted with 100 mM biotin in wash buffer. The elution was
757 dialyzed against buffer L3 and further purified by Superdex 200 increase 10/300 GL column in
758 buffer L3. Peak fractions were collected and concentrated by Viva Spin Turbo (10 kDa cutoff). The
759 protein was snap-frozen in liquid nitrogen in storage buffer (25 mM Tris-HCl (pH 7.6 at RT), 200
760 mM NaCl, 7 mM β-mercaptoethanol, 40% glycerol) and stored at -80 °C.
761
762 GST-pVCA-SspB-mCherry
763 The bacteria transformed with pGEX2T-GST-pVCA-3Csite-SspB(micro)-mCherry-TEVsite-6×His or
764 pGEX2T-GST-pVCA-3Csite-SspB(nano)-mCherry-TEVsite-6×His were cultured overnight in LB
765 broth supplemented with 100 µg/mL Ampicillin and 25 µg/mL Chloramphenicol (LB/Amp/Cam).
766 Pre-culture was inoculated to LB/Amp/Cam and cultured at 37°C until OD_{600} reached around 0.5–
767 0.6. After cooling the culture on ice, protein expression was induced by adding 300 µM IPTG and
768 allowed to proceed for 24–26 hours at 18°C. The cells were resuspended with buffer V (50 mM
769 HEPES-NaOH (pH 7.5), 150 mM NaCl, 10% glycerol, 14 mM β-mercaptoethanol, 1 mM EDTA, 1
770 mM PMSF, 100 µg/mL DNase, supplemented with cOmplete EDTA-free protease inhibitor
771 cocktail) and lysed by microfluidizer. The lysate was centrifuged at 20,000×g at 4°C for 30 min to
772 remove cell debris. To enhance resin binding, final 5 mM DTT was added to the lysate. The lysate

773 was applied to glutathione sepharose equilibrated with buffer V [50 mM HEPES-NaOH (pH 7.5)
774 150 mM NaCl, 10% glycerol, 7 mM β-mercaptoethanol, and 1 mM PMSF], and the protein was
775 eluted with 20 mM glutathione in buffer V (pH was adjusted between 7.0–8.0 by NaOH). The
776 elution was then purified by Ni-NTA and eluted with 50–500 mM imidazole. After concentrated
777 by Amicon Ultra (10 kDa cutoff), the protein was further purified by Superdex 200 increase
778 10/300 GL column in buffer V and concentrated again by Amicon Ultra (10 kDa cutoff). The
779 protein was snap-frozen in liquid nitrogen and stored at -80 °C.
780
781
782 mCherry-SspB-mDia1
783 The bacteria transformed with pET28-2×Strep-mCherry-SspB(micro)-mDia1(FH1-FH2-DAD) were
784 cultured overnight in LB broth supplemented with 50 µg/mL Kanamycin and 25 µg/mL
785 Chloramphenicol (LB/Kan/Cam). Pre-culture was inoculated to LB/Kan/Cam and cultured at 37°C
786 until OD_{600} reached around 0.5–0.6. After cooling the culture on ice, protein expression was
787 induced by adding 300 µM IPTG and allowed to proceed for 24 hours at 16°C. The cells were
788 resuspended with buffer D [50 mM Tris-HCl (pH 7.5), 500 mM NaCl, 10% glycerol, 1 mM DTT, 1
789 mM EDTA, 1 mM PMSF, 100 µg/mL DNase, supplemented with cOmplete EDTA-free protease
790 inhibitor cocktail] and lysed by microfluidizer. The lysate was centrifuged at 20,000×g at 4°C for
791 30 min to remove cell debris. The supernatant was applied to Strep-Tactin XT (IBA Lifesciences)
792 equilibrated with buffer D1 (50 mM Tris-HCl (pH 7.5), 500 mM NaCl, 10% glycerol, 1 mM DTT, 1
793 mM EDTA, 1 mM PMSF) and the protein was eluted with 50 mM biotin in buffer D1. The elution
794 was concentrated by Amicon Ultra (10 kDa cutoff) and dialyzed against buffer D2 [25 mM HEPES-
795 NaOH (pH 7.5), 150 mM NaCl, 7 mM β-mercaptoethanol, 10% glycerol]. The protein was further
796 purified by Superdex 200 increase 10/300 GL column in buffer D2 and concentrated again by
797 Amicon Ultra (10 kDa cutoff). The protein was snap-frozen in liquid nitrogen and stored at -80 °C.
798 This protein was used as mDia1 in most figures unless otherwise indicated.
799
800 mCherry-SspB-mDia1-6×His and mCherry-SspB-mDia1ΔDAD-6×His
801 The bacteria transformed with pET28-2×Strep-mCherry-SspB(micro)-mDia1(FH1-FH2-DAD)-
802 TEVsite-6×His or pET28-2×Strep-mCherry-SspB(micro)-mDia1ΔDAD(FH1-FH2)-TEVsite-6×His
803 were cultured overnight in LB broth supplemented with 50 µg/mL Kanamycin and 25 µg/mL
804 Chloramphenicol (LB/Kan/Cam). Pre-culture was inoculated to LB/Kan/Cam and cultured at 37°C
805 until OD_{600} reached around 0.5–0.6. After cooling the culture on ice, protein expression was
806 induced by adding 300 µM IPTG and allowed to proceed for 24 hours at 16°C. The cells were
807 resuspended with buffer D3 [50 mM Tris-HCl (pH 8.0), 500 mM NaCl, 10% glycerol, 1 mM DTT,
808 1 mM PMSF] supplemented with 1× protease inhibitor cocktail V (Wako 168-26033)] and house-
809 purified benzonase, and sonicated by Misonix Ultrasonic Liquid Processor Sonicator S4000
810 (amplitude 30, 2 seconds ON, 10 seconds OFF, total 3 minutes ON). Unbroken cells were pelleted

811 by centrifugation at 13,420×g for 5 min at 4°C, resuspended in buffer D1, and subjected to
812 sonication under the same conditions. This procedure was repeated twice. The lysate was then
813 clarified by centrifugation at 13,420×g for 45 min at 4°C. The supernatant was applied to Strep-
814 Tactin XT (IBA Lifesciences) equilibrated with buffer D3 and the protein was eluted with 100 mM
815 biotin in buffer D3. The elution was then purified by Ni-NTA equilibrated with 50 mM Tris-HCl (pH
816 8.0), 150 mM NaCl, 10% glycerol, 7 mM β-mercaptoethanol, 1 mM PMSF and eluted stepwise
817 with 20–500 mM imidazole. Peak fractions were collected and diluted 3-fold with 50 mM Tris-
818 HCl (pH 8.0), 10% glycerol, 7 mM β-mercaptoethanol, 1 mM PMSF. The protein was further
819 purified by HiTrapQ column equilibrated with 50 mM HEPES-NaOH (pH 7.5), 50 mM NaCl, 10%
820 glycerol, 7 mM β-mercaptoethanol, 1 mM PMSF, and eluted with linear NaCl gradients of 50–500
821 mM NaCl. The protein was concentrated by Viva Spin Turbo (10 kDa cutoff), snap-frozen in liquid
822 nitrogen and stored at -80 °C. mCherry-SspB-mDia1-6×His was used in Figure 2E, F, H, S10, S12.
823 mCherry-SspB-mDia1ΔDAD-6×His was used in Figure 4J.
824
825 Capping protein
826 The bacteria transformed with pET28-6×His-2×Strep-TEVsite-Capβ2(mouse)-Capα1(mouse) were
827 cultured overnight in LB/Kan/Cam. Pre-culture was inoculated to LB/Kan/Cam and cultured at
828 37°C until OD_{600} reached around 0.7. Protein expression was induced by adding 300 µM IPTG and
829 allowed to proceed for 24 hours at 18°C. The cells were re-suspended with 50 mM Tris-HCl (pH
830 7.5 at RT), 150 mM NaCl, 14 mM β-mercaptoethanol, 1 mM EDTA, 1 mM PMSF, 100 µg/mL
831 DNase and lysed by microfluidizer. The lysate was centrifuged at 20,000×g at 4°C for 30 min to
832 remove cell debris. The supernatant was applied to Strep-Tactin XT 4Flow (IBA Lifesciences)
833 equilibrated with buffer C1 [50 mM Tris-HCl (pH 7.5 at RT), 150 mM NaCl, 7 mM β-
834 mercaptoethanol] and the protein was eluted with 50 mM biotin in buffer C1. The elution was
835 dialyzed against buffer C2 [25 mM Tris-HCl (pH 7.5 at RT), 150 mM NaCl, 7 mM β-
836 mercaptoethanol]. 6×His-2×Strep tag was cleaved by 6×His-MBP-TEV protease (S219V) (purified
837 in house) during the dialysis. The cleaved 6×His-2×Strep tag and TEV protease were removed
838 through Ni-NTA column. Flow through and wash fractions were dialyzed against buffer and
839 concentrated by Amicon Ultra (10 kDa cutoff). The protein was snap-frozen in liquid nitrogen in
840 buffer C2 and stored at -80 °C.
841
842 **Pyrene-actin polymerization assay**
843 For pyrene actin assay, actin was purified by size exclusion column. One milligram of actin
844 (Cytoskeleton Inc. AKL99-B) was dissolved in 400 µL G-buffer [2 mM Tris-HCl (pH 7.5 at RT), 0.1
845 mM $CaCl_2$, 0.2 mM ATP, 0.5 mM DTT, 1 mM NaN_3] and dialyzed against the same buffer. After 3
846 days dialysis with daily buffer exchange, the actin was purified by Superdex 200 Increase 10/300
847 GL column (GE Healthcare) to separate monomer fraction from a fraction occasionally appear at

848 larger size molecular size (smaller elution volume). The purified actin was stored at 4°C in a
849 dialyzed manner against G-Buffer with twice a week buffer exchange.
850 Pyrene-actin polymerization assay was performed with FluoroMax 3 and DataMax software.
851 Pyrene fluorescence and its kinetics were measured by 365 nm excitation (1 nm bandwidth) and
852 407 nm emission (5 nm bandwidth). The reaction was prepared by following the previously
853 reported method (*135*), except that the reaction was 50 µL in quartz cuvettes (Hellma, 105-251-
854 15-40).
855
856 **Ultracentrifugation assay**
857 Reaction solutions were prepared by mixing 4.5 µL of actin in G-buffer and 4.5 µL of other
858 proteins solution. At the final concentration, reaction solution contained 7.5 µM actin (10% Alexa
859 488 labeled), 1 µM GST-pVCA-SspB(micro)-mCherry, 1 µM mCherry-SspB(micro)-mDia1, 150 nM
860 Arp2/3, 50 nM capping protein, 3 µM profilin, 2 µM cofilin, 1 µM creatin kinase, 1 mM ATP, 25
861 mM creatin phosphate, 240 mM sucrose, and 1×KMEI buffer [10 mM imidazole pH 7.0, 50 mM
862 KCl, 1 mM $MgCl_2$, 1 mM EGTA]. Polymerization reaction for 30 min at RT. The solutions were
863 ultracentrifuged at 100,000×g (90,000 rpm, S55A2 rotor) for 1 hour at RT and analyzed by SDS-
864 PAGE.
865
866 **GUV preparation by emulsion transfer**
867 Lipid-in-oil solution was prepared as follows. Chloroform solutions of lipids were mixed in 5 mL
868 glass vial, dried at 70°C with N_2 gas flow, and left in vacuum 3 hours to overnight. The amounts
869 of lipids were typically 6.5 µmol (1.3 mM, 1 mg/mL at final concentration in oil) for 40 mol%
870 POPS/60 mol% POPC mixture (MARCKS peptide anchoring) and 1.5 µmol (0.3 mM, 0.23 mg/mL
871 at final concentration in oil) for 2 mol% Benzylguanine-conjugated lipid/98 mol% POPC and 100%
872 POPC (SNAP-tag anchoring). Lipid was dissolved in 5 mL of oil mixture (90 volume% hexadecane,
873 10 volume% silicone oil) by heating at 80˚C for 1–2 hours, then brought to RT.
874 For iLID-SspB translocation experiments, inner solution contained 4 µM iLID-YFP-SNAP (or iLID-
875 EYFP-MARCKS) and 1 µM mCherry-SspB(micro) in buffer (22.5 mM Tris-HCl (pH 7.5 at RT), 122.5
876 mM NaCl, 2 mM $MgCl_2$, 240 mM sucrose, 0.7 mM β-mercaptoethanol, and 3% glycerol). Outer
877 solution was prepared by replacing protein fractions of inner solution with their buffers and
878 sucrose with glucose.
879 For actin polymerization experiments, inner solution was prepared by mixing 10 µL of actin (10%
880 Alexa 647 labeled) in G-buffer and 10 µL of other proteins solution similarly to pyrene actin
881 polymerization assay. At the final concentration, inner solution typically contained 11.75 µM
882 iLID-EYFP-SNAP, 1 µM GST-pVCA-SspB(micro)-mCherry, 1 µM mCherry-SspB(micro)-mDia1, 7.5
883 µM actin, 150 nM Arp2/3, 50 nM capping protein, 3 µM profilin, 2 µM cofilin, 1 µM creatine
884 kinase in the buffer (5.9 mM Tris-HCl (pH 7.5 at RT), 1.3 mM HEPES-NaOH (pH 7.5 at RT), 7.7 mM
885 Imidazole (pH 8.0 at RT), 27 µM KH_2PO_4, 74 µM Na_2HPO_4, 39 mM KCl, 33 mM NaCl, 0.8 mM $MgCl_2$,

886 43 µM $CaCl_2$, 1.1 mM EGTA, 1.2 mM β-mercaptoethanol, 0.21 mM DTT, 0.43 mM NaN_3, 1 mM
887 ATP, 25 mM creatine phosphate, 240 mM sucrose and 2.8% glycerol). Outer solution was
888 prepared by replacing protein fractions of inner solution with their buffers and sucrose with
889 glucose. Protein and buffer conditions are summarized in Supplementary table 1.
890 In experiments using pVCA alone, SspB(nano) was employed to ensure sufficiently robust light-
891 induced membrane recruitment and actin polymerization, and pVCA was used at 4–4.2 µM.
892 When mDia1 was included, SspB(micro) was used to avoid excessive basal membrane association
893 of mDia1 prior to illumination. To maintain comparable recruitment behavior within the
894 combined system, pVCA was also fused to SspB(micro) and used at 1 µM, matching the
895 concentration of mDia1.
896 GUVs were prepared as previously reported (*56*, *136*). Briefly, oil-buffer interface was created by
897 layering 250 µL lipid-in-oil solution on top of 250 µL outer buffer in 1.5 mL tube. Water-in-oil
898 emulsion was made by vigorously pipetting 20 µL of inner solution in 250 µL of lipid-in-oil solution
899 and then gently added to the top of the oil-buffer layers. The emulsions were transferred through
900 the oil-buffer interface by centrifugation at 2500×g for 2 min at RT. GUVs were collected by
901 pipetting.
902
903 **Image acquisition and analysis**
904 For imaging GUVs, 8-well glass chamber slides (ThermoFisher Scientific, 154534) were pretreated
905 with 10 mg/mL BSA in PBS for 10 minutes and washed with MilliQ water twice. LSM780 confocal
906 microscope (Zeiss) equipped with Plan-Apochromat 63X/1.40na oil immersion DIC objective lens
907 (Zeiss 420782-9900) was used for imaging and light stimulation of GUVs. YFP, mCherry, and Alexa
908 Fluor 647 were imaged with 514, 561, and 633 nm excitation lasers, respectively. Blue light
909 illumination for iLID stimulation was performed by using bleaching function with 458 nm laser at
910 intensity 1.0–5.0%, scan speed 6 (pixel dwell time = 6.3 µsec). Main beam splitters MBS458/561,
911 MBS 488/561/633, and MBS 458/514 were used for 458 and 561, 633, and 514 nm excitation,
912 respectively. The imaging was performed at room temperature. Data were analyzed by Fiji
913 software (*137*).
914
915 **FRAP analysis on GUV membranes**
916 A small region of interest (ROI) on the GUV membrane was selectively photobleached for 1 s
917 using high-intensity laser illumination. Fluorescence recovery within the bleached ROI was
918 measured. To correct for photobleaching caused by repeated imaging, fluorescence intensity in
919 the bleached ROI was normalized to that of a non-bleached reference region on the same GUV
920 membrane. To capture rapid fluorescence recovery with short imaging intervals, mCherry- and
921 Alexa Fluor 647–labeled signals were analyzed on different individual GUVs.
922
923 **Small unilamellar vesicles (SUVs) preparation**

924 SUVs used for EM experiments were prepared as follows. Chloroform solutions of lipids were
925 mixed in 5 mL glass vial, dried at 70°C under a flow of N_2 gas, and left under vacuum overnight.
926 The total amount of lipid was 0.5 µmol (corresponding to 5 mM, or 4 mg/mL, at the final
927 concentration in buffer). Lipid composition was 2 mol% benzylguanine-conjugated lipid/98 mol%
928 POPC. The lipid film was hydrated with 100 µL of SUV buffer (25 mM HEPES-KOH (pH 7.6), 50 mM
929 KCl, 1 mM $MgCl_2$, 1 mM TCEP), incubated at 37°C for 10 min, and sonicated using Misonix
930 Ultrasonic Liquid Processor Sonicator S4000.
931
932 **Electron microscopy (EM)**
933 The reaction for EM imaging was prepared by mixing 2.75 µL of a solution containing all
934 components except actin (solution I) with 2.25 µL of actin in G-Mg buffer [2 mM Tris-HCl (pH 7.5),
935 0.2 mM ATP, 0.1 mM $MgCl_2$, 0.5 mM DTT, 1 mM NaN_3] (solution II). Solution I was first placed to
936 carbon-coated collodion film on a Cu grid (Nisshin EM, Tokyo, Japan) and incubated for several
937 seconds to allow SUVs to settle onto the grid surface. Solution II was then added, and actin
938 polymerization was allowed to proceed for 3 min at room temperature (24–26°C). At final
939 concentrations, the reaction mixture contained 0.3 mg/mL lipid SUVs, 7.5 µM actin (10% Alexa
940 Fluor 647–labeled), 1 µM GST–pVCA–SspB(micro)–mCherry, 1 µM mCherry–SspB(micro)–
941 mDia1(FH1–FH2–DAD)–6×His, 150 nM Arp2/3 complex, 50 nM capping protein, 3 µM profilin, 2
942 µM cofilin, 1 µM creatine kinase, 1 mM ATP, 25 mM creatine phosphate, and 1× KMEI buffer (10
943 mM imidazole, pH 7.0, 50 mM KCl, 1 mM $MgCl_2$, 1 mM EGTA). After the reaction, excess liquid
944 on the grid was carefully removed, followed by negative staining with 2% phosphotungstic acid
945 (pH 7.0). The samples were observed with a JEM1010 EM (JEOL, Akishima, Japan) at 80 kV
946 equipped with a FastScan-F214(T) charge-coupled device (CCD) camera (TVIPS, Gauting,
947 Germany).
948
949 **Live-cell CID experiments**
950 DNA constructs: Four plasmids were used which encoded Lyn-CFP-FRB (*138*), YFP-FKBP (*138*),
951 YFP-FKBP-Tiam1 (*133*), YFP-FKBP-pVCA, and YFP-FKBP-mDia1.
952 Cell culture: HEK293T cells (ATCC) were cultured in DMEM (Corning, 10-013-CV) supplemented
953 with 10% fetal bovine serum (Corning, 35-010-CV) and 1% penicillin-streptomycin (ThermoFisher,
954 15140163).
955 Transient transfection: HEK293T cells were seeded at a density of 9,000-12,000 cells in an 8-well
956 chamber slide. Per well, a solution of 0.3 µg of DNA, 1 µL of FuGENE HD, and 30 µL of Opti-MEM
957 was added for transfection. FRB:FKBP pairs were cotransfected in a 1:1 or 1:2 ratio. Cells
958 were incubated at 37°C with 5% CO_2 and 95% humidity for 24–48 h before imaging.
959 Microscopes and imaging: Live cell imaging of actin NPF recruitment to the cell membrane was
960 performed using an Eclipse Ti inverted fluorescence microscope (Nikon) with a 100x Oil objective
961 lens and Andor Zyla 4.2 plus sCMOS camera, or with a 60x Oil, TIRF 60x Oil, or TIRF 100x Oil

962 objective lens and ORCA-Fusion Digital CMOS camera. Images were captured every 1 min for 30-
963 120 min, where within 5 min of starting, 0.1 µM rapamycin was added. Nikon microscopes were
964 driven by NIS-Elements software (Nikon). All live-cell imaging was performed at 37 °C with 5%
965 CO_2 and humidity control by a stage top incubator. Image processing and analysis were
966 performed using Fiji software.
967 Data analysis: Per transfection sample, a count was made based on the phenotype of cells falling
968 into three categories: no change, lamellipodia, and filopodia. Cells with lamellipodia or filopodia
969 pre-rapamycin were not counted unless new membrane protrusions formed after rapamycin
970 addition. If the cell under observation did not produce any new lamellipodia or filopodia after
971 addition of rapamycin, then it was counted as no change. Only healthy cells fully in the field of
972 view with clear expression of both FRB and FKBP constructs were counted. If there was any doubt
973 in the phenotype of the cell, then it was not included in the count.
974 Statistics
975 1. The cell counts for each category were summed across all experiments, and this sum was
976 divided by the total number of cells to get a percentage of cells belonging to each category when
977 a certain actin NPF was recruited to the membrane.
978 2. For each image set collected from a transfection sample, the categorized cell counts were
979 divided by the total cell count to get percentages. For each actin NPF, the percentages from all
980 transfection samples were averaged. These averages were analyzed by two-tailed Student's t-
981 test assuming equal variance (determined by F-test) in order to establish the significance of
982 lamellipodia or filopodia detection between transfection samples.
983
984 **Statistics and reproducibility**
985 Quantitative data with error bars were obtained from three or more independent experiments,
986 except for fig. S10 and S11, which were obtained from two independent experiments. Where
987 indicated, 95% confidence intervals of the mean were calculated in Microsoft Excel using the t-
988 distribution (T.INV.2T) and the standard error (SD/√n). For statistical comparison of multiple
989 groups, the Steel–Dwass test was performed using the pSDCFlig function (asymptotic option) in
990 the NSM3 package in R. Pearson's R and p-values in fig. S19 was calculated by cor.test function
991 (pearson option).
992
993 **Theoretical model of actin filament-membrane interactions**
994 We employed Cytosim (*95*), a stochastic agent-based cytoskeletal modeling framework that
995 incorporates Brownian dynamics, actin filament dynamics, and the action of actin-binding
996 proteins. To Cytosim, we added a deformable membrane model (*96*) along with terms for the
997 reciprocal actin-membrane interactions (*97*). In the following text we elaborate on the details
998 and implementation for each model component. We further refer the reader to Table 1, for a

complete list of parameters and their corresponding references from where they were obtained. The use of these physically relevant parameters constraint our simulations against reality.

To model the membrane, we utilize a 2-D enclosed polygon with resistance to bending and stretching. The energy of the membrane is given by discrete 2-D Helfrich Hamiltonian,

$$E = \frac{\kappa}{4} \sum_{i=1}^{N_{edges}} k_i^2 l_i^2 + \sum_{i=1}^{N_{edges}} \sigma l_i^2,$$

where κ is the bending rigidity of the membrane and σ is the membrane surface tension. k_i is the local curvature at vertex i and l_i is the length of the edge connecting vertices i and i+1. The force on a vertex i is given by

$$\frac{\partial E}{\partial r_i} = \frac{\kappa}{4} \sum_{i=1}^{N_{edges}} \left[l_i^2 \frac{\partial}{\partial r_i}(k_i^2) + 2 l_i k_i^2 \frac{\partial}{\partial r_i} l_i \right] + \sum_{i=1}^{N_{edges}} 2\sigma l_i \frac{\partial}{\partial r_i} l_{i.}$$

There are several established ways to define curvature in discrete settings (*139*, *140*). For this model, we choose a definition of curvature based on the turning angle at each vertex.

$$k_i = \frac{\tan\left(\frac{\alpha_i}{2}\right) + \tan\left(\frac{\alpha_{i+1}}{2}\right)}{l_i},$$

where the turning angle α_i is given by the sum of the internal angles,

$$\alpha_i = \tan^{-1}\left(\frac{l_{i,y}}{l_{i,x}}\right) + \tan^{-1}\left(\frac{l_{i+1,y}}{l_{i+1,x}}\right),$$

and we can express $\partial l_i/\partial r_a$ and $\partial \alpha_i/\partial r_a$ as

$$\frac{\partial l_i}{\partial r_a} = -\frac{\mathrm{e}_i}{|\mathrm{e}_i|},$$

$$\frac{\partial \alpha_i}{\partial r_a} = \frac{\eta_i}{|\eta|^2},$$

respectively, as the unit vector along the edge i and the unit normal to the edge i.

Filament description

The actin filaments are modeled as described in the original Cytosim reference (*95*). In brief, actin filaments are modeled as semiflexible, inextensible fibers composed of linear segments with hinge points that allow for bending. The bending rigidity of the filament, k_{bend}, is chosen so that the persistence length of an isolated filament is 17 μm.

Filament-membrane interactions

We model filament-membrane interactions using a purely repulsive harmonic potential between points on the filament and the edges of the enclosed polygon. Given a position **p** on a filament *i* and an edge *j* on the enclosed membrane, the force is given by

$$F^{excl} = K^{excl}(\boldsymbol{q} - \boldsymbol{p}),$$

where $\boldsymbol{q}$ is the point closest to the point $\boldsymbol{p}$ on the edge *j* and $K^{excl}$is the stiffness of the steric potential.

F^{excl} confines the actin filament within the enclosed membrane and applies a force from the actin filament to the membrane. The steric force to points on the membrane edge c_j and c_{j+1} is calculated using the lever rule,

$$F(c_{j+1}) = F^{excl}\left(\frac{|q - c_j|}{|c_{j+1} - c_j|}\right),$$

$$F(c_j) = F^{excl} - F(c_{j+1}).$$

Inter-filament interactions

They are implemented as a repulsive harmonic potential between filaments, mimicking the physical constraints and forces arising from their proximity and entanglement.

Dynamics of filament growth

We assume that filaments polymerize at their barbed ends and do not depolymerize at the pointed ends. We assume a constant polymerization rate dependent on which actin-binding protein is bound to the filament.

Actin-binding proteins and nucleation promoting factors

We considered three proteins: mDia1 (formin) and Arp2/3. To model the spatial control of mDia1 and pVCA, we assume that iLID-SspB is already attached to pVCA and mDia1 at the membrane surface. To capture the actin nucleation and polymerization dynamics of the experiment, we modeled mDia1 and pVCA as beads that can nucleate and elongate actin filaments at prescribed rates. For reasons of computational cost, we assume that pVCA recruitment of Arp2/3 is fast. It has been shown experimentally that pVCA unbinds Arp2/3 after nucleation (*141*). In our model, pVCA unbinds the mother filament after nucleation. After initial nucleation by pVCA-Arp2/3

complex, free Arp2/3 can bind to mother filaments and nucleate daughter filaments. Arp2/3 stochastically bind mother filaments with a rate k_{bind} and unbind with a rate k_{unbind} in a force-dependent manner given by

$$k_{unbind} = k_{unbind,0} \exp\left(\frac{F}{F_d}\right),$$

where $k_{unbind,0}$ is the unbinding rate in the absence of force, **F** is the force experienced by the actin-binding protein and F_d is a characteristic detachment force.

Dynamics of network evolution

Unbound actin-binding proteins, filament motion, and membrane deformations are governed by Langevin dynamics. In each time interval Δt, we update the positions of all particles in the system using

$$\mathrm{x}(t + \Delta t) = \mathrm{x}(t) + \mu \mathrm{F}(t)\Delta t + \mathrm{B}(t)\Delta t.$$

Here, μ is the viscosity of the medium. **F**(t) is the sum total of all forces acting on the particle at time t. **B**(t) is the Brownian noise term, which is a random variable drawn from a normal distribution with a mean of 0 and a variance of $2\mu k_B T \Delta t$. $k_B$is the Boltzmann constant and T is the temperature.

The forces on the membrane are composed of forces from membrane surface tension, bending rigidity, and point forces from the actin filaments on the membrane. In our formulation, the speed at which membrane deformation occurs is governed by a membrane deformation parameter, $\mu_{mobility}$(not to be confused with the viscosity of the medium), which acts as a dampener to slow down the deformation of the membrane over time.

Model Assumptions

To capture the length control effect of capping protein in the experiments, we cap filament growth to a particular filament length. Our current model does not account for filament turnover, a feature we plan to incorporate in future simulations. Because we are simulating the 2-D projection of the membrane, we assume that the membrane is in a low-tension regime and any stretching of the membrane during deformation results from overcoming entropic and enthalpic cost of unfolding of wrinkles. Membrane surface tension is set to 0.001 mN/m in line with experimentally reported values (*142*).

For computational cost and technical challenges of performing simulations on the timescales of the experiments, we assumed faster nucleation rates for mDia1 and pVCA-bound Arp2/3 and simulated for shorter timescales.

Simulation set-up

1092 Mimicking the instance of asymmetric surface accumulation after illumination, we randomly
1093 placed surface-bound nucleators at the right edge of the model GUV and simulated the system
1094 for a period of 5 s. We examined three cases: one with pVCA and Arp2/3, one with mDia1 only
1095 and one with both NPFs and Arp2/3. For each case, we simulated conditions with and without
1096 inter-filament interactions, giving a total of 6 simulation conditions. We performed 20
1097 independent trajectories per condition.
1098
1099 Table 1. List of Parameters used in the simulations

Parameter	**Units**	**Value(s)**	**References**
r_{eff}	µm	0.035	This study
t_{final}	s	5	This study
Boundary Repulsion	pN/µm	10	This study
r_{cutoff}	µm	0.0035	Based on the radius of an actin filament
Brownian ratchet force for polymerization	pN	3	Footer et al. 2007 (*143*)
Growth rate	µm/s	0.033 (Arp23), 0.167 (Formin)	Kovar 2004 (*144*)
pVCA-Arp2/3 binding rate	s^{-1}	1	Beltzner and Pollard 2008 (*141*)
pVCA-Arp2/3 unbinding rate	s^{-1}	0.001	Beltzner and Pollard 2008 (*141*)
pVCA-Arp2/3 nucleation rate	s^{-1}	5	This study
mDia1 nucleation rate	s^{-1}	10	This study
Final filament length	µm	0.75	This study
Steric strength	pN/µm	0, 10	This study
Membrane surface tension	mN/m	10^{-3}	Rawicz et al. 2000 (*142*)
Membrane bending modulus	$k_B T$	20	Drabik et al. 2020 (*145*)
Filament Bending rigidity	pNµm	0.068	Akenuwa and Abel 2023 (*146*)
Number of mDia1, Arp2/3, pVCA		50	This study
Medium viscosity	Pa·s	0.001	

Membrane deformation parameter	Pa·s	1.0	This study

Quantification of membrane deformation in simulations

To quantify the extent of actin-induced membrane deformation, we calculated the average difference between the radius of the GUV and the distance from each node in the leading edge of the membrane to the center of the membrane at the final timepoint.

$$\Delta L = \frac{1}{M}\sum_{i=1}^{M}(|\vec{r_i}| - r_{GUV})\ \forall M \in N(leading\ edge)$$

Acknowledgement

We thank Yubin Zhou for TEV protease plasmid; Masato Kanemaki for pET28-2×Strep-tag plasmid; Miho Iijima for pGEX-2T plasmid; Bin Wu for Phage-ubc-nls-ha-tdMCP-SNAP plasmid; Roberto Dominguez for pCold-mDia1 plasmid, Saki Takayanagi for constructing GST-pVCA-FKBP-EYFP plasmid. We also thank Yusuke Sato, Taro Toyota, Pushpendra Singh, Tetsuya Kotani, Takeya Masubuchi for technical advice on the experiments. We appreciate Erin D. Goley for technical support of pyrene assay and insightful comments on actin preparation. We also appreciate Julie Plastino and Cecile Sykes for pET3d-Capβ2(mouse)-Capα1(mouse) plasmid and insightful advice on protein purification. Our appreciation extends to Pablo A. Iglesias for fruitful discussion. We thank our lab members, including Allen Kim, Abhijit Deb Roy, Helen D. Wu, Yuta Nihongaki for constructive discussion. We thank Kyoko Chiba for technical support on protein purification. We also thank Robert DeRose for proofreading the manuscript and experimental support. FRIS CoRE (a shared research environment in Tohoku University) is also acknowledged. This study was supported by the PRESTO program (JPMJPR12A5 to TI, JPMJPR20KA to HTM), CREST program (JPMJCR19S5 to MM), and FOREST program (JPMJFR2416 to HTM) of the Japan Science and Technology Agency, MEXT/JSPS KAKENHI Grants (23K14150, 23H04397, 25K02234, 25H02347 to HTM), National Institutes of Health (5R01GM123130, R01GM136858, R35GM149329 to TI, and R35GM128786 to BC), ExCELLS project research (25EXC604-6 to HTM) and the National Science Foundation (000819255 to TI, JL, BC). TI was also supported by Nitto Denko Corp. HTM was supported by Postdoctoral Fellowships from the Japan Society for the Promotion of Science. SR was supported by the National Science Foundation and the Japan Society for the Promotion of Science (JSPS) East Asia and Pacific Summer Institutes and Johns Hopkins Lucille Elizabeth Hay graduate fellowships. Computer simulations were run on hardware hosted by the Triton Shared

Computing Cluster (*147*). OHA and CTL further acknowledge high performance computing support from the UCSD Physics Computing Facility.

Author contributions

HTM, SR, and TI conceived the project. HTM performed most of the experiments and analyzed the data with contributions from SR, HN, BC, SM, SMN and TI. SR established GUV preparation method. WR performed in-cell CID experiment and analyzed the data. RY performed biochemical experiments. YOT performed EM under supervision by MM. OHA and CTL built and analyzed computational models. DN, DAK, and BC provided cytoskeleton proteins. TM provided benzylguanine-conjugated lipid. HTM wrote the manuscript in consultation with TI. HTM, SR, and TI edited the manuscript. All the authors contributed to the final version of the manuscript.

Data Availability

The datasets generated during this study are available from the corresponding author upon request.

Figure Legends

Fig. 1. Reversible and asymmetric control of protein localization with iLID-SspB within GUVs. (A) Schematic representation of iLID-SspB reaction with global light stimulation. iLID was tethered on the membrane via the interaction between SNAP-tag and benzylguanine-conjugated lipids. Upon blue light illumination, Jα helix of iLID extends to expose the binding site for SspB, whereas in the dark, iLID reverses to its closed state and releases SspB. (B) Representative images of iLID-YFP-SNAP and mCherry-SspB. Scale bar, 10 µm. Blue bar indicates the period of blue light illumination. (C) Time course of membrane/lumen ratio of mCherry-SspB signal (n=5). Error bars indicate 95% CI. Blue area indicates the period of blue light stimulation. (D) Schematic representation of iLID-SspB reaction with local light stimulation. (E) Representative images of mCherry-SspB. Scale bar, 10 µm. Yellow box indicates the area of blue light illumination. (F) Membrane/lumen ratio of mCherry-SspB for the representative image shown. The distance is measured from the center of blue light illumination along the perimeter of the GUV. (G) Representative image and kymograph of repetitive and reversible SspB translocation. Kymograph shows membrane signal of mCherry-SspB.

1167 **Fig. 2. Reversible light control of actin cytoskeleton within GUVs.** (A) Bulk pyrene actin
1168 polymerization assay with 1 µM actin (5% pyrene-labeled), 10 nM Arp2/3, and 100 nM NPFs. (-
1169 NPF) represents actin and Arp2/3 only condition. (B) Schematic representation of light-inducible
1170 actin polymerization. Translocation of pVCA-SspB-mCherry increases local concentration of pVCA
1171 on the membrane and enhances actin polymerization. (C) Representative images of pVCA-SspB-
1172 mCherry and Alexa 647 actin. Blue bar indicates the period of blue light illumination. (D) Time
1173 course of membrane/lumen ratio of mCherry and Alexa 647 actin in (C) and fig. S9. pVCA
1174 +Arp2/3+Light: full set of components (n=4). -Light: no blue light stimulation (n=3). -pVCA: pVCA-
1175 SspB-mCherry was replaced with mCherry-SspB (n=4). -Arp2/3: Arp2/3 was omitted (n=4). In (E)–
1176 (H), pVCA-SspB-mCherry was constitutively anchored to the membrane via SsrA-SNAP. (E)
1177 Pharmacological perturbation of membrane-associated actin. DMSO (n=8), Jasplakinolide (Jasp,
1178 n=10), Latrunculin A (LatA, n=9). (F) Time course of normalized membrane/lumen ratio of Alexa-
1179 647 actin in (E). The values were normalized by time=0. (G) FRAP analysis of membrane
1180 fluorescence of mCherry and Alexa 647 actin in fig. S11. The values were normalized by time=0.
1181 Sample sizes are listed in fig. S11A. (H) Electron microscopy (EM) images of actin filaments in the
1182 presence and absence of pVCA. Scale bar indicates 500 nm. (I) Representative images of
1183 reversible actin polymerization. Blue bars indicate the period of blue light illumination. (J) Time
1184 course of membrane/lumen ratio of pVCA-SspB-mCherry and Alexa 647-labeled actin in (F). (D,
1185 F, G) Error bars indicate 95% CI.
1186
1187 **Fig. 3. Asymmetric light control of actin cytoskeleton within GUVs.** (A) Schematic representation
1188 of iLID-SspB reaction with local light stimulation. (B, D) Representative images of light-inducible
1189 asymmetric actin polymerization. Yellow boxes indicate the area of blue light illumination. (C, E)
1190 Kymograph of membrane pVCA-SspB and actin signals. Blue bars indicate the period of blue light
1191 illumination. Triangles indicate timepoints represented in (B, D).
1192
1193 **Fig. 4. mDia1-mediated actin polymerization drives protrusive movement of GUVs.** (A)
1194 Schematic representation of light-inducible membrane protrusion driven by pVCA and mDia1-
1195 mediated actin polymerization. (B) Representative images of pVCA-mDia1-mediated movement
1196 of GUVs. Yellow boxes indicate the area of blue light stimulation. Dotted line shows the initial
1197 position of the GUV. (C) Representative images of iLID-EYFP-SNAP showing the increase in
1198 adhesive area and vesicle deformation into dome-like shape. X-y images show the confocal plane
1199 right above the bottom substrate. Z-x and y-z images are reconstituted from z-stack. Dotted line
1200 shows the adhesive area of the previous images. (D) Color-coded boundaries of GUVs. The data
1201 correspond as follows. Left: Fig. 4B. Middle: fig. S16A. Right: fig. S16B. (E, F) Kymographs of
1202 membrane signal of mCherry and actin Alexa-647 and membrane protrusions. Triangles in (E)
1203 indicate the timepoints represented in (B, C). Data of (E) and (F) correspond to Fig. 4 (B) and fig.
1204 S16A, respectively. (G) Distance the front (illuminated) side of GUV membrane moved forward.

pVCA+mDia1 (1 μM GST-pVCA-SspB-mCherry + 1 μM mCherry-SspB-mDia1, n=14 vesicles), mDia1 (1 μM mCherry-SspB-mDia1, n=12 vesicles), pVCA (1 μM GST-pVCA-SspB-mCherry, n=12 vesicles). Error bars indicate 95% CI (H, I) Quantification of the initial velocity and the distance the front side of GUV membrane moved forward. P values of Steel-Dwass test (two sided) are indicated. pVCA + mDia1: n=22 vesicles. mDia1: n=11 vesicles. pVCA: n=12 vesicles. Box whisker plots represent median, 1st, 3rd quartiles and 1.5×inter-quartile range. (J~~H~~) Distance the front (illuminated) side of GUV membrane moved forward. DMSO (n=9 vesicles), 30 μM LatA (Latrunculin A) (n=10 vesicles). DMSO, ΔDAD: mCherry-SspB-mDia1 (FH1-FH2-DAD) was replaced with mCherry-SspB-mDia1(FH1-FH2) (n=13 vesicles). 30 μM SMIFH2 (n=6 vesicles). Error bars indicate 95% CI. (H, I) Quantification of the initial velocity and the distance the front side of GUV membrane moved forward. P values of Steel-Dwass test (two sided) are indicated. pVCA + mDia1: n=22 vesicles. mDia1: n=11 vesicles. pVCA: n=12 vesicles. Box whisker plots represent median, 1st, 3rd quartiles and 1.5×inter-quartile range. (K) A GUV deformed into dome-like shape after movement. Upper images: before light stimulation. Lower images: after light stimulation. The data corresponds to fig. S16C.

fig. S1. Proteins purified in this study. (A) SDS-PAGE results of purified proteins. Blue: Coomassie brilliant blue staining. Gray: SYPRO Ruby staining. Most mCherry-tagged proteins show two extra bands due to a known chromophore cleavage reaction during the boiling process (*148*, *149*). (B) Domain structures of NPFs used in this study.

fig. S2. Optimization of membrane anchoring of iLID. (A),(D),(G),(I): Schematic representations of membrane anchoring of iLID. (B),(C),(E),(F),(H),(J): Confocal images of iLID variants and mCherry-SspB. (B) His-tag Ni-NTA pair caused non-specific membrane recruitment of SspB. This is possibly caused by the presence of 2×Strep-iLID-YFP-6×His because mCherry-SspB itself did not show non-specific binding to the membrane of 5%Ni-NTA DGS/95%POPC (C). (E),(F) MARCKS-ED peptide requires high percentage of PS and PEGylated-lipids to reduce non-specific binding of SspB. (H) Biotin-StrepTactin-Streptag also caused non-specific membrane binding of SspB. (J) The data correspond with Fig. 1B.

fig. S3. Asymmetric control of protein localization with iLID-SspB within GUVs. (A) Time course of membrane/lumen ratio of mCherry-SspB signal in the illuminated area (n=6). Error bars indicate 95% CI. Blue area indicates the time window of blue light stimulation. The data corresponds to Fig. 1E and F. (B, C) Confocal images and time course of membrane/lumen ratio of mCherry-SspB signal responding to repetitive local light illuminations. The data corresponds to Fig. 1G.

1242 **fig. S4. Optimization of ActA-SspB.** (A) Pyrene actin polymerization assay. The reaction was
1243 performed with 1 μM actin (5% pyrene labeled), 10 nM Arp2/3, and 100 nM ActA variants or GST-
1244 VCA. (B) Fluorescence intensity/time in 0–6 min of (A) was plotted as bar chart. (C–E) Light-
1245 inducible local membrane recruitment of ActA (C) Confocal images of ActA translocation. Yellow
1246 boxes indicate the area of blue light illumination. (D) Time course of membrane/lumen ratio of
1247 ActA-SspB variants (n≥5 for each variant). Error bars indicate 95% CI. Blue bar indicates the time
1248 window of blue light stimulation. (E) Average membrane/lumen ratio of mCherry signal. In each
1249 condition, left and right bars indicate before and after light stimulation, respectively. The
1250 numbers on the bar chart indicate the fold change after stimulation.
1251
1252 **fig. S5. Light-inducible actin polymerization with global ActA membrane recruitment.** iLID-EYFP-
1253 MARCKS (5 μM), ActA-SspBnano-mCherry (2 μM), actin (1.5 μM, 10% Alexa-647 labeled), and
1254 Arp2/3 (150 nM) were encapsulated in GUVs containing 60 mol% POPC/40 mol% POPS. Blue light
1255 was applied to the entire GUV. (A) Representative images of ActA(1–183)-SspB(nano)-mCherry
1256 and actin Alexa-647. All components (n=4): w/o ActA: ActA(1–183)-SspB(nano)-mCherry was
1257 replaced with mCherry-SspB(micro) (n=3), w/o Arp2/3: Arp2/3 was omitted (n=3). No Light: no
1258 blue light stimulation (n=3). (B, C) Time course of membrane/lumen ratio of mCherry and actin
1259 Alexa 647. (D) Bar chart of membrane/lumen ratio of actin Alexa 647 before (0 min) and after (40
1260 min) light stimulation. Error bars indicate 95% CI.
1261
1262 **fig. S6. Asymmetric ActA membrane recruitment fails to induce directed actin polarization**
1263 **toward local light illumination.** iLID-EYFP-MARCKS (5 μM), ActA-SspBnano-mCherry (2 μM), actin
1264 (1.5 μM, 10% Alexa-647 labeled), and Arp2/3 (150 nM), 1 mM ATP were encapsulated in GUVs
1265 containing 60 mol% POPC/40 mol% POPS. Yellow boxes indicate the area of blue light illumination.
1266 Although ActA creates asymmetric distribution, actin patches randomly distributed due to the
1267 diffusion on the membrane.
1268
1269 **fig. S7. Global ActA membrane recruitment fails to induce actin polymerization on the**
1270 **membrane in the presence of profilin, cofilin, and capping protein.** 15 μM iLID-YFP-MARCKS, 5
1271 μM ActA(1-183)-SspB(nano)-mCherry, 7.5 μM actin (10% Alexa 647 labeled), 150 nM Arp2/3, 3
1272 μM profilin, cofilin, and capping protein were encapsulated in GUVs containing 60 mol% POPC/40
1273 mol% POPS. Blue bars indicate the period of blue light illumination.
1274
1275 **fig. S8. Biochemical characterization of actin and actin-binding proteins used in this study.**
1276 (A, B) Ultracentrifuge assay. After 30 min actin polymerization reaction at RT, the solutions were
1277 ultracentrifuged 100,000×g, 60 min, at RT. Proteins and concentrations used: 7.5 μM actin (10%
1278 Alexa-488 labeled), 3 μM profilin, 4 μM cofilin, 50 nM capping protein, 150 nM Arp2/3, 1 μM
1279 GST-pVCA-SspB-mCherry, 1 μM mCherry-SspB-mDia1. G-buffer: 2 mM Tris-HCl (pH 7.5), 0.2 mM

1280 ATP, 0.1 mM $CaCl_2$, 0.5 mM DTT, 1 mM NaN_3. KMEI-S buffer: .10mM imidazole (pH 7.0), 50mM
1281 KCl, 1mM $MgCl_2$, 1mM EGTA, 240 mM sucrose (sucrose was added to mimic the buffer conditions
1282 in GUV experiments). (C–F) Pyrene actin polymerization assay. The reactions were performed
1283 with 2 µM actin (5% pyrene labeled) at RT. (C, D) 10 nM Arp2/3, and 100 nM NPFs. (-) represents
1284 actin and Arp2/3 only condition. (E) The reactions were performed with the indicated factors. (F)
1285 50 nM capping protein, 150 nM Arp2/3, 3 µM profilin, 1 µM mCherry-SspB-mDia1, 1 µM GST-
1286 pVCA-SspB-mCherry. (-) represents actin only condition.
1287
1288 **fig. S9. Light control of actin cytoskeleton with pVCA-SspB-mCherry.** The data correspond to Fig.
1289 2C–E. (+) condition contains 15 µM iLID-YFP-MARCKS, 4.2 µM pVCA-SspB(nano)-mCherry, 7.5 µM
1290 actin (10% Alexa 647 labeled), 150 nM Arp2/3, 100 nM capping protein, 3 µM profilin, 4 µM cofilin,
1291 and 1 mM ATP. In (-light) and (-Arp2/3) conditions, blue light illumination or Arp2/3 was omitted
1292 from (+pVCA +Arp2/3 +Light) condition, respectively. In (-pVCA) condition, pVCA-SspB(nano)-
1293 mCherry was replaced with mCherry-SspB(micro).
1294
1295 **fig. S10. Pharmacological perturbation of membrane-associated actin assemblies.** (A)
1296 Schematic representation of constitutive tethering of NPFs. SspB-fused NPFs (pVCA and/or
1297 mDia1) were tethered to the GUV membrane via the SsrA–SNAP/BG-lipid system. (B)
1298 Representative confocal images of membrane-associated actin assemblies formed by pVCA,
1299 mDia1, or their combination. Scale bars, 5 µm. (C) Quantification of the initial membrane/lumen
1300 fluorescence intensity ratio for mCherry and actin Alexa-647. pVCA: n=27 vesicles. mDia1: n=23
1301 vesicles. pVCA + mDia1: n=27 vesicles. Box whisker plots represent median, 1st, 3rd quartiles and
1302 1.5×inter-quartile range. (D) Representative images before (0 min) and after (24 min) treatment
1303 with DMSO, 50 µM Latrunculin A, or 50 µM Jasplakinolide. Scale bars, 5 µm. (E) Time courses of
1304 membrane/lumen ratio and normalized membrane/lumen ratio of actin Alexa-647. (F) Time
1305 courses of normalized membrane/lumen ratio of actin Alexa-647 for each NPF condition. The y-
1306 axis is shown on a logarithmic scale. (E, F) Error bars indicate 95% CI. (G) Representative images
1307 showing membrane deformation after Jasplakinolide treatment. Scale bars, 10 µm. mCherry-
1308 SspB-mDia1-6×His was used as mDia1 in this figure.
1309
1310 **fig. S11. Fluorescence recovery after photobleaching (FRAP) analysis of membrane-associated**
1311 **NPFs and actin.** (A) Summary table of proteins included in each conditions. In FRAP analysis, SspB-
1312 fused NPFs (pVCA and/or mDia1) were tethered to the GUV membrane via the SsrA–SNAP/BG-
1313 lipid system. (B, C) Representative confocal images of mCherry-tagged NPFs and actin Alexa-647.
1314 The white dashed box indicates the photobleached region. Scale bars, 5 µm. (D, E) Time course
1315 of mCherry and Alexa-647 fluorescence recovery at the bleached region. Fluorescence intensities
1316 were normalized to those of a non-bleached region to compensate for photobleaching during

1317 image acquisition. The data from Fig. 1G are reproduced to facilitate direct comparison with the
1318 other conditions presented in this figure.
1319
1320 **fig. S12. Electron microscopy (EM) analysis of actin filaments.** Ultrastructure of small unilamellar
1321 vesicles (SUVs) and actin filaments were analyzed by negative staining electron microscopy. (A)
1322 Representative EM images of SUVs alone. (B) Representative images of Y-junctions formed in the
1323 presence of pVCA, Arp2/3, capping protein (CP), profilin, and cofilin. (C) Negative control sample
1324 lacking pVCA (Arp2/3, CP, profilin, and cofilin only). (B, C) To reduce filament overlap, the
1325 polymerization reactions were diluted 10-fold prior to deposition onto EM grids. (D)
1326 Representative EM images of actin assemblies formed with pVCA or the corresponding negative
1327 control lacking pVCA. (E) Representative EM images of actin assemblies formed with pVCA +
1328 mDia1, mDia1 alone, or the corresponding negative control lacking mDia1. All samples were
1329 deposited onto EM grids and negatively stained prior to imaging. Scale bars are shown in each
1330 panel. mCherry-SspB-mDia1-6×His was used as mDia1 in this figure.
1331
1332 **fig. S13. Representative images of reversible actin polymerization.** Confocal images and time
1333 course of membrane/lumen ratio of pVCA-SspB-mCherry and Alexa 647-labeld actin. Blue bars
1334 on images and blue regions in graphs indicate timepoints with blue light illumination. This figure
1335 corresponds with Fig. 2F, G.
1336
1337 **fig. S14. Asymmetric actin polymerization induced by pVCA.** (A) Confocal images of local pVCA
1338 recruitment and actin polymerization. Yellow boxes indicate areas of blue light illumination. (B)
1339 Membrane/lumen ratio of mCherry-tagged pVCA and actin Alexa-647 for the images in (A). The
1340 distance is measured from the center of blue light illumination along the perimeter of the GUV.
1341 (A, B) The data corresponds to Fig. 3B and C. (C) Confocal images of local pVCA recruitment
1342 accompanied by vesicle movement toward light stimulation. Gray scaled images were created by
1343 averaging pVCA and actin images. Dotted circles indicate positions of vesicles in the images of
1344 one above.
1345
1346 **fig. S15. Quantitative analysis of mDia1-induced filopodia formation in Cos7 cells.** (A) Schematic
1347 representation of chemically-inducible mDia1 translocation and membrane protrusions. (B, C)
1348 Confocal images of plasma membrane recruitment of mDia1 and subsequent filopodia formation.
1349 Cos7 cells were transfected with Lyn-ECFP-FRB, Lifeact-mCherry, and either of YFP-FKBP or YFP-
1350 FKBP-mDia1. At time 0, 100 nM rapamycin was added. Green: YFP-FKBP or YFP-FKBP-mDia1.
1351 Magenta: Lifeact-mCherry. (B) YFP-FKBP control. (C) YFP-FKBP-mDia1. (D) Zoomed-up view of
1352 filopodia extension. Images were acquired every 1.5 minutes. The bottom is merged image. (E)
1353 Quantification of mDia1-induced filopodia. Number of filopodia whose length is longer than 15
1354 µm was counted. Box whisker plots represent median, 1st, 3rd quartiles and 1.5×inter-quartile

range. P-values: ****: < 0.0001. Wilcoxon rank sum test. YF (YFP-FKBP): n=36 cells. YF-mDia1 (YFP-FKBP-mDia1): n=33 cells. (F–H) Quantification of the phenotypes observed after plasma membrane translocation of mDia1 (n=159 cells), pVCA (n=142 cells), Tiam1 (Rac1 GEF) (n=67 cells), and control protein YFP-FKBP (n=44 cells).

fig. S16. mDia1-mediated GUV movement and the comparison between mDia1 and pVCA + mDia1 system. (A) Representative images of mDia1-mediated GUV movement. Yellow boxes indicate the area of blue light stimulation. Dotted lines indicate the initial position of the GUV. (B, C) Time course of the distance the front (illuminated) side of GUV membrane moved forward. Each line represents each GUV. Insets show the initial response.

fig. S17. Local protrusions in pVCA + mDia1 GUVs. Representative images of local protrusions seen in pVCA + mDia1 GUVs. Yellow boxes indicate the area of blue light stimulation. Dotted lines indicate the initial position of the GUV. White arrows indicate where local protrusions arose.

fig. S18. Lack of vesicle movement and shape change with mCherry-SspB. With pVCA-SspB-mCherry and mCherry-SspB-mDia1 being replaced with mCherry-SspB, GUVs neither moved nor changed their shape after blue light illumination. (A) Time course of the distance the front (illuminated) side of GUV membrane moved forward. pVCA + mDia1 GUVs: n=6 vesicles. SspB GUVs: n=4 vesicles. Error bars indicate 95% CI. (B) 3D reconstitution of iLID-YFP-SNAP images before and after blue light illumination.

Fig. S19. Relationship between vesicle motion and biophysical parameters. (A) Relationship between initial velocity (average velocity over the first 5 minutes) and net displacement after 30 minutes of GUV forward movement. (B, C) Biophysical parameters are plotted against initial velocity and displacement are plotted in (B) and (C), respectively. R and p indicate Pearson's correlation coefficient and its p-value.

fig. S20. Representative images of pVCA-mDia1-mediated movement of GUVs. (A, B) Representative images of pVCA-mDia1-mediated movement of GUVs. Yellow boxes indicate the area of blue light stimulation. Dotted lines indicate the initial position of the GUV. White arrows indicate where local protrusions arose. (C) Distance the front side of GUV membrane moved forward. Data was quantified from the images of (B). Blue areas indicate the periods of blue light stimulation.

Fig. S21. Computational modeling of actin network dynamics underlying membrane deformation. (A, B) Snapshots showing actin filaments at the leading edge of the membrane after 5 s of simulation. Actin filaments are shown in green, pVCA-Arp2/3 is shown in red, mDia1 is

shown in orange, and Arp2/3 is shown in magenta. The membrane location at t = 0 is shown with the cyan dotted line to highlight the extent of membrane deformation. Simulations without and with inter-filament steric interactions are shown in A and B, respectively. (C, D) Box-whisker plots showing distributions of the membrane extension for the different actin-binding proteins. Results for networks without and with inter-filament steric interactions are shown in A and B, respectively. Each box plot is constructed using 20 independent simulation trajectories. Error bars represent standard deviation about the mean.

Movie S1

Representative movie of repetitive and reversible SspB translocation. The data corresponds to Fig. 1G. Time in min:sec. Yellow regions indicate the area of blue light stimulations.

Movie S2

A rare example where ActA induced actin polymerization in the direction of light stimulus. The data corresponds the leftmost images in Fig. S6. Red: ActA-SspB(nano)-mCherry. Magenta: Alexa 647-labeled actin. Time in hr:min:sec. Yellow regions indicate the area of blue light stimulation.

Movie S3

Representative movie of global membrane recruitment of pVCA-SspB-mCherry. The data corresponds to Fig. 2C and "pVCA +Arp2/3 +Light" in Fig. S9. Red: pVCA-SspB-mCherry. Magenta: Alexa 647-labeled actin. Time in hr:min:sec. The label "Light" indicates when blue light stimulation is applied to the entire GUV.

Movie S4

Representative movie of global and reversible membrane recruitment of pVCA-SspB-mCherry. The data corresponds to Fig. 2I~~F~~ and S13. Red: pVCA-SspB-mCherry. Magenta: Alexa 647-labeled actin. Time in hr:min:sec. The label "Light" indicates when blue light stimulation is applied to the entire GUV.

Movie S5

Representative movie of asymmetric membrane recruitment of pVCA-SspB-mCherry. The data corresponds to Fig. 3B and C. Red: pVCA-SspB-mCherry. Magenta: Alexa 647-labeled actin. Time in hr:min:sec. Yellow regions indicate the area of blue light stimulation.

Movie S6

1429 Representative movie of asymmetric and reversible membrane recruitment of pVCA-SspB-
1430 mCherry. The data corresponds to Fig. 3D and E. Red: pVCA-SspB-mCherry. Magenta: Alexa 647-
1431 labeled actin. Time in hr:min:sec. Yellow regions indicate the area of blue light stimulation.
1432
1433 **Movie S7**
1434 Representative movie of pVCA-mDia1-mediated movement of GUV. The data corresponds to Fig.
1435 4B and E. Red: pVCA-SspB-mCherry and mCherry-SspB-mDia1. Magenta: Alexa 647-labeled actin.
1436 Time in hr:min:sec. Yellow regions indicate the area of blue light stimulation.
1437
1438 **Movie S8**
1439 Representative movie of local protrusions seen in pVCA + mDia1 GUVs. The data corresponds to
1440 Fig. S17. Red: pVCA-SspB-mCherry and mCherry-SspB-mDia1. Magenta: Alexa 647-labeled actin.
1441 Time in hr:min:sec. Yellow regions indicate the area of blue light stimulation. In the zoomed-in
1442 view, the relative movement of the GUV was subtracted to better highlight the local protrusions.
1443
1444 **Movie S9**
1445 Representative movie of pVCA-mDia1-mediated movement of GUV. The data corresponds to Fig.
1446 4F and S20A. Red: pVCA-SspB-mCherry and mCherry-SspB-mDia1. Magenta: Alexa 647-labeled
1447 actin. Time in hr:min:sec. Yellow regions indicate the area of blue light stimulation.
1448
1449 **Movie S10**
1450 Representative movie of pVCA-mDia1-mediated movement of GUV. The data corresponds to Fig.
1451 S20B. Red: pVCA-SspB-mCherry and mCherry-SspB-mDia1. Magenta: Alexa 647-labeled actin.
1452 Time in hr:min:sec. Yellow regions indicate the area of blue light stimulation.
1453
1454 **Movie S11**
1455 Representative simulation movies in the absence of inter-filament steric interactions. Actin
1456 filaments are shown in green, pVCA–Arp2/3 in red, mDia1 in orange, and Arp2/3 in magenta. The
1457 membrane position at t = 0 is marked by a cyan line to indicate the extent of membrane
1458 deformation.
1459
1460 **Movie S12**
1461 Representative simulation movies in the presence of inter-filament steric interactions. Actin
1462 filaments are shown in green, pVCA–Arp2/3 in red, mDia1 in orange, and Arp2/3 in magenta. The
1463 membrane position at t = 0 is marked by a cyan line to indicate the extent of membrane
1464 deformation.

References

1. M. Miyata, R. C. Robinson, T. Q. P. Uyeda, Y. Fukumori, S. ichi Fukushima, S. Haruta, M. Homma, K. Inaba, M. Ito, C. Kaito, K. Kato, T. Kenri, Y. Kinosita, S. Kojima, T. Minamino, H. Mori, S. Nakamura, D. Nakane, K. Nakayama, M. Nishiyama, S. Shibata, K. Shimabukuro, M. Tamakoshi, A. Taoka, Y. Tashiro, I. Tulum, H. Wada, K. ichi Wakabayashi, Tree of motility – A proposed history of motility systems in the tree of life. *Genes to Cells* **25**, 6–21 (2020).

2. K. Y. Wan, G. Jékely, Origins of eukaryotic excitability. *Phil. Trans. R. Soc. B* **376**, 20190758 (2021).

3. T. Froese, N. Virgo, T. Ikegami, Motility at the Origin of Life: Its Characterization and a Model. *Artificial Life* **20**, 55–76 (2014).

4. P. N. Devreotes, S. Bhattacharya, M. Edwards, P. A. Iglesias, T. Lampert, Y. Miao, Excitable Signal Transduction Networks in Directed Cell Migration. *Annu. Rev. Cell Dev. Biol.* **33**, 103–125 (2017).

5. L. K. Fritz-Laylin, The evolution of animal cell motility. *Current Biology* **30**, R477–R482 (2020).

6. S. SenGupta, C. A. Parent, J. E. Bear, The principles of directed cell migration. *Nat Rev Mol Cell Biol* **22**, 529–547 (2021).

7. Effects of Cytochalasins on Mammalian Cells | Nature. https://www.nature.com/articles/213261a0.

8. T. D. Pollard, S. Ito, CYTOPLASMIC FILAMENTS OF *AMOEBA PROTEUS*. *The Journal of Cell Biology* **46**, 267–289 (1970).

9. J. V. Small, G. Isenberg, J. E. Celis, Polarity of actin at the leading edge of cultured cells. *Nature* **272**, 638–639 (1978).

10. L. G. Tilney, S. Inoué, Acrosomal reaction of Thyone sperm. II. The kinetics and possible mechanism of acrosomal process elongation. *J Cell Biol* **93**, 820–827 (1982).

11. J. A. Theriot, The Polymerization Motor. *Traffic* **1**, 19–28 (2000).

12. T. D. Pollard, Landmarks in the discovery of a role for actin in cell locomotion. *Molecular Biology of the Cell*, 4 (2022).

13. P. Lappalainen, T. Kotila, A. Jégou, G. Romet-Lemonne, Biochemical and mechanical regulation of actin dynamics. *Nat Rev Mol Cell Biol*, doi: 10.1038/s41580-022-00508-4 (2022).

1496 14. T. Lämmermann, M. Sixt, Mechanical modes of 'amoeboid' cell migration. *Current Opinion*
1497 *in Cell Biology* **21**, 636–644 (2009).

1498 15. P. Friedl, K. Wolf, Plasticity of cell migration: a multiscale tuning model. *Journal of Cell*
1499 *Biology* **188**, 11–19 (2010).

1500 16. M. Garrido-Casado, G. Asensio-Juárez, M. Vicente-Manzanares, Nonmuscle Myosin II
1501 Regulation Directs Its Multiple Roles in Cell Migration and Division. *Annu Rev Cell Dev Biol*
1502 **37**, 285–310 (2021).

1503 17. D. Knecht, W. Loomis, Antisense RNA inactivation of myosin heavy chain gene expression in
1504 Dictyostelium discoideum. *Science* **236**, 1081–1086 (1987).

1505 18. A. De Lozanne, J. A. Spudich, Disruption of the Dictyostelium myosin heavy chain gene by
1506 homologous recombination. *Science* **236**, 1086–1091 (1987).

1507 19. A. B. Verkhovsky, T. M. Svitkina, G. G. Borisy, Self-polarization and directional motility of
1508 cytoplasm. *Current Biology* **9**, 11-S1 (1999).

1509 20. R. J. Eddy, L. M. Pierini, F. Matsumura, F. R. Maxfield, Ca2+-dependent myosin II activation
1510 is required for uropod retraction during neutrophil migration. *J Cell Sci* **113 (Pt 7)**, 1287–
1511 1298 (2000).

1512 21. T. Lämmermann, B. L. Bader, S. J. Monkley, T. Worbs, R. Wedlich-Söldner, K. Hirsch, M.
1513 Keller, R. Förster, D. R. Critchley, R. Fässler, M. Sixt, Rapid leukocyte migration by integrin-
1514 independent flowing and squeezing. *Nature* **453**, 51–55 (2008).

1515 22. A. Reversat, F. Gaertner, J. Merrin, J. Stopp, S. Tasciyan, J. Aguilera, I. de Vries, R. Hauschild,
1516 M. Hons, M. Piel, A. Callan-Jones, R. Voituriez, M. Sixt, Cellular locomotion using
1517 environmental topography. *Nature* **582**, 582–585 (2020).

1518 23. Y. I. Wu, D. Frey, O. I. Lungu, A. Jaehrig, I. Schlichting, B. Kuhlman, K. M. Hahn, A genetically
1519 encoded photoactivatable Rac controls the motility of living cells. *Nature* **461**, 104–108
1520 (2009).

1521 24. B. Lin, W. R. Holmes, C. J. Wang, T. Ueno, A. Harwell, L. Edelstein-Keshet, T. Inoue, A.
1522 Levchenko, Synthetic spatially graded Rac activation drives cell polarization and movement.
1523 *Proceedings of the National Academy of Sciences of the United States of America* **109**
1524 (2012).

1525 25. S. Nanda, A. Calderon, A. Sachan, T.-T. Duong, J. Koch, X. Xin, D. Solouk-Stahlberg, Y.-W. Wu,
1526 P. Nalbant, L. Dehmelt, Rho GTPase activity crosstalk mediated by Arhgef11 and Arhgef12
1527 coordinates cell protrusion-retraction cycles. *Nat Commun* **14**, 8356 (2023).

1528 26. L. A. Cameron, M. J. Footer, A. Van Oudenaarden, J. A. Theriot, Motility of ActA protein-
1529 coated microspheres driven by actin polymerization. *Proceedings of the National Academy*
1530 *of Sciences of the United States of America* **96**, 4908–4913 (1999).

1531 27. T. P. Loisel, R. Boujemaa, D. Pantaloni, M. Carlier, Reconstitution of actin-based motility of
1532 Listeria and Shigella using pure proteins. **401**, 613–616 (1999).

1533 28. A. Bernheim-Groswasser, S. Wiesner, R. M. Golsteyn, M.-F. Carlier, C. Sykes, The dynamics
1534 of actin-based motility depend on surface parameters. *Nature* **417**, 308–311 (2002).

1535 29. A. Mogilner, G. Oster, Force generation by actin polymerization II: The elastic ratchet and
1536 tethered filaments. *Biophysical Journal* **84**, 1591–1605 (2003).

1537 30. S. Wiesner, E. Helfer, D. Didry, G. Ducouret, F. Lafuma, M. F. Carlier, D. Pantaloni, A
1538 biomimetic motility assay provides insight into the mechanism of actin-based motility.
1539 *Journal of Cell Biology* **160**, 387–398 (2003).

1540 31. S. Romero, C. Le Clainche, D. Didry, C. Egile, D. Pantaloni, M. F. Carlier, Formin is a
1541 processive motor that requires profilin to accelerate actin assembly and associated ATP
1542 hydrolysis. *Cell* **119**, 419–429 (2004).

1543 32. C. Co, D. T. Wong, S. Gierke, V. Chang, J. Taunton, Mechanism of Actin Network Attachment
1544 to Moving Membranes: Barbed End Capture by N-WASP WH2 Domains. *Cell* **128**, 901–913
1545 (2007).

1546 33. O. Akin, R. D. Mullins, Capping Protein Increases the Rate of Actin-BasedMotility by
1547 Promoting Filament Nucleation by the Arp2/3 Complex. *Cell* **133**, 841–851 (2008).

1548 34. J. Prost, J.-F. Joanny, P. Lenz, C. Sykes, "The Physics Of Listeria Propulsion" in *Cell Motility*
1549 (Springer New York, New York, NY, 2008; https://doi.org/10.1007/978-0-387-73050-9_1),
1550 pp. 1–30.

1551 35. P. Bieling, S. D. Hansen, O. Akin, T.-D. Li, C. C. Hayden, D. A. Fletcher, R. D. Mullins, WH2 and
1552 proline-rich domains of WASP-family proteins collaborate to accelerate actin filament
1553 elongation. *EMBO J* **37**, 102–121 (2018).

1554 36. C. Guérin, A.-B. N'Diaye, L. Gressin, A. Mogilner, M. Théry, L. Blanchoin, A. Colin, Balancing
1555 limited resources in actin network competition. *Current Biology* **35**, 500-513.e5 (2025).

1556 37. S. Razavi, T. Inoue, "Chapter 22 - Reconstitution of membrane symmetry breaking" in
1557 *Plasma Membrane Shaping*, S. Suetsugu, Ed. (Academic Press, 2023;
1558 https://www.sciencedirect.com/science/article/pii/B9780323899116000273), pp. 333–353.

1559 38. R. Lopes Dos Santos, C. Campillo, Studying actin-induced cell shape changes using Giant
1560 Unilamellar Vesicles and reconstituted actin networks. *Biochemical Society Transactions* **50**,
1561 1527–1539 (2022).

39. F. C. Keber, E. Loiseau, T. Sanchez, S. J. DeCamp, L. Giomi, M. J. Bowick, M. C. Marchetti, Z. Dogic, A. R. Bausch, Topology and dynamics of active nematic vesicles. *Science* **345**, 1135–1139 (2014).

40. Y. Sato, Y. Hiratsuka, I. Kawamata, S. Murata, S. M. Nomura, Micrometer-sized molecular robot changes its shape in response to signal molecules. *Science Robotics* **2**, eaal3735 (2017).

41. K. Gavriljuk, B. Scocozza, F. Ghasemalizadeh, H. Seidel, A. P. Nandan, M. Campos-Medina, M. Schmick, A. Koseska, P. I. H. Bastiaens, A self-organized synthetic morphogenic liposome responds with shape changes to local light cues. *Nature Communications* **12**, 1548 (2021).

42. J. D. Cortese, B. Schwab, C. Frieden, E. L. Elson, Actin polymerization induces a shape change in actin-containing vesicles. *Proceedings of the National Academy of Sciences of the United States of America* **86**, 5773–5777 (1989).

43. H. Miyata, H. Hotani, Morphological changes in liposomes caused by polymerization of encapsulated actin and spontaneous formation of actin bundles. *Proceedings of the National Academy of Sciences of the United States of America* **89**, 11547–11551 (1992).

44. H. Miyata, S. Nishiyama, K. -i. Akashi, K. Kinosita, Protrusive growth from giant liposomes driven by actin polymerization. *Proceedings of the National Academy of Sciences* **96**, 2048–2053 (1999).

45. M. Honda, K. Takiguchi, S. Ishikawa, H. Hotani, Morphogenesis of liposomes encapsulating actin depends on the type of actin-crosslinking. *Journal of Molecular Biology* **287**, 293–300 (1999).

46. L. L. Pontani, J. Van Der Gucht, G. Salbreux, J. Heuvingh, J. F. Joanny, C. Sykes, Reconstitution of an actin cortex inside a liposome. *Biophysical Journal* **96**, 192–198 (2009).

47. K. Dürre, F. C. Keber, P. Bleicher, F. Brauns, C. J. Cyron, J. Faix, A. R. Bausch, Capping protein-controlled actin polymerization shapes lipid membranes. *Nature Communications*, doi: 10.1038/s41467-018-03918-1 (2018).

48. Y. Bashirzadeh, S. A. Redford, C. Lorpaiboon, A. Groaz, H. Moghimianavval, T. Litschel, P. Schwille, G. M. Hocky, A. R. Dinner, A. P. Liu, Actin crosslinker competition and sorting drive emergent GUV size-dependent actin network architecture. *Commun Biol* **4**, 1136 (2021).

49. N. H. Wubshet, Y. Bashirzadeh, A. P. Liu, Fascin-induced actin protrusions are suppressed by dendritic networks in giant unilamellar vesicles. *MBoC* **32**, 1634–1640 (2021).

50. T. Litschel, C. F. Kelley, D. Holz, M. Adeli Koudehi, S. K. Vogel, L. Burbaum, N. Mizuno, D. Vavylonis, P. Schwille, Reconstitution of contractile actomyosin rings in vesicles. *Nature Communications* **12**, 2254 (2021).

1596 51. R. Sakamoto, M. P. Murrell, Composite branched and linear F-actin maximize myosin-
1597 induced membrane shape changes in a biomimetic cell model. *Commun Biol* **7**, 1–12 (2024).

1598 52. R. Sakamoto, D. S. Banerjee, V. Yadav, S. Chen, M. L. Gardel, C. Sykes, S. Banerjee, M. P.
1599 Murrell, Membrane tension induces F-actin reorganization and flow in a biomimetic model
1600 cortex. *Commun Biol* **6**, 325 (2023).

1601 53. K. Y. Lee, S. J. Park, K. A. Lee, S. H. Kim, H. Kim, Y. Meroz, L. Mahadevan, K. H. Jung, T. K.
1602 Ahn, K. K. Parker, K. Shin, Photosynthetic artificial organelles sustain and control ATP-
1603 dependent reactions in a protocellular system. *Nature Biotechnology* **36**, 530–535 (2018).

1604 54. S. Tanaka, K. Takiguchi, M. Hayashi, Repetitive stretching of giant liposomes utilizing the
1605 nematic alignment of confined actin. *Communications Physics* **1** (2018).

1606 55. A. Fink, C. R. Doll, A. Yagüe Relimpio, Y. Dreher, J. P. Spatz, K. Göpfrich, E. A. Cavalcanti-
1607 Adam, Extracellular Cues Govern Shape and Cytoskeletal Organization in Giant Unilamellar
1608 Lipid Vesicles. *ACS Synth. Biol.*, acssynbio.2c00516 (2023).

1609 56. S. Razavi, F. Wong, B. Abubaker-Sharif, H. T. Matsubayashi, H. Nakamura, N. T. H. Nguyen,
1610 D. N. Robinson, B. Chen, P. A. Iglesias, T. Inoue, Synthetic control of actin polymerization
1611 and symmetry breaking in active protocells. *Sci Adv* **10**, eadk9731 (2024).

1612 57. K. Zhang, B. Cui, Optogenetic control of intracellular signaling pathways. *Trends in*
1613 *Biotechnology* **33**, 92–100 (2015).

1614 58. A. Pudasaini, K. K. El-Arab, B. D. Zoltowski, LOV-based optogenetic devices: Light-driven
1615 modules to impart photoregulated control of cellular signaling. *Frontiers in Molecular*
1616 *Biosciences* **2**, 1–15 (2015).

1617 59. J. Niu, M. Ben Johny, I. E. Dick, T. Inoue, Following Optogenetic Dimerizers and Quantitative
1618 Prospects. *Biophysical Journal* **111**, 1132–1140 (2016).

1619 60. G. Guntas, R. A. Hallett, S. P. Zimmerman, T. Williams, H. Yumerefendi, J. E. Bear, B.
1620 Kuhlman, Engineering an improved light-induced dimer (iLID) for controlling the localization
1621 and activity of signaling proteins. *Proceedings of the National Academy of Sciences of the*
1622 *United States of America* **112**, 112–117 (2015).

1623 61. A. Uyeda, T. Watanabe, T. Hohsaka, T. Matsuura, Different protein localizations on the inner
1624 and outer leaflet of cell-sized liposomes using cell-free protein synthesis. *Synthetic Biology*
1625 **3**, ysy007 (2018).

1626 62. A. K. Rudd, J. M. Valls Cuevas, N. K. Devaraj, SNAP-Tag-Reactive Lipid Anchors Enable
1627 Targeted and Spatiotemporally Controlled Localization of Proteins to Phospholipid
1628 Membranes. *J. Am. Chem. Soc.* **137**, 4884–4887 (2015).

1629 63. D. Scherfeld, N. Kahya, P. Schwille, Lipid dynamics and domain formation in model
1630 membranes composed of ternary mixtures of unsaturated and saturated
1631 phosphatidylcholines and cholesterol. *Biophysical journal* **85**, 3758–3768 (2003).

1632 64. F. A. Thomas, I. Visco, Z. Petrášek, F. Heinemann, P. Schwille, Diffusion coefficients and
1633 dissociation constants of enhanced green fluorescent protein binding to free standing
1634 membranes. *Data in Brief* **5**, 537–541 (2015).

1635 65. M. Frick, K. Schmidt, B. J. Nichols, Modulation of Lateral Diffusion in the Plasma Membrane
1636 by Protein Density. *Current Biology* **17**, 462–467 (2007).

1637 66. R. D. Mullins, P. Bieling, D. A. Fletcher, From solution to surface to filament: actin flux into
1638 branched networks. *Biophys Rev* **10**, 1537–1551 (2018).

1639 67. L. B. Case, X. Zhang, J. A. Ditlev, M. K. Rosen, Stoichiometry controls activity of phase-
1640 separated clusters of actin signaling proteins. *Science* **363**, 1093–1097 (2019).

1641 68. K. Yamamoto, M. Miyazaki, Optogenetic actin network assembly on lipid bilayer uncovers
1642 the network density-dependent functions of actin-binding proteins. [Preprint] (2024).
1643 https://doi.org/10.1101/2024.12.25.630233.

1644 69. H. Nakamura, E. Rho, C. T. Lee, K. Itoh, D. Deng, S. Watanabe, S. Razavi, H. T. Matsubayashi,
1645 C. Zhu, E. Jung, P. Rangamani, S. Watanabe, T. Inoue, ActuAtor, a Listeria-inspired molecular
1646 tool for physical manipulation of intracellular organizations through de novo actin
1647 polymerization. *Cell Reports* **42**, 113089 (2023).

1648 70. S. Shekhar, M.-F. Carlier, Enhanced Depolymerization of Actin Filaments by ADF/Cofilin and
1649 Monomer Funneling by Capping Protein Cooperate to Accelerate Barbed-End Growth.
1650 *Current Biology* **27**, 1990-1998.e5 (2017).

1651 71. A. Colin, T. Kotila, C. Guérin, M. Orhant-Prioux, B. Vianay, A. Mogilner, P. Lappalainen, M.
1652 Théry, L. Blanchoin, Recycling of the actin monomer pool limits the lifetime of network
1653 turnover. *The EMBO Journal* **42**, e112717 (2023).

1654 72. H. Miki, K. Miura, T. Takenawa, N-WASP, a novel actin-depolymerizing protein, regulates
1655 the cortical cytoskeletal rearrangement in a PIP2-dependent manner downstream of
1656 tyrosine kinases. *The EMBO Journal* **15**, 5326–5335 (1996).

1657 73. R. Rohatgi, L. Ma, H. Miki, M. Lopez, T. Kirchhausen, T. Takenawa, M. W. Kirschner, The
1658 Interaction between N-WASP and the Arp2/3 Complex Links Cdc42-Dependent Signals to
1659 Actin Assembly. *Cell* **97**, 221–231 (1999).

1660 74. O. D. Weiner, G. Servant, M. D. Welch, T. J. Mitchison, J. W. Sedat, H. R. Bourne, Spatial
1661 control of actin polymerization during neutrophil chemotaxis. *Nature Cell Biology* **1**, 75–81
1662 (1999).

1663 75. O. D. Weiner, M. C. Rentel, A. Ott, G. E. Brown, M. Jedrychowski, M. B. Yaffe, S. P. Gygi, L. C.
1664 Cantley, H. R. Bourne, M. W. Kirschner, Hem-1 Complexes Are Essential for Rac Activation,
1665 Actin Polymerization, and Myosin Regulation during Neutrophil Chemotaxis. *PLoS Biol* **4**,
1666 e38 (2006).

1667 76. A. Kawska, K. Carvalho, J. Manzi, R. Boujemaa-Paterski, L. Blanchoin, J.-L. Martiel, C. Sykes,
1668 How actin network dynamics control the onset of actin-based motility. *Proceedings of the*
1669 *National Academy of Sciences* **109**, 14440–14445 (2012).

1670 77. K. B. Velle, L. K. Fritz-Laylin, Diversity and evolution of actin-dependent phenotypes. *Current*
1671 *Opinion in Genetics and Development* **58–59**, 40–48 (2019).

1672 78. E. D. Goley, M. D. Welch, The ARP2/3 complex: An actin nucleator comes of age. *Nature*
1673 *Reviews Molecular Cell Biology* **7**, 713–726 (2006).

1674 79. D. A. Valencia, M. E. Quinlan, Formins. *Current Biology* **31**, R517–R522 (2021).

1675 80. D. R. Kovar, E. S. Harris, R. Mahaffy, H. N. Higgs, T. D. Pollard, Control of the Assembly of
1676 ATP- and ADP-Actin by Formins and Profilin. *Cell* **124**, 423–435 (2006).

1677 81. J. Funk, F. Merino, L. Venkova, L. Heydenreich, J. Kierfeld, P. Vargas, S. Raunser, M. Piel, P.
1678 Bieling, Profilin and formin constitute a pacemaker system for robust actin filament growth.
1679 *eLife* **8**, e50963 (2019).

1680 82. S. Dmitrieff, F. Nédélec, Amplification of actin polymerization forces. *Journal of Cell Biology*
1681 **212**, 763–766 (2016).

1682 83. R. DeRose, T. Miyamoto, T. Inoue, Manipulating signaling at will: chemically-inducible
1683 dimerization (CID) techniques resolve problems in cell biology. *Pflugers Archiv : European*
1684 *journal of physiology* **465**, 409–417 (2013).

1685 84. W. Luo, Z. Z. Lieu, E. Manser, A. D. Bershadsky, M. P. Sheetz, Formin DAAM1 organizes actin
1686 filaments in the cytoplasmic nodal actin network. *PLoS ONE* **11**, 1–22 (2016).

1687 85. K. M. C. Chan, A. L. Arthur, J. Morstein, M. Jin, A. Bhat, D. Schlesinger, S. Son, D. A. Stevens,
1688 D. G. Drubin, D. A. Fletcher, Evolutionarily related small viral fusogens hijack distinct but
1689 modular actin nucleation pathways to drive cell-cell fusion. *Proc Natl Acad Sci USA* **118**,
1690 e2007526118 (2021).

1691 86. A. Drazic, H. Aksnes, M. Marie, M. Boczkowska, S. Varland, E. Timmerman, H. Foyn, N.
1692 Glomnes, G. Rebowski, F. Impens, K. Gevaert, R. Dominguez, T. Arnesen, NAA80 is actin's N-
1693 terminal acetyltransferase and regulates cytoskeleton assembly and cell motility.
1694 *Proceedings of the National Academy of Sciences* **115**, 4399–4404 (2018).

1695 87. J. Block, D. Breitsprecher, S. Kühn, M. Winterhoff, F. Kage, R. Geffers, P. Duwe, J. L. Rohn, B.
1696 Baum, C. Brakebusch, M. Geyer, T. E. B. Stradal, J. Faix, K. Rottner, FMNL2 Drives Actin-

1697 Based Protrusion and Migration Downstream of Cdc42. *Current Biology* **22**, 1005–1012
1698 (2012).

1699 88. A. Schirenbeck, R. Arasada, T. Bretschneider, M. Schleicher, J. Faix, Formins and VASPs may
1700 co-operate in the formation of filopodia. *Biochemical Society Transactions* **33**, 4 (2005).

1701 89. H. Mizuno, C. Higashida, Y. Yuan, T. Ishizaki, S. Narumiya, N. Watanabe, Rotational
1702 movement of the formin mDia1 along the double helical strand of an actin filament. *Science*
1703 **331**, 80–83 (2011).

1704 90. X. Naj, A. K. Hoffmann, M. Himmel, S. Linder, The formins FMNL1 and mDia1 regulate
1705 coiling phagocytosis of borrelia burgdorferi by primary human macrophages. *Infection and*
1706 *Immunity* **81**, 1683–1695 (2013).

1707 91. C. J. Gould, S. Maiti, A. Michelot, B. R. Graziano, L. Blanchoin, B. L. Goode, The formin DAD
1708 domain plays dual roles in autoinhibition and actin nucleation. *Current Biology* **21**, 384–390
1709 (2011).

1710 92. M. P. Murrell, R. Voituriez, J.-F. Joanny, P. Nassoy, C. Sykes, M. L. Gardel, Liposome
1711 adhesion generates traction stress. *Nature Phys* **10**, 163–169 (2014).

1712 93. A. Ward, F. Hilitski, W. Schwenger, D. Welch, A. W. C. Lau, V. Vitelli, L. Mahadevan, Z. Dogic,
1713 Solid friction between soft filaments. *Nature Mater* **14**, 583–588 (2015).

1714 94. M. A. Dichtl, E. Sackmann, Microrheometry of semiflexible actin networks through enforced
1715 single-filament reptation: Frictional coupling and heterogeneities in entangled networks.
1716 *Proc. Natl. Acad. Sci. U.S.A.* **99**, 6533–6538 (2002).

1717 95. F. Nedelec, D. Foethke, Collective Langevin dynamics of flexible cytoskeletal fibers. *New J.*
1718 *Phys.* **9**, 427–427 (2007).

1719 96. C. Zhu, C. T. Lee, P. Rangamani, Mem3DG: Modeling membrane mechanochemical
1720 dynamics in 3D using discrete differential geometry. *Biophysical Reports* **2**, 100062 (2022).

1721 97. S. Dmitrieff, A. Alsina, A. Mathur, F. J. Nédélec, Balance of microtubule stiffness and cortical
1722 tension determines the size of blood cells with marginal band across species. *Proc. Natl.*
1723 *Acad. Sci. U.S.A.* **114**, 4418–4423 (2017).

1724 98. Y. Shi, J. Zhang, M. Mullin, B. Dong, A. S. Alberts, K. A. Siminovitch, The mDial Formin Is
1725 Required for Neutrophil Polarization, Migration, and Activation of the LARG/RhoA/ROCK
1726 Signaling Axis during Chemotaxis. *The Journal of Immunology* **182**, 3837–3845 (2009).

1727 99. D. Sakata, H. Taniguchi, S. Yasuda, A. Adachi-Morishima, Y. Hamazaki, R. Nakayama, T. Miki,
1728 N. Minato, S. Narumiya, Impaired T lymphocyte trafficking in mice deficient in an actin-
1729 nucleating protein, mDia1. *Journal of Experimental Medicine* **204**, 2031–2038 (2007).

1730 100. C. Yang, L. Czech, S. Gerboth, S. Kojima, G. Scita, T. Svitkina, Novel Roles of Formin
1731 mDia2 in Lamellipodia and Filopodia Formation in Motile Cells. *PLoS Biol* **5**, e317 (2007).

1732 101. T. Isogai, R. van der Kammen, D. Leyton-Puig, K. M. Kedziora, K. Jalink, M. Innocenti,
1733 Initiation of lamellipodia and ruffles involves cooperation between mDia1 and the Arp2/3
1734 complex. *Journal of Cell Science*, jcs.176768 (2015).

1735 102. P. Monzo, Y. K. Chong, C. Guetta-Terrier, A. Krishnasamy, S. R. Sathe, E. K. F. Yim, W. H.
1736 Ng, B. T. Ang, C. Tang, B. Ladoux, N. C. Gauthier, M. P. Sheetz, Mechanical confinement
1737 triggers glioma linear migration dependent on formin FHOD3. *MBoC* **27**, 1246–1261 (2016).

1738 103. F. Kage, M. Winterhoff, V. Dimchev, J. Mueller, T. Thalheim, A. Freise, S. Brühmann, J.
1739 Kollasser, J. Block, G. Dimchev, M. Geyer, H.-J. Schnittler, C. Brakebusch, T. E. B. Stradal, M.-
1740 F. Carlier, M. Sixt, J. Käs, J. Faix, K. Rottner, FMNL formins boost lamellipodial force
1741 generation. *Nat Commun* **8**, 14832 (2017).

1742 104. Y. Yamazaki, Y. Miyata, K. Morigaki, M. Miyazaki, Controlling Physical and Biochemical
1743 Parameters of Actin Nucleation Using a Patterned Model Lipid Membrane. *Nano Lett.* **24**,
1744 1825–1834 (2024).

1745 105. M. Abercrombie, J. E. M. Heaysman, S. M. Pegrum, The locomotion of fibroblasts in
1746 culture I. Movements of the leading edge. *Experimental Cell Research* **59**, 393–398 (1970).

1747 106. P. Maiuri, E. Terriac, P. Paul-Gilloteaux, T. Vignaud, K. McNally, J. Onuffer, K. Thorn, P. A.
1748 Nguyen, N. Georgoulia, D. Soong, A. Jayo, N. Beil, J. Beneke, J. C. Hong Lim, C. Pei-Ying Sim,
1749 Y.-S. Chu, A. Jiménez-Dalmaroni, J.-F. Joanny, J.-P. Thiery, H. Erfle, M. Parsons, T. J.
1750 Mitchison, W. A. Lim, A.-M. Lennon-Duménil, M. Piel, M. Théry, The first World Cell Race.
1751 *Current Biology* **22**, R673–R675 (2012).

1752 107. S. A. Koestler, K. Rottner, F. Lai, J. Block, M. Vinzenz, J. V. Small, F- and G-Actin
1753 Concentrations in Lamellipodia of Moving Cells. *PLoS ONE* **4**, e4810 (2009).

1754 108. S. Samarin, S. Romero, C. Kocks, D. Didry, D. Pantaloni, M. F. Carlier, How VASP
1755 enhances actin-based motility. *Journal of Cell Biology* **163**, 131–142 (2003).

1756 109. W. M. Brieher, M. Coughlin, T. J. Mitchison, Fascin-mediated propulsion of Listeria
1757 monocytogenes independent of frequent nucleation by the Arp2/3 complex. *Journal of Cell*
1758 *Biology* **165**, 233–242 (2004).

1759 110. P. Li, S. Banjade, H. C. Cheng, S. Kim, B. Chen, L. Guo, M. Llaguno, J. V. Hollingsworth, D.
1760 S. King, S. F. Banani, P. S. Russo, Q. X. Jiang, B. T. Nixon, M. K. Rosen, Phase transitions in the
1761 assembly of multivalent signalling proteins. *Nature* **483**, 336–340 (2012).

1762 111. C. Simon, R. Kusters, V. Caorsi, A. Allard, M. Abou-Ghali, J. Manzi, A. Di Cicco, D. Lévy, M.
1763 Lenz, J.-F. Joanny, C. Campillo, J. Plastino, P. Sens, C. Sykes, Actin dynamics drive cell-like
1764 membrane deformation. *Nature Physics* **15**, 602–609 (2019).

1765 112. P. DiMilla, J. Stone, J. Quinn, S. Albelda, D. Lauffenburger, Maximal migration of human
1766 smooth muscle cells on fibronectin and type IV collagen occurs at an intermediate
1767 attachment strength. *Journal of Cell Biology* **122**, 729–737 (1993).

1768 113. C. Schreiber, B. Amiri, J. C. J. Heyn, J. O. Rädler, M. Falcke, On the adhesion–velocity
1769 relation and length adaptation of motile cells on stepped fibronectin lanes. *Proc. Natl. Acad.*
1770 *Sci. U.S.A.* **118**, e2009959118 (2021).

1771 114. V. Caorsi, J. Lemière, C. Campillo, M. Bussonnier, J. Manzi, T. Betz, J. Plastino, K.
1772 Carvalho, C. Sykes, Cell-sized liposome doublets reveal active tension build-up driven by
1773 acto-myosin dynamics. *Soft Matter* **12**, 6223–6231 (2016).

1774 115. W. I. Goh, K. B. Lim, T. Sudhaharan, K. P. Sem, W. Bu, A. M. Chou, S. Ahmed, mDia1 and
1775 WAVE2 Proteins Interact Directly with IRSp53 in Filopodia and Are Involved in Filopodium
1776 Formation. *Journal of Biological Chemistry* **287**, 4702–4714 (2012).

1777 116. A. Bisaria, A. Hayer, D. Garbett, D. Cohen, T. Meyer, Membrane-proximal F-actin
1778 restricts local membrane protrusions and directs cell migration. *Science* **368**, 1205–1210
1779 (2020).

1780 117. Z. Shi, Z. T. Graber, T. Baumgart, H. A. Stone, A. E. Cohen, Cell Membranes Resist Flow.
1781 *Cell* **175**, 1769-1779.e13 (2018).

1782 118. S. Gat, C. Simon, C. Campillo, A. Bernheim-Groswasser, C. Sykes, Finger-like membrane
1783 protrusions are favored by heterogeneities in the actin network. *Soft Matter* **16**, 7222–7230
1784 (2020).

1785 119. S. M. Bartelt, J. Steinkühler, R. Dimova, S. V. Wegner, Light-Guided Motility of a Minimal
1786 Synthetic Cell. *Nano Lett.* **18**, 7268–7274 (2018).

1787 120. L. A. Banaszynski, C. W. Liu, T. J. Wandless, Characterization of the FKBP·Rapamycin·FRB
1788 Ternary Complex. *J. Am. Chem. Soc.* **127**, 4715–4721 (2005).

1789 121. E. Rihtar, T. Lebar, D. Lainšček, K. Kores, S. Lešnik, U. Bren, R. Jerala, Chemically inducible
1790 split protein regulators for mammalian cells. *Nat Chem Biol*, doi: 10.1038/s41589-022-
1791 01136-x (2022).

1792 122. K. Yoshida, K. Abe, Y. Sato, I. Kawamata, R. J. Archer, H. T. Matsubayashi, S. Hamada, S.
1793 Murata, S. Nomura, Transmembrane DNA Sequence Signaling via Hybridization. ChemRxiv
1794 [Preprint] (2024). https://doi.org/10.26434/chemrxiv-2024-571kp.

1795 123. S. L. Veatch, S. L. Keller, Separation of Liquid Phases in Giant Vesicles of Ternary
1796 Mixtures of Phospholipids and Cholesterol. *Biophysical Journal* **85**, 3074–3083 (2003).

124. T. Litschel, B. Ramm, R. Maas, M. Heymann, P. Schwille, Beating Vesicles: Encapsulated Protein Oscillations Cause Dynamic Membrane Deformations. *Angewandte Chemie International Edition* **57**, 16286–16290 (2018).

125. S. Takada, N. Yoshinaga, N. Doi, K. Fujiwara, Controlling the Periodicity of a Reaction–Diffusion Wave in Artificial Cells by a Two-Way Energy Supplier. *ACS Nano* **16**, 16853–16861 (2022).

126. S. D. Hansen, W. Y. C. Huang, Y. K. Lee, P. Bieling, S. M. Christensen, J. T. Groves, Stochastic geometry sensing and polarization in a lipid kinase–phosphatase competitive reaction. *Proceedings of the National Academy of Sciences of the United States of America* **116**, 15013–15022 (2019).

127. Y. Sato, M. Takinoue, Capsule-like DNA Hydrogels with Patterns Formed by Lateral Phase Separation of DNA Nanostructures. *JACS Au* **2**, 159–168 (2022).

128. R. Sakamoto, Z. Izri, Y. Shimamoto, M. Miyazaki, Y. T. Maeda, Geometric trade-off between contractile force and viscous drag determines the actomyosin-based motility of a cell-sized droplet. *Proc. Natl. Acad. Sci. U.S.A.* **119**, e2121147119 (2022).

129. L. T. Benk, A. S. Benk, R. B. Lira, E. A. Cavalcanti-Adam, R. Dimova, R. Lipowsky, B. Geiger, J. P. Spatz, Integrin α_{IIb} β_3 Activation and Clustering in Minimal Synthetic Cells. *Advanced NanoBiomed Research* **2**, 2100094 (2022).

130. S. Brühmann, D. S. Ushakov, M. Winterhoff, R. B. Dickinson, U. Curth, J. Faix, Distinct VASP tetramers synergize in the processive elongation of individual actin filaments from clustered arrays. *Proc Natl Acad Sci USA* **114**, E5815–E5824 (2017).

131. Y. Liang, Y. Takaki, H. Inaba, K. Matsuura, Local Deformation in Phase-Separated Giant Liposomes via Photo-Induced Peptide Nanofiber Formation. *Langmuir* **41**, 15173–15181 (2025).

132. J. E. Tropea, S. Cherry, D. S. Waugh, "Expression and Purification of Soluble His6-Tagged TEV Protease" in *High Throughput Protein Expression and Purification: Methods and Protocols*, S. A. Doyle, Ed. (Humana Press, Totowa, NJ, 2009; https://doi.org/10.1007/978-1-59745-196-3_19)*Methods in Molecular Biology*, pp. 297–307.

133. T. Inoue, W. D. Heo, J. S. Grimley, T. J. Wandless, T. Meyer, An inducible translocation strategy to rapidly activate and inhibit small GTPase signaling pathways. *Nature Methods* **2**, 415–418 (2005).

134. Cytoplasmic Actin: Purification and Single Molecule Assembly Assays | SpringerLink. https://link.springer.com/protocol/10.1007/978-1-62703-538-5_9.

135. L. K. Doolittle, M. K. Rosen, S. B. Padrick, Measurement and analysis of in vitro actin polymerization. *Methods in Molecular Biology*, doi: 10.1007/978-1-62703-538-5_16 (2013).

136. S. Razavi, T. Inoue, T. LUO, D. Robinson, Methods for making giant vesicles and their use (2024). https://patents.google.com/patent/US11951210B2/en.

137. J. Schindelin, I. Arganda-Carreras, E. Frise, V. Kaynig, M. Longair, T. Pietzsch, S. Preibisch, C. Rueden, S. Saalfeld, B. Schmid, J.-Y. Tinevez, D. J. White, V. Hartenstein, K. Eliceiri, P. Tomancak, A. Cardona, Fiji: an open-source platform for biological-image analysis. *Nature methods* **9**, 676–682 (2012).

138. H. T. Matsubayashi, J. Mountain, N. Takahashi, A. Deb Roy, T. Yao, A. F. Peterson, C. Saez Gonzalez, I. Kawamata, T. Inoue, Non-catalytic role of phosphoinositide 3-kinase in mesenchymal cell migration through non-canonical induction of p85β/AP2-mediated endocytosis. *Nat Commun* **15**, 2612 (2024).

139. K. Crane, DISCRETE DIFFERENTIAL GEOMETRY: AN APPLIED INTRODUCTION.

140. M. Meyer, M. Desbrun, P. Schröder, A. H. Barr, "Discrete Differential-Geometry Operators for Triangulated 2-Manifolds" in *Visualization and Mathematics III*, H.-C. Hege, K. Polthier, Eds. (Springer, Berlin, Heidelberg, 2003), pp. 35–57.

141. C. C. Beltzner, T. D. Pollard, Pathway of Actin Filament Branch Formation by Arp2/3 Complex*. *Journal of Biological Chemistry* **283**, 7135–7144 (2008).

142. W. Rawicz, K. C. Olbrich, T. McIntosh, D. Needham, E. Evans, Effect of Chain Length and Unsaturation on Elasticity of Lipid Bilayers. *Biophysical Journal* **79**, 328–339 (2000).

143. M. J. Footer, J. W. J. Kerssemakers, J. A. Theriot, M. Dogterom, Direct measurement of force generation by actin filament polymerization using an optical trap. *Proc. Natl. Acad. Sci. U.S.A.* **104**, 2181–2186 (2007).

144. D. R. Kovar, T. D. Pollard, Insertional assembly of actin filament barbed ends in association with formins produces piconewton forces. *Proc. Natl. Acad. Sci. U.S.A.* **101**, 14725–14730 (2004).

145. D. Drabik, M. Gavutis, R. Valiokas, A. Ulčinas, Determination of the Mechanical Properties of Model Lipid Bilayers Using Atomic Force Microscopy Indentation. *Langmuir* **36**, 13251–13262 (2020).

146. O. H. Akenuwa, S. M. Abel, Organization and dynamics of cross-linked actin filaments in confined environments. *Biophysical Journal* **122**, 30–42 (2023).

147. San Diego Supercomputer Center (2022): Triton Shared Computing Cluster. University of California, San Diego. Service. https://doi.org/10.57873/T34W2R

148. L. A. Gross, G. S. Baird, R. C. Hoffman, K. K. Baldridge, R. Y. Tsien, The structure of the chromophore within DsRed, a red fluorescent protein from coral. *Proc Natl Acad Sci U S A* **97**, 11990–11995 (2000).

1866 149. V. I. Martynov, A. P. Savitsky, N. Y. Martynova, P. A. Savitsky, K. A. Lukyanov, S. A.
1867 Lukyanov, Alternative Cyclization in GFP-like Proteins Family. *Journal of Biological Chemistry*
1868 **276**, 21012–21016 (2001).

1869

Figure 1

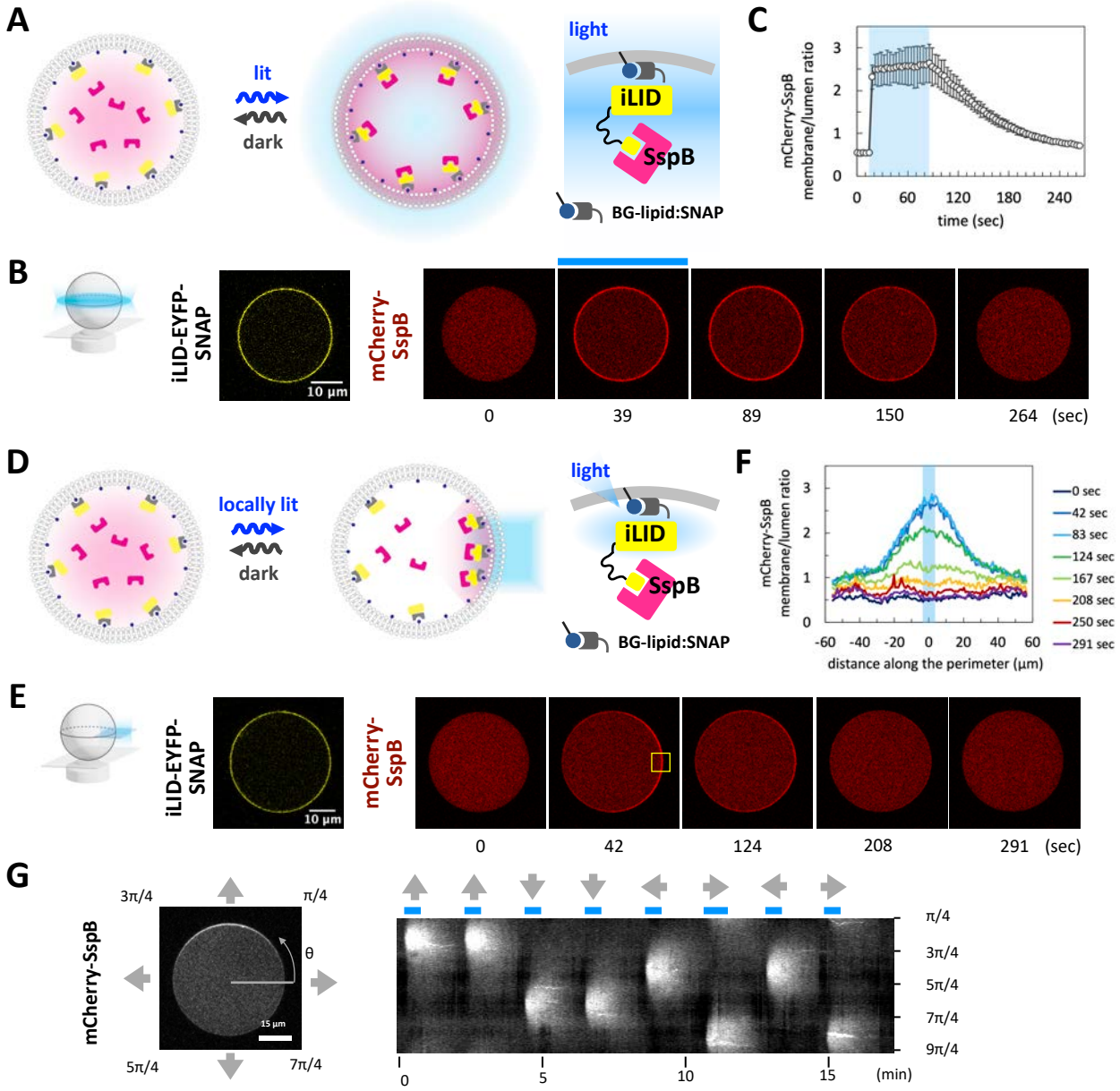

Fig. 1. Reversible and asymmetric control of protein localization with iLID-SspB within GUVs. (A) Schematic representation of iLID-SspB reaction with global light stimulation. iLID was tethered on the membrane via the interaction between SNAP-tag and bendylguanine-conjugated lipids. Upon blue light illumination, Jα helix of iLID extends to expose the binding site for SspB, whereas in the dark, iLID reverses to its closed state and releases SspB. (B) Representative images of iLID-YFP-SNAP and mCherry-SspB. Scale bar, 10 µm. Blue bar indicates the period of blue light illumination. (C) Time course of membrane/lumen ratio of mCherry-SspB signal (n=5). Error bars indicate 95% CI. Blue area indicates the period of blue light stimulation. (D) Schematic representation of iLID-SspB reaction with local light stimulation. (E) Representative images of mCherry-SspB. Scale bar, 10 µm. Yellow box indicates the area of blue light illumination. (F) Membrane/lumen ratio of mCherry-SspB for the representative image shown. The distance is measured from the center of blue light illumination along the perimeter of the GUV. (G) Representative image and kymograph of repetitive and reversible SspB translocation. Kymograph shows membrane signal of mCherry-SspB.

Figure 2

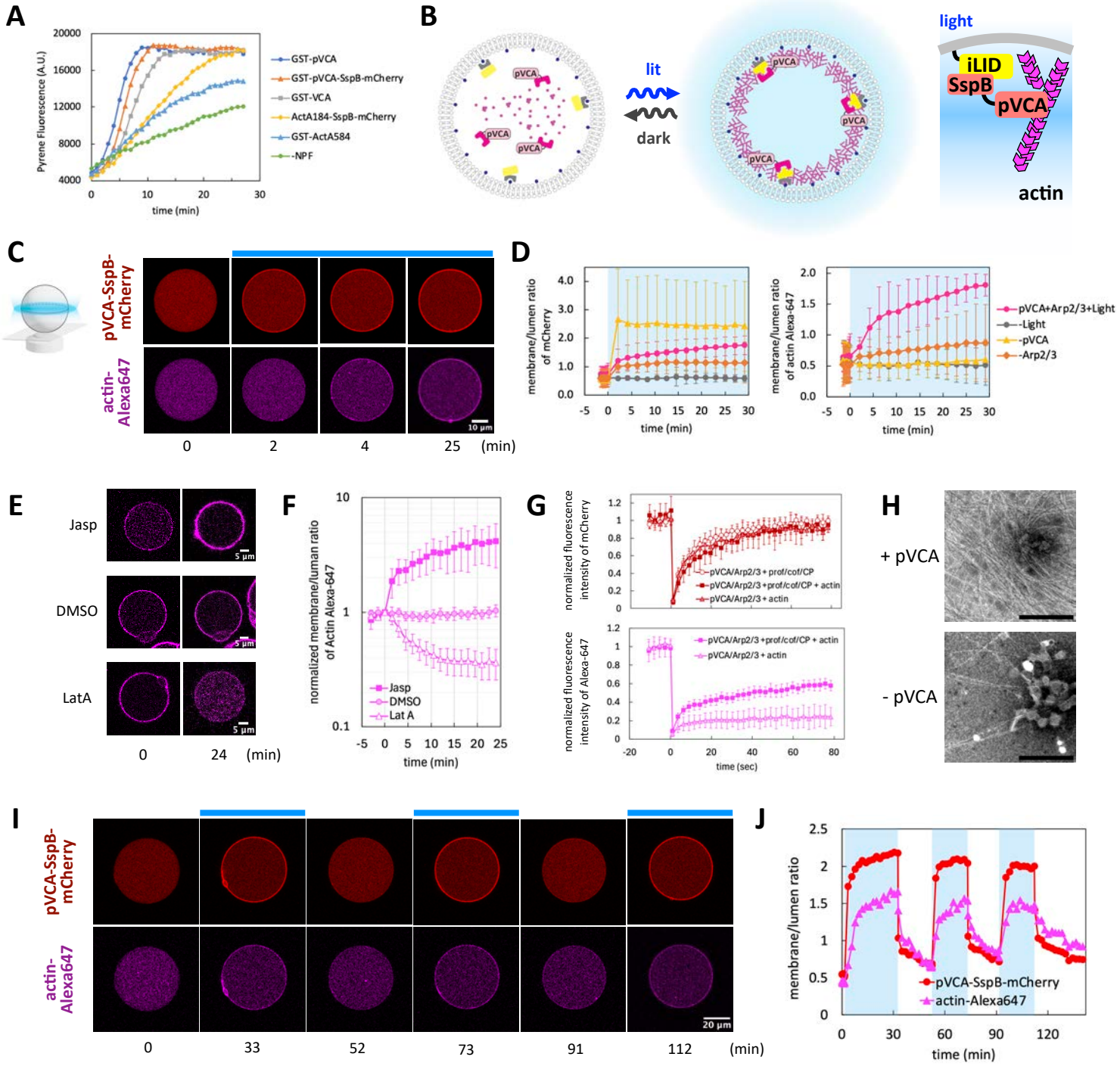

Fig. 2. Reversible light control of actin cytoskeleton within GUVs. (A) Bulk pyrene actin polymerization assay with 1 µM actin (5% pyrene-labeled), 10 nM Arp2/3, and 100 nM NPFs. (-NPF) represents actin and Arp2/3 only condition. (B) Schematic representation of light-inducible actin polymerization. Translocation of pVCA-SspB-mCherry increases local concentration of pVCA on the membrane and enhances actin polymerization. (C) Representative images of pVCA-SspB-mCherry and Alexa 647 actin. Blue bar indicates the period of blue light illumination. (D) Time course of membrane/lumen ratio of mCherry and Alexa 647 actin in (C) and fig. S9. pVCA +Arp2/3+Light: full set of components (n=4). -Light: no blue light stimulation (n=3). -pVCA: pVCA-SspB-mCherry was replaced with mCherry-SspB (n=4). -Arp2/3: Arp2/3 was omitted (n=4). In (E)–(H), pVCA-SspB-mCherry was constitutively anchored to the membrane via SsrA-SNAP. (E) Pharmacological perturbation of membrane-associated actin. DMSO (n=8), Jasplakinolide (Jasp, n=10), Latrunculin A (LatA, n=9). (F) Time course of normalized membrane/lumen ratio of Alexa-647 actin in (E). The values were normalized by time=0. (G) FRAP analysis of membrane fluorescence of mCherry and Alexa 647 actin in fig. S11. The values were normalized by time=0. Sample sizes are listed in fig. S11A. (H) Electron microscopy (EM) images of actin filaments in the presence and absence of pVCA. Scale bar indicates 500 nm. (I) Representative images of reversible actin polymerization. Blue bars indicate the period of blue light illumination. (J) Time course of membrane/lumen ratio of pVCA-SspB-mCherry and Alexa 647-labeled actin in (F). (D, F, G) Error bars indicate 95% CI.

Figure 3

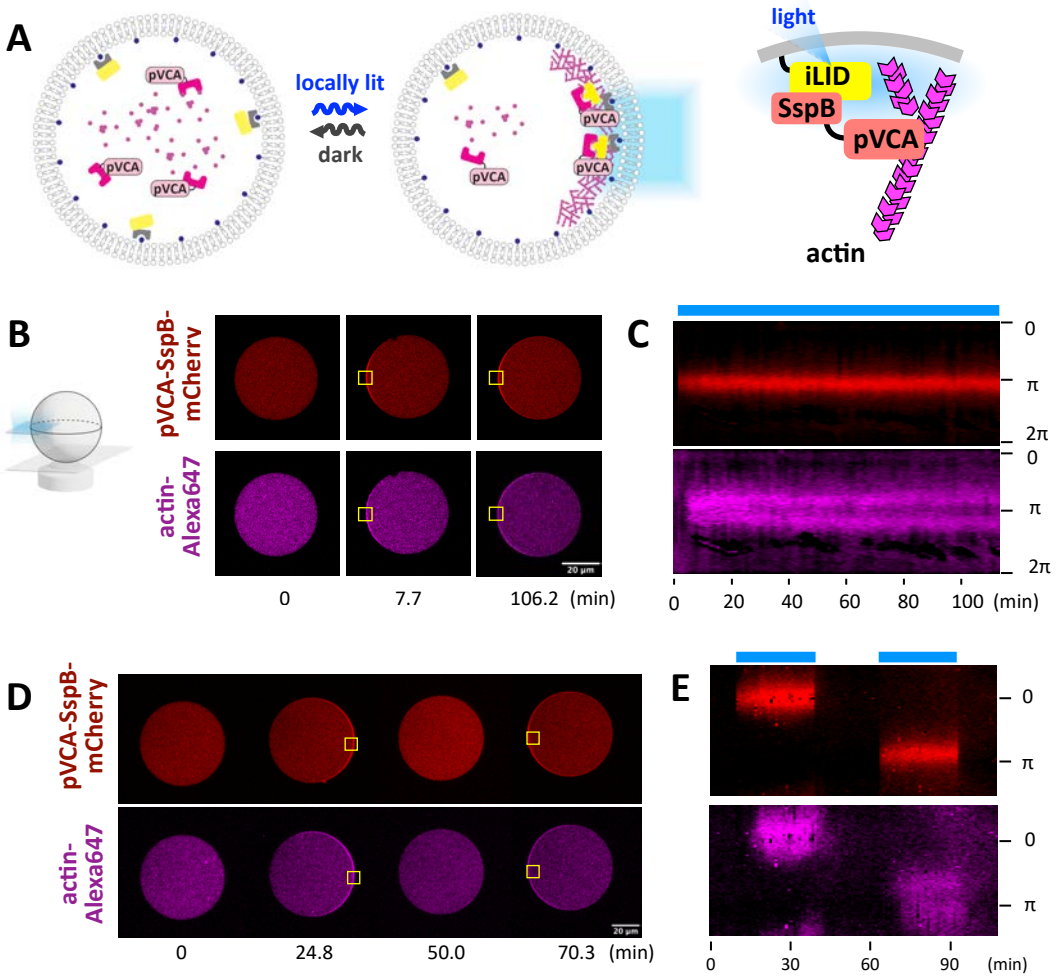

Fig. 3. Asymmetric light control of actin cytoskeleton within GUVs. (A) Schematic representation of iLID-SspB reaction with local light stimulation. (B, D) Representative images of light-inducible asymmetric actin polymerization. Yellow boxes indicate the area of blue light illumination. (C, E) Kymograph of membrane pVCA-SspB and actin signals. Blue bars indicate the period of blue light illumination. Triangles indicate timepoints represented in (B, D).

Figure 4

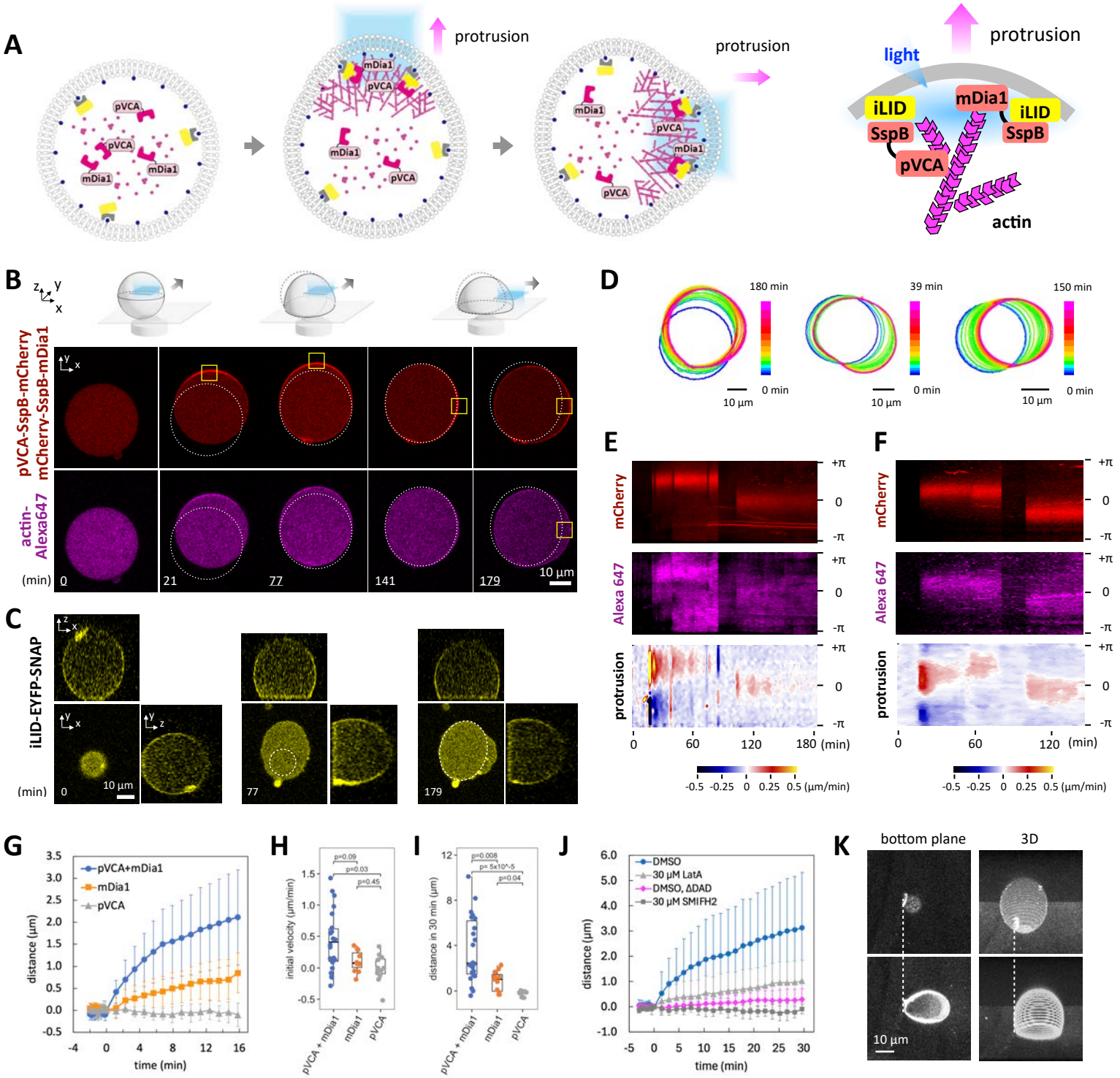

Fig. 4. mDia1-mediated actin polymerization drives protrusive movement of GUVs. (A) Schematic representation of light-inducible membrane protrusion driven by pVCA and mDia1-mediated actin polymerization. (B) Representative images of pVCA-mDia1-mediated movement of GUVs. Yellow boxes indicate the area of blue light stimulation. Dotted line shows the initial position of the GUV. (C) Representative images of iLID-EYFP-SNAP showing the increase in adhesive area and vesicle deformation into dome-like shape. X-y images show the confocal plane right above the bottom substrate. Z-x and y-z images are reconstituted from z-stack. Dotted line shows the adhesive area of the previous images. (D) Color-coded boundaries of GUVs. The data correspond as follows. Left: Fig. 4B. Middle: fig. S16A. Right: fig. S16B. (E, F) Kymographs of membrane signal of mCherry and actin Alexa-647 and membrane protrusions. Triangles in (E) indicate the timepoints represented in (B, C). Data of (E) and (F) correspond to Fig. 4 (B) and fig. S16A, respectively. (G) Distance the front (illuminated) side of GUV membrane moved forward. pVCA+mDia1 (1 µM GST-pVCA-SspB-mCherry + 1 µM mCherry-SspB-mDia1, n=14 vesicles), mDia1 (1 µM mCherry-SspB-mDia1, n=12 vesicles), pVCA (1 µM GST-pVCA-SspB-mCherry, n=12 vesicles). Error bars indicate 95% CI. (H, I) Quantification of the initial velocity and the distance the front side of GUV membrane moved forward. P values of Steel-Dwass test (two sided) are indicated. pVCA + mDia1: n=22 vesicles. mDia1: n=11 vesicles. pVCA: n=12 vesicles. Box whisker plots represent median, 1st, 3rd quartiles and 1.5×inter-quartile range. (J) Distance the front (illuminated) side of GUV membrane moved forward. DMSO (n=9 vesicles), 30 µM LatA (Latrunculin A) (n=10 vesicles). DMSO, ΔDAD: mCherry-SspB-mDia1 (FH1-FH2-DAD) was replaced with mCherry-SspB-mDia1(FH1-FH2) (n=13 vesicles). 30 µM SMIFH2 (n=6 vesicles). Error bars indicate 95% CI. (H, I) Quantification of the initial velocity and the distance the front side of GUV membrane moved forward. P values of Steel-Dwass test (two sided) are indicated. pVCA + mDia1: n=22 vesicles. mDia1: n=11 vesicles. pVCA: n=12 vesicles. Box whisker plots represent median, 1st, 3rd quartiles and 1.5×inter-quartile range. (K) A GUV deformed into dome-like shape after movement. Upper images: before light stimulation. Lower images: after light stimulation. The data corresponds to fig. S16C.

Figure S1

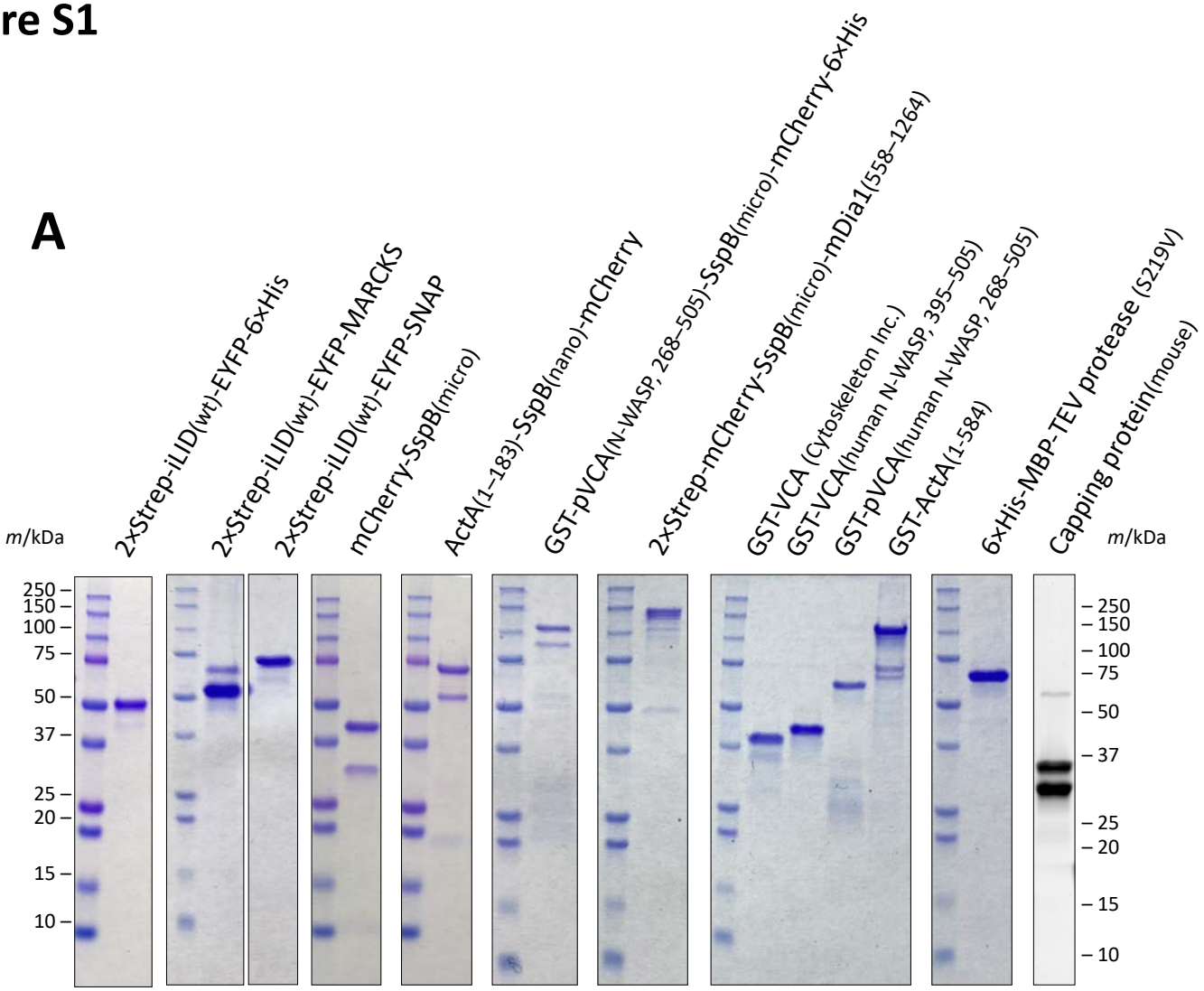

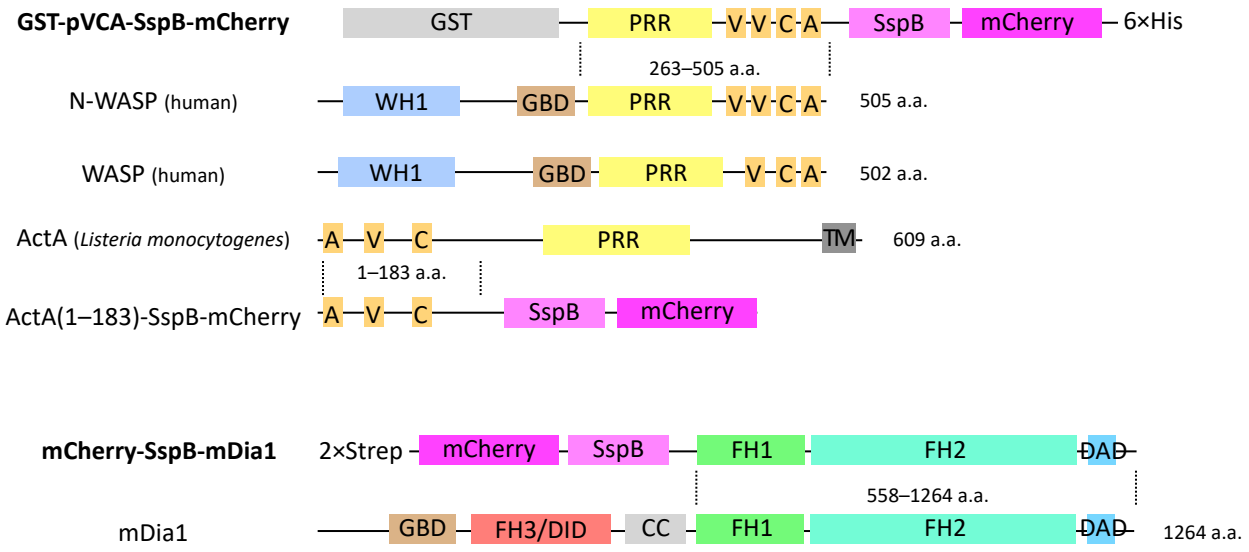

Fig. S1. Proteins purified in this study. (A) SDS-PAGE results of purified proteins. Blue: Coomassie brilliant blue staining. Gray: SYPRO Ruby staining. Most mCherry-tagged proteins show two extra bands due to a known chromophore cleavage reaction during the boiling process (145, 146). (B) Domain structures of NPFs used in this study.

Figure S2

A

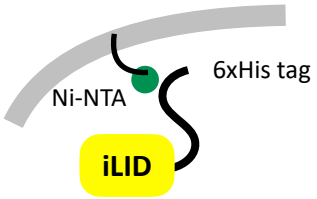

B

5 mol% NI-NTA-DGS/0–2 mol% PEG2000-PE/
93-95 mol% POPC

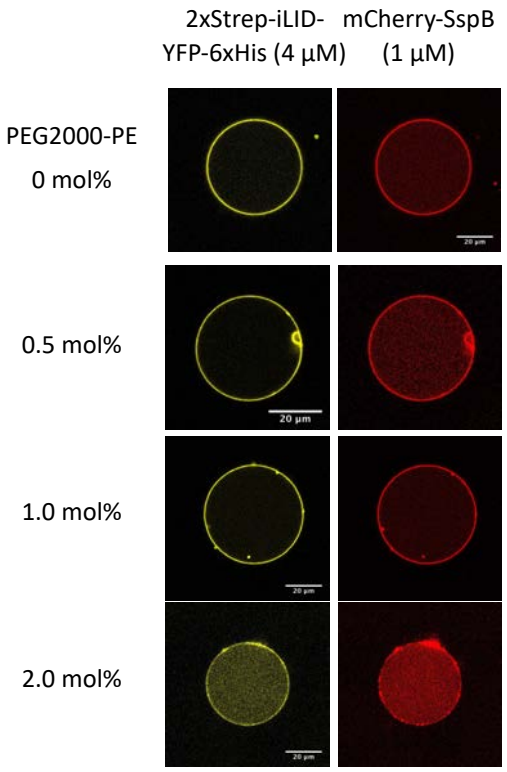

C

5 mol% Ni-NTA-DGS/95 mol% POPC

mCherry-SspB (1 µM)

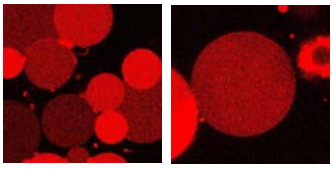

D

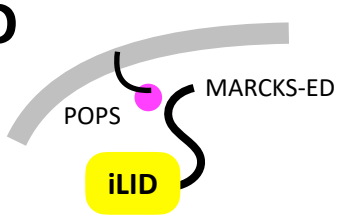

E

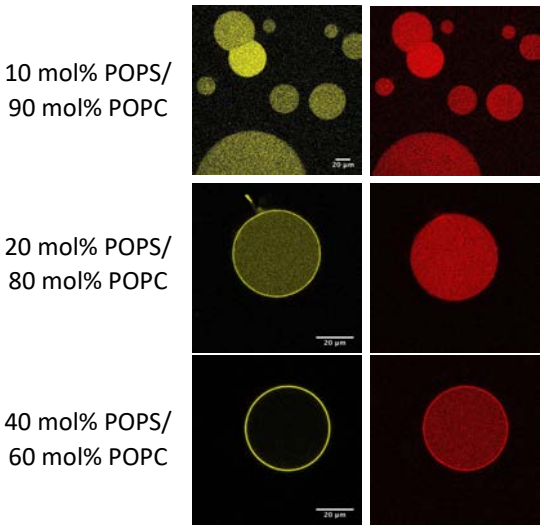

F

40 mol% POPS/58–60 mol% POPC

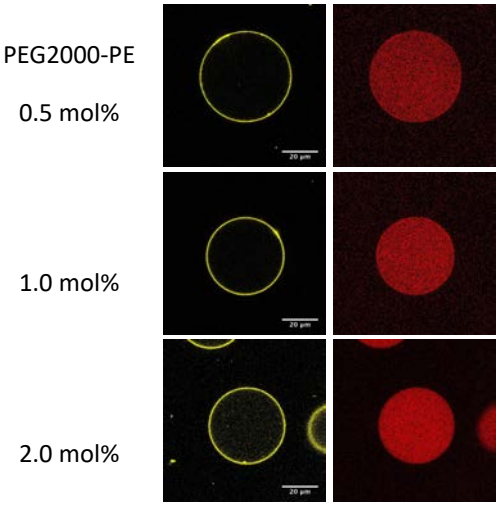

Figure S2

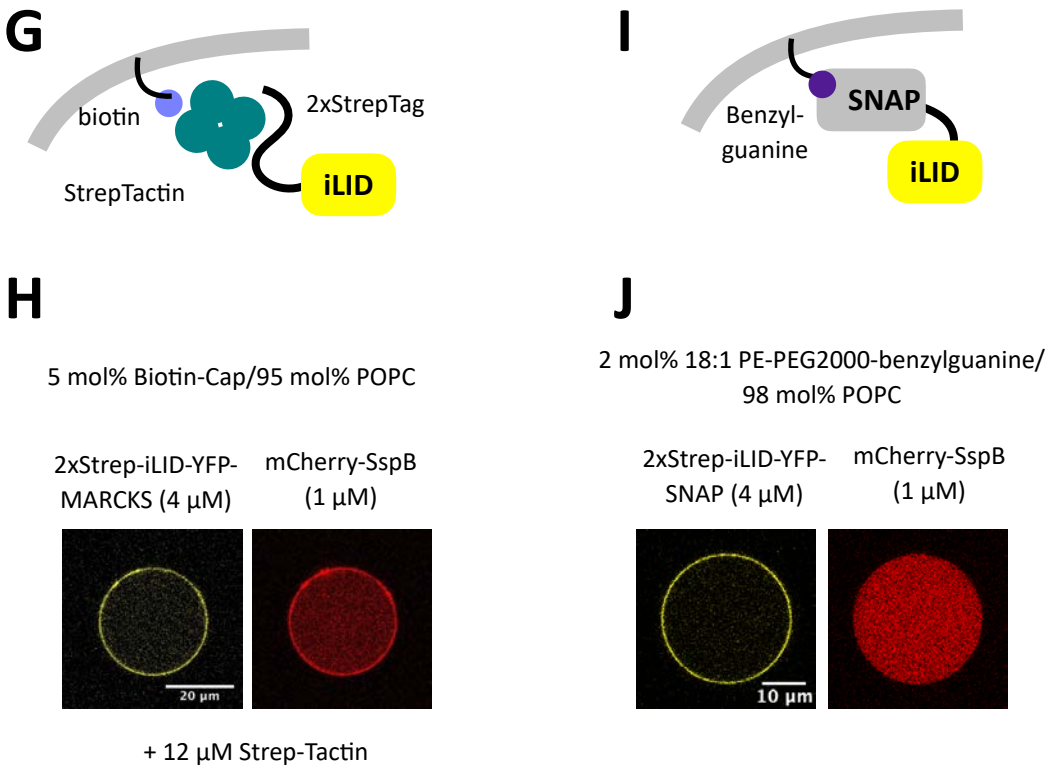

Fig. S2. Optimization of membrane anchoring of iLID. (A),(D),(G),(I): Schematic representations of membrane anchoring of iLID. (B),(C),(E),(F),(H),(J): Confocal images of iLID variants and mCherry-SspB. (B) His-tag Ni-NTA pair caused non-specific membrane recruitment of SspB. This is possibly caused by the presence of 2×Strep-iLID-YFP-6×His because mCherry-SspB itself did not show non-specific binding to the membrane of 5%Ni-NTA DGS/95%POPC (C). (E),(F) MARCKS-ED peptide requires high percentage of PS and PEGylated-lipids to reduce non-specific binding of SspB. (H) Biotin-StrepTactin-Streptag also caused non-specific membrane binding of SspB. (J) The data correspond with Fig. 1B.

Figure S3

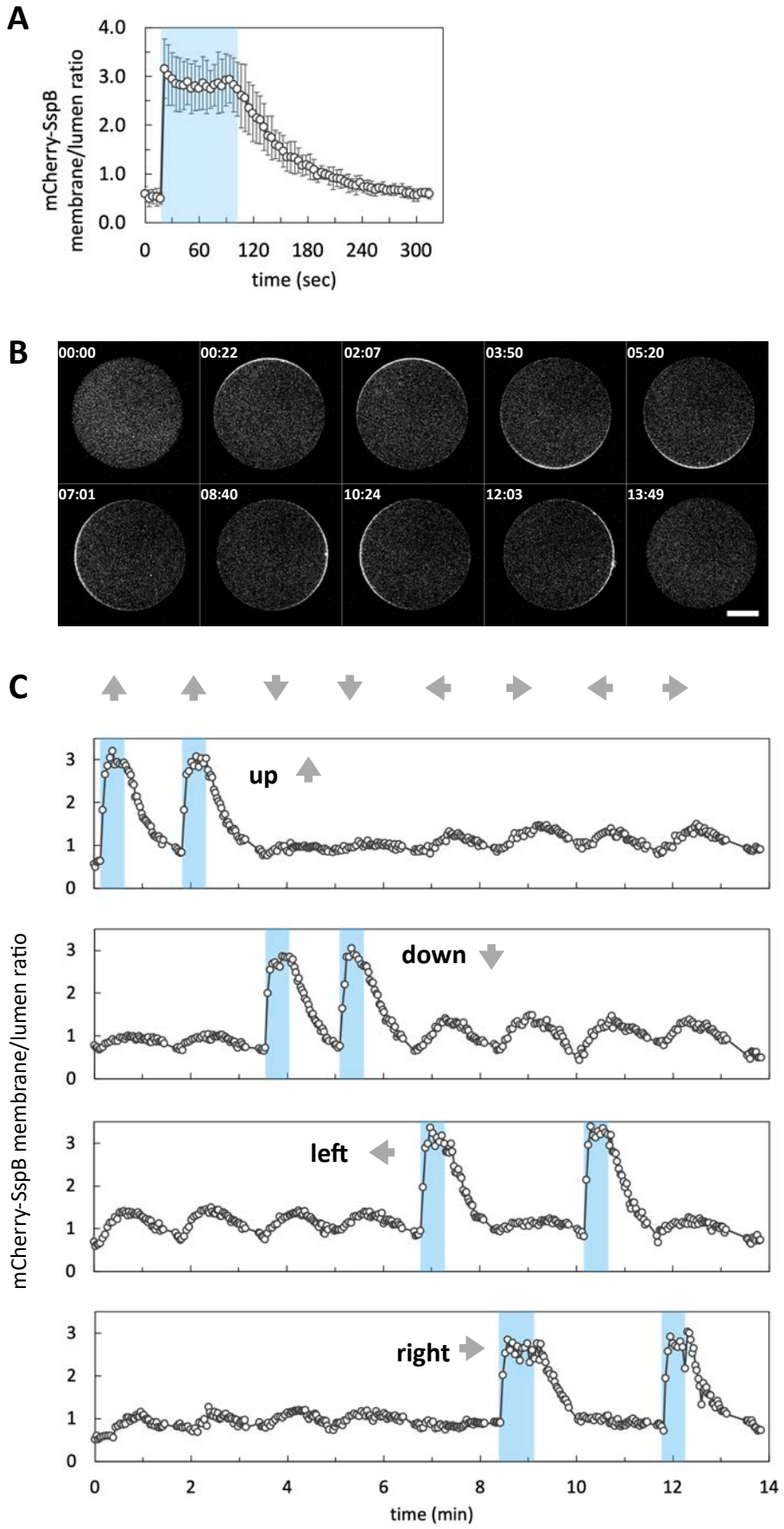

Fig. S3. Asymmetric control of protein localization with iLID-SspB within GUVs. (A) Time course of membrane/lumen ratio of mCherry-SspB signal in the illuminated area (n=6). Error bars indicate 95% CI. Blue area indicates the time window of blue light stimulation. The data corresponds to Fig. 1E and F. (B, C) Confocal images and time course of membrane/lumen ratio of mCherry-SspB signal responding to repetitive local light illuminations. The data corresponds to Fig. 1G.

Figure S4

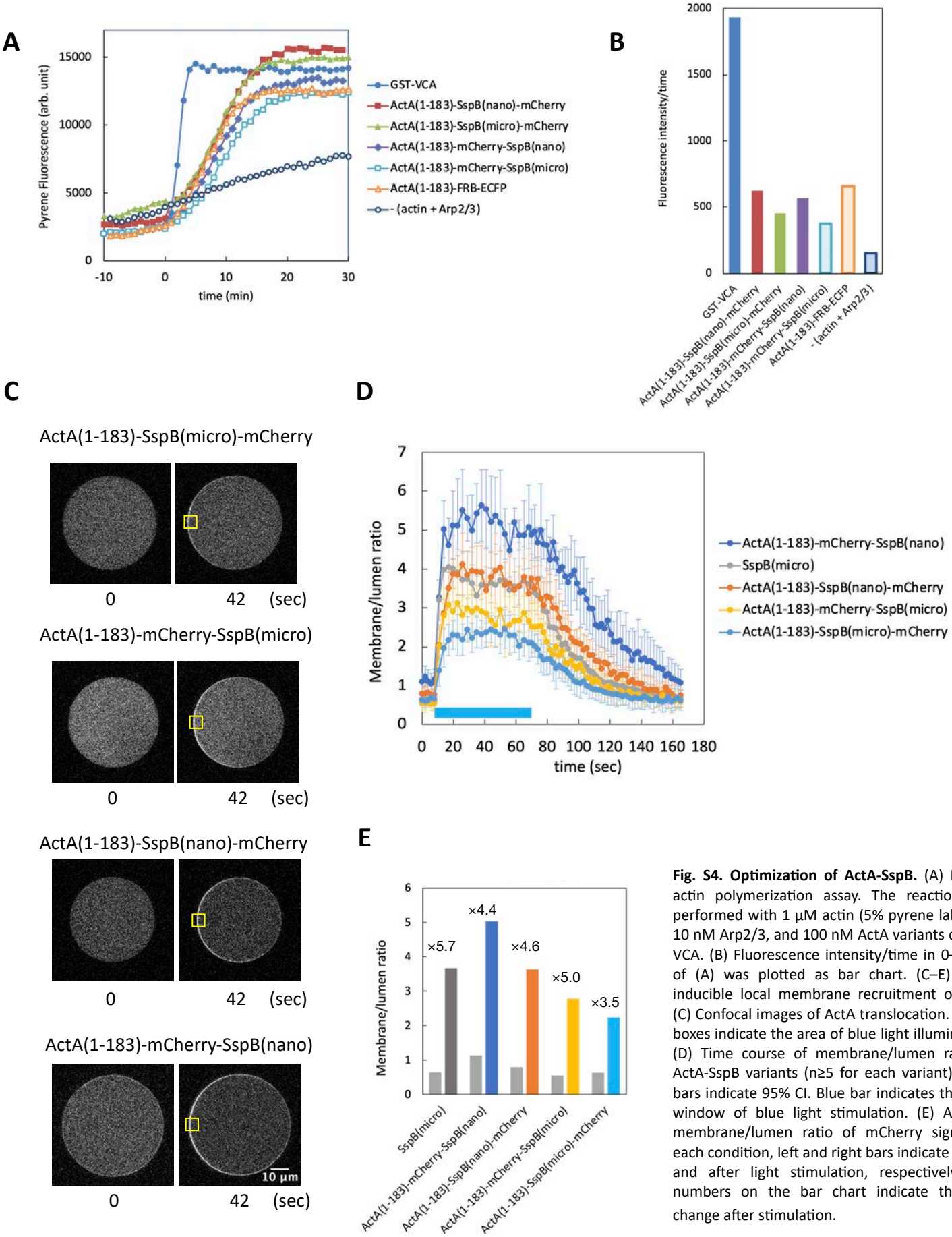

Fig. S4. Optimization of ActA-SspB. (A) Pyrene actin polymerization assay. The reaction was performed with 1 μM actin (5% pyrene labeled), 10 nM Arp2/3, and 100 nM ActA variants or GST-VCA. (B) Fluorescence intensity/time in 0–6 min of (A) was plotted as bar chart. (C–E) Light-inducible local membrane recruitment of ActA (C) Confocal images of ActA translocation. Yellow boxes indicate the area of blue light illumination. (D) Time course of membrane/lumen ratio of ActA-SspB variants (n≥5 for each variant). Error bars indicate 95% CI. Blue bar indicates the time window of blue light stimulation. (E) Average membrane/lumen ratio of mCherry signal. In each condition, left and right bars indicate before and after light stimulation, respectively. The numbers on the bar chart indicate the fold change after stimulation.

Figure S5

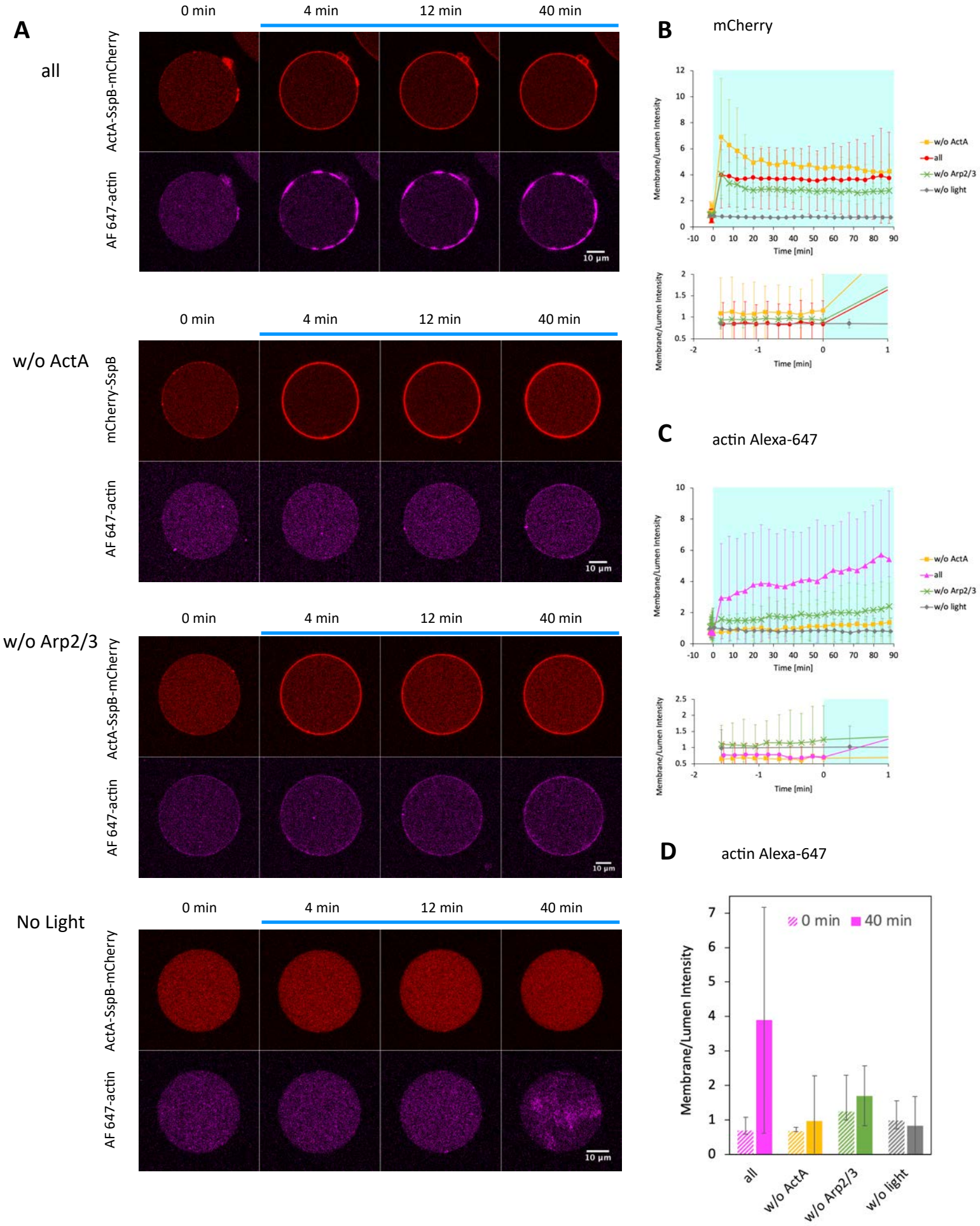
A
all
0 min
4 min
12 min
40 min
ActA-SspB-mCherry
AF 647-actin
10 µm
w/o ActA
mCherry-SspB
w/o Arp2/3
No Light
B
mCherry
Membrane/Lumen Intensity
Time [min]
w/o ActA
all
w/o Arp2/3
w/o light
C
actin Alexa-647
D
actin Alexa-647
0 min
40 min
all
w/o ActA
w/o Arp2/3
w/o light

Figure S5

Fig S5. Light-inducible actin polymerization with global ActA membrane recruitment. iLID-EYFP-MARCKS (5 µM), ActA-SspBnano-mCherry (2 µM), actin (1.5 µM, 10% Alexa-647 labeled), and Arp2/3 (150 nM) were encapsulated in GUVs containing 60 mol% POPC/40 mol% POPS. Blue light was applied to the entire GUV. (A) Representative images of ActA(1–183)-SspB(nano)-mCherry and actin Alexa-647. All components (n=4): w/o ActA: ActA(1–183)-SspB(nano)-mCherry was replaced with mCherry-SspB(micro) (n=3), w/o Arp2/3: Arp2/3 was omitted (n=3). No Light: no blue light stimulation (n=3). (B, C) Time course of membrane/lumen ratio of mCherry and actin Alexa 647. (D) Bar chart of membrane/lumen ratio of actin Alexa 647 before (0 min) and after (40 min) light stimulation. Error bars indicate 95% CI.

Figure S6

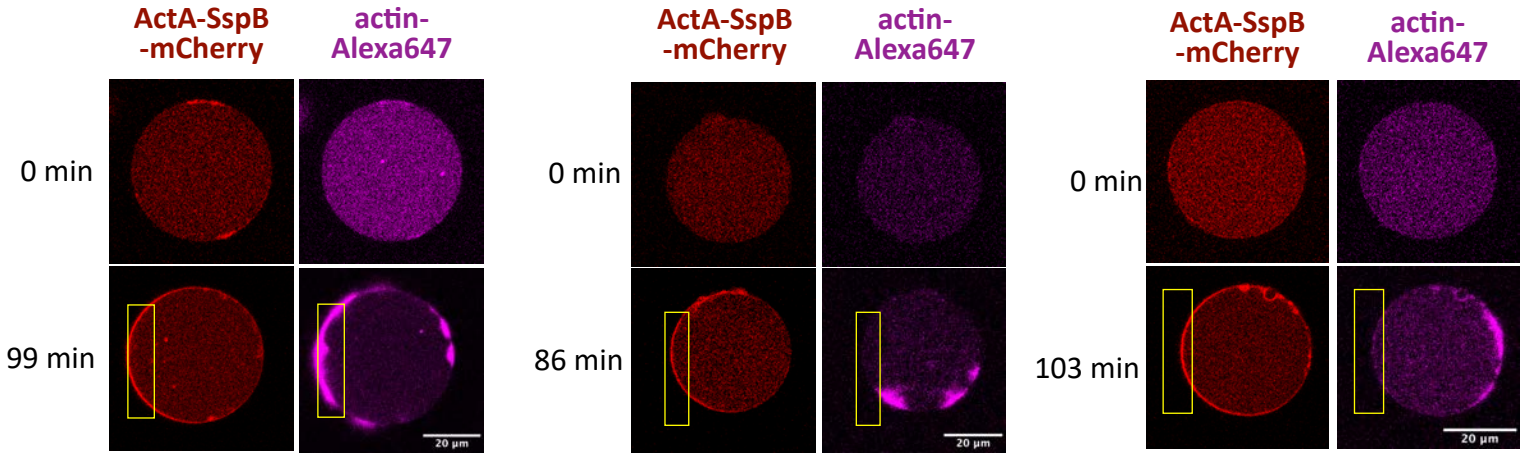

Fig S6. Asymmetric ActA membrane recruitment fails to induce directed actin polarization toward local light illumination. iLID-EYFP-MARCKS (5 µM), ActA-SspBnano-mCherry (2 µM), actin (1.5 µM, 10% Alexa-647 labeled), and Arp2/3 (150 nM), 1 mM ATP were encapsulated in GUVs containing 60 mol% POPC/40 mol% POPS. Yellow boxes indicate the area of blue light illumination. Although ActA creates asymmetric distribution, actin patches randomly distributed due to the diffusion on the membrane.

Figure S7

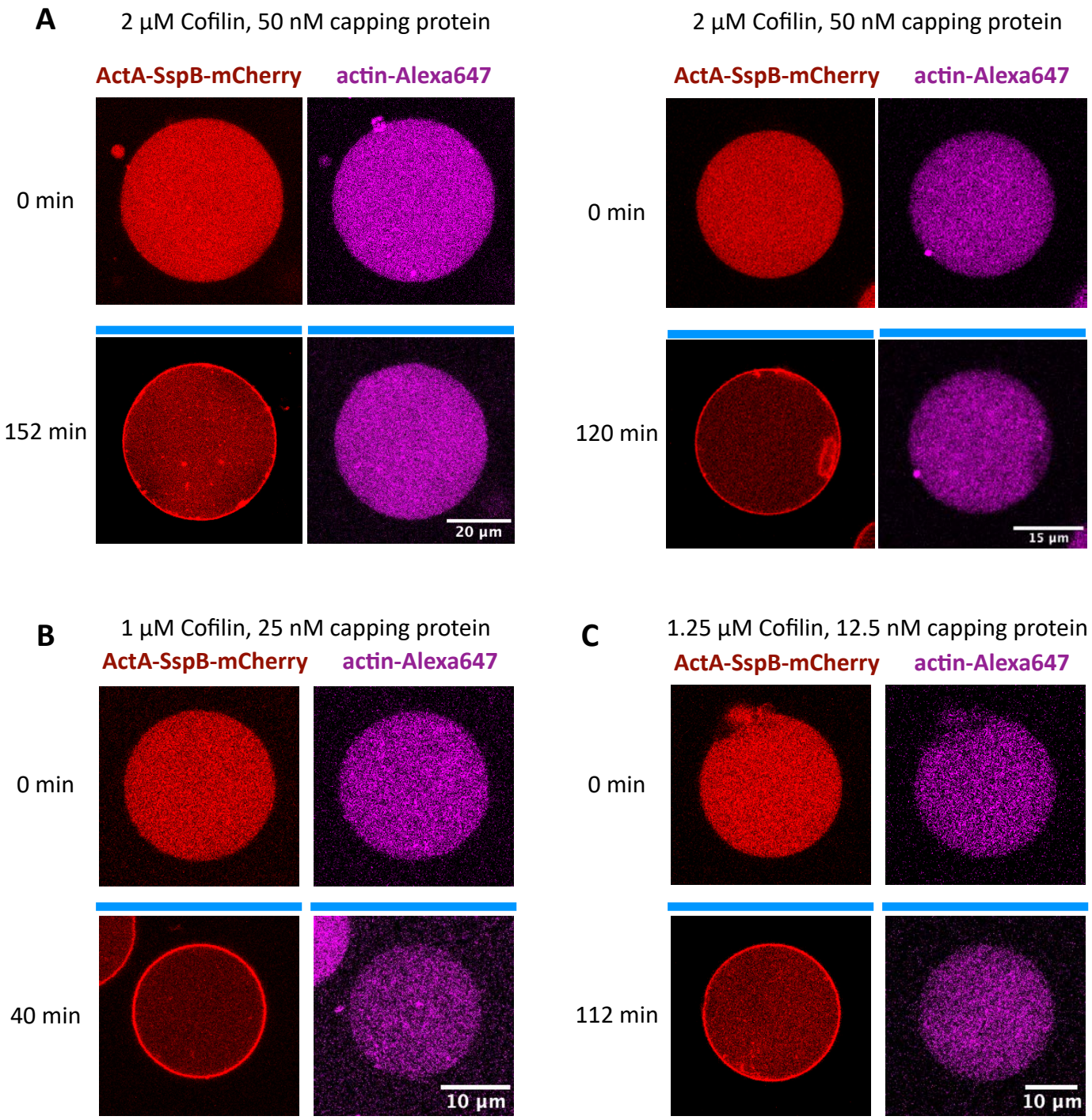

Fig. S7. Global ActA membrane recruitment fails to induce actin polymerization on the membrane in the presence of profilin, cofilin, and capping protein. 15 µM iLID-YFP-MARCKS, 5 µM ActA(1-183)-SspB(nano)-mCherry, 7.5 µM actin (10% Alexa 647 labeled), 150 nM Arp2/3, 3 µM profilin, cofilin, and capping protein were encapsulated in GUVs containing 60 mol% POPC/40 mol% POPS. Blue bars indicate the period of blue light illumination.

Figure S8

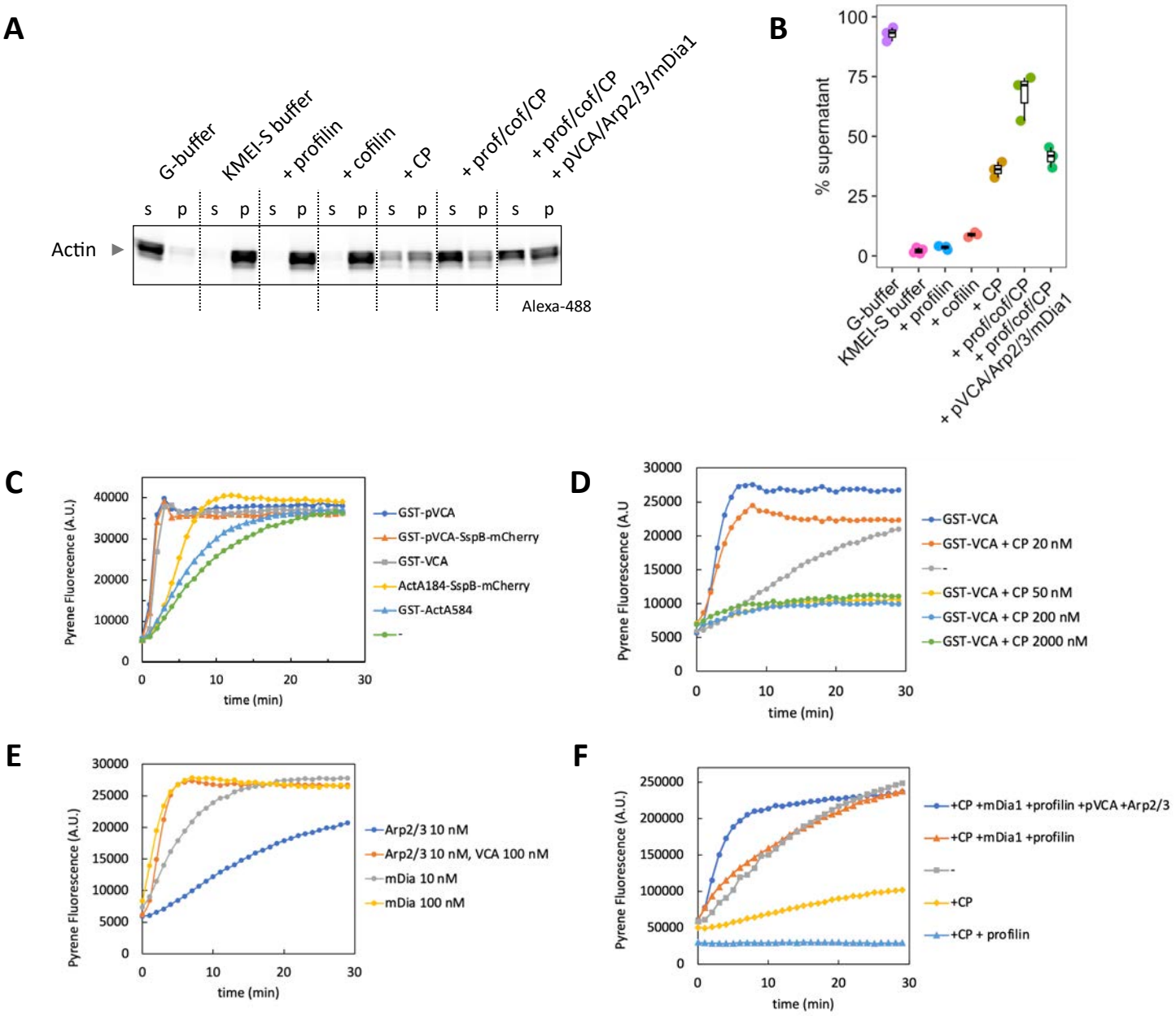

fig. S8. Biochemical characterization of actin and actin-binding proteins used in this study. (A, B) Ultracentrifuge assay. After 30 min actin polymerization reaction at RT, the solutions were ultracentrifuged 100,000×g, 60 min, at RT. Proteins and concentrations used: 7.5 µM actin (10% Alexa-488 labeled), 3 µM profilin, 4 µM cofilin, 50 nM capping protein, 150 nM Arp2/3, 1 µM GST-pVCA-SspB-mCherry, 1 µM mCherry-SspB-mDia1. G-buffer: 2 mM Tris-HCl (pH 7.5), 0.2 mM ATP, 0.1 mM CaCl2, 0.5 mM DTT, 1 mM NaN3. KMEI-S buffer: .10mM imidazole (pH 7.0), 50mM KCl, 1mM MgCl2, 1mM EGTA, 240 mM sucrose (sucrose was added to mimic the buffer conditions in GUV experiments). (C–F) Pyrene actin polymerization assay. The reactions were performed with 2 µM actin (5% pyrene labeled) at RT. (C, D) 10 nM Arp2/3, and 100 nM NPFs. (-) represents actin and Arp2/3 only condition. (E) The reactions were performed with the indicated factors. (F) 50 nM capping protein, 150 nM Arp2/3, 3 µM profilin, 1 µM mCherry-SspB-mDia1, 1 µM GST-pVCA-SspB-mCherry. (-) represents actin only condition.

Figure S9

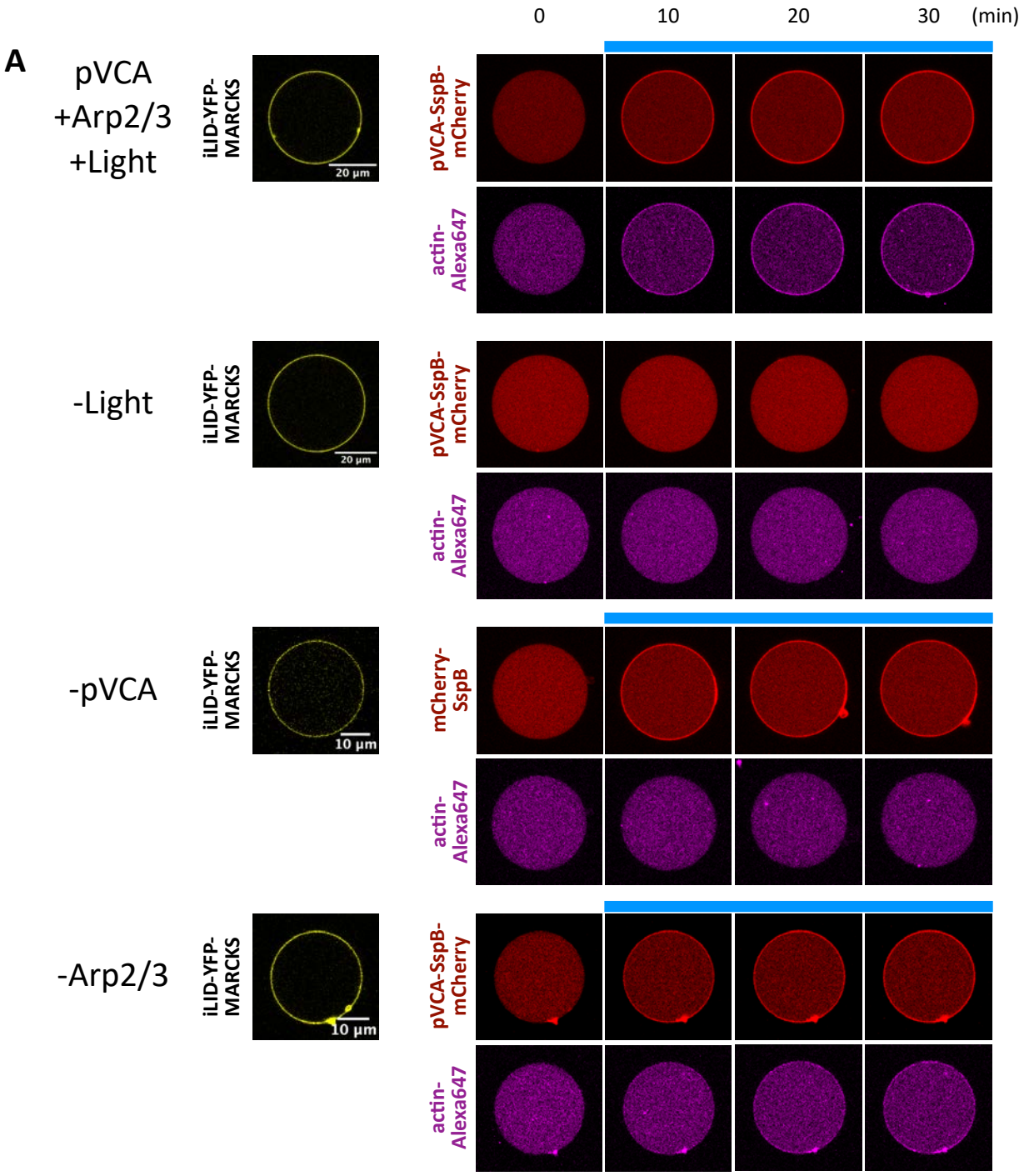

Fig. S9. Light control of actin cytoskeleton with pVCA-SspB-mCherry. The data correspond to Fig. 2C–E. (+) condition contains 15 µM iLID-YFP-MARCKS, 4.2 µM pVCA-SspB(nano)-mCherry, 7.5 µM actin (10% Alexa 647 labelled), 150 nM Arp2/3, 100 nM capping protein, 3 µM profilin, 4 µM cofilin, and 1 mM ATP. In (-light) and (-Arp2/3) conditions, blue light illumination or Arp2/3 was omitted from (+pVCA +Arp2/3 +Light) condition, respectively. In (-pVCA) condition, pVCA-SspB(nano)-mCherry was replaced with mCherry-SspB(micro).

Figure S10

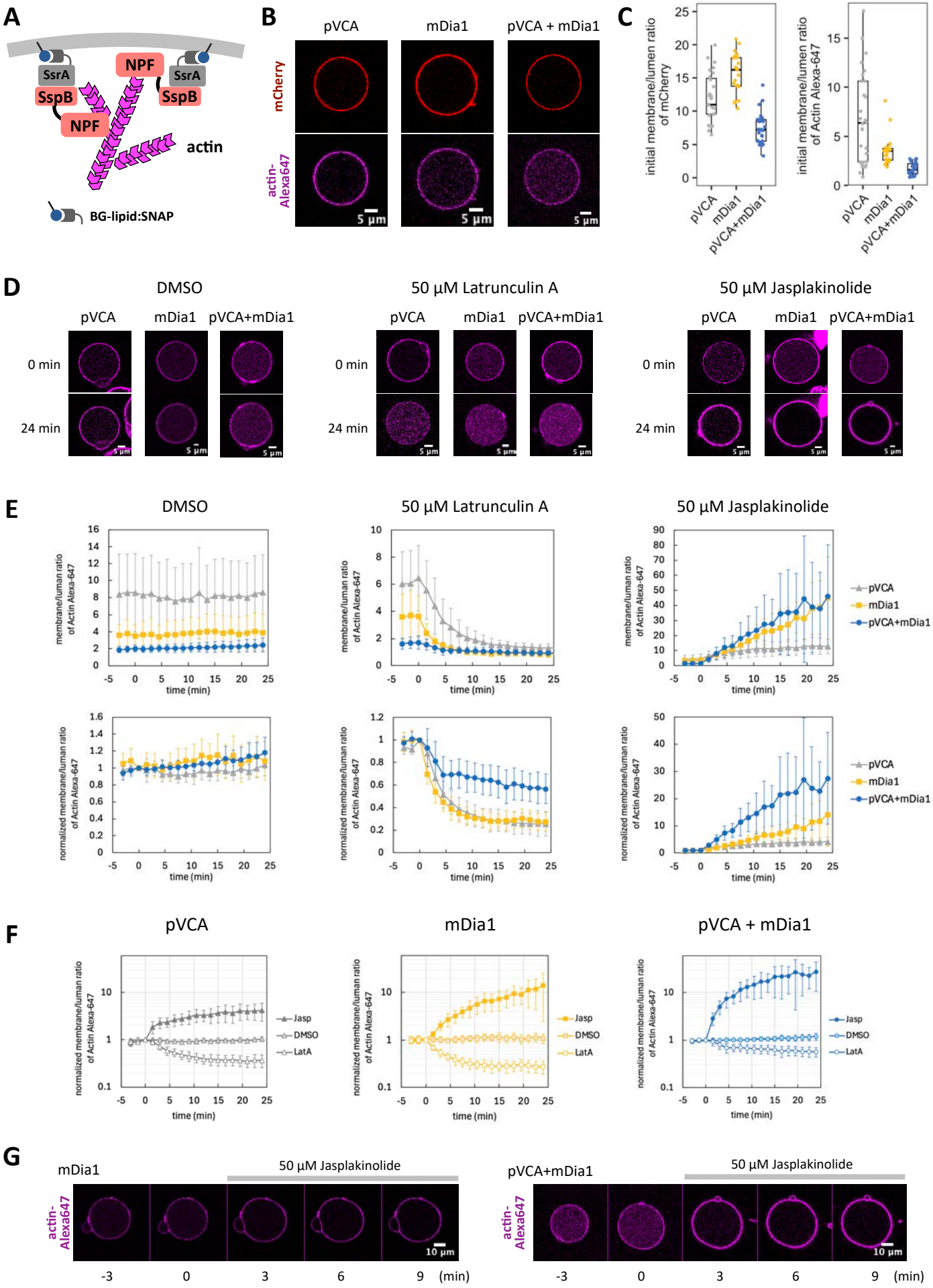
A
SsrA
SspB
NPF
NPF
SsrA
SspB
actin
BG-lipid:SNAP
B
pVCA
mDia1
pVCA + mDia1
mCherry
actin-Alexa647
5 µm
C
initial membrane/lumen ratio of mCherry
initial membrane/lumen ratio of Actin Alexa-647
pVCA
mDia1
pVCA+mDia1
D
DMSO
50 µM Latrunculin A
50 µM Jasplakinolide
pVCA
mDia1
pVCA+mDia1
0 min
24 min
E
DMSO
50 µM Latrunculin A
50 µM Jasplakinolide
membrane/luman ratio of Actin Alexa-647
normalized membrane/luman ratio of Actin Alexa-647
time (min)
pVCA
mDia1
pVCA+mDia1
F
pVCA
mDia1
pVCA + mDia1
normalized membrane/luman ratio of Actin Alexa-647
time (min)
Jasp
DMSO
LatA
G
mDia1
50 µM Jasplakinolide
pVCA+mDia1
50 µM Jasplakinolide
actin-Alexa647
10 µm
-3
0
3
6
9
(min)

fig. S10. Pharmacological perturbation of membrane-associated actin assemblies. (A) Schematic representation of constitutive tethering of NPFs. SspB-fused NPFs (pVCA and/or mDia1) were tethered to the GUV membrane via the SsrA–SNAP/BG-lipid system. (B) Representative confocal images of membrane-associated actin assemblies formed by pVCA, mDia1, or their combination. Scale bars, 5 µm. (C) Quantification of the initial membrane/lumen fluorescence intensity ratio for mCherry and actin Alexa-647. pVCA: n=27 vesicles. mDia1: n=23 vesicles. pVCA + mDia1: n=27 vesicles. Box whisker plots represent median, 1st, 3rd quartiles and 1.5×inter-quartile range. (D) Representative images before (0 min) and after (24 min) treatment with DMSO, 50 µM Latrunculin A, or 50 µM Jasplakinolide. Scale bars, 5 µm. (E) Time courses of membrane/lumen ratio and normalized membrane/lumen ratio of actin Alexa-647. (F) Time courses of normalized membrane/lumen ratio of actin Alexa-647 for each NPF condition. The y-axis is shown on a logarithmic scale. (E, F) Error bars indicate 95% CI. (G) Representative images showing membrane deformation after Jasplakinolide treatment. Scale bars, 10 µm. mCherry-SspB-mDia1-6×His was used as mDia1 in this figure.

Figure S11

A

	pVCA	Arp2/3	mDia1	actin	profilin	cofilin	capping protein	SsrA-SNAP		mCherry FRAP	Alexa 647 FRAP
pVCA/Arp2/3 + prof/cof/CP	+	+			+	+	+	+		n=9	-
pVCA/Arp2/3 + prof/cof/CP + actin	+	+		+	+	+	+	+		n=10	n=13
pVCA/Arp2/3 + actin	+	+		+				+		n=7	n=8
mDia1 + prof/cof			+		+	+		+		n=9	-
mDia1 + prof/cof + actin			+	+	+	+		+		n=6	n=8
pVCA/Arp2/3 + mDia1 + prof/cof/CP + actin	+	+	+	+	+	+	+	+		n=6	n=10

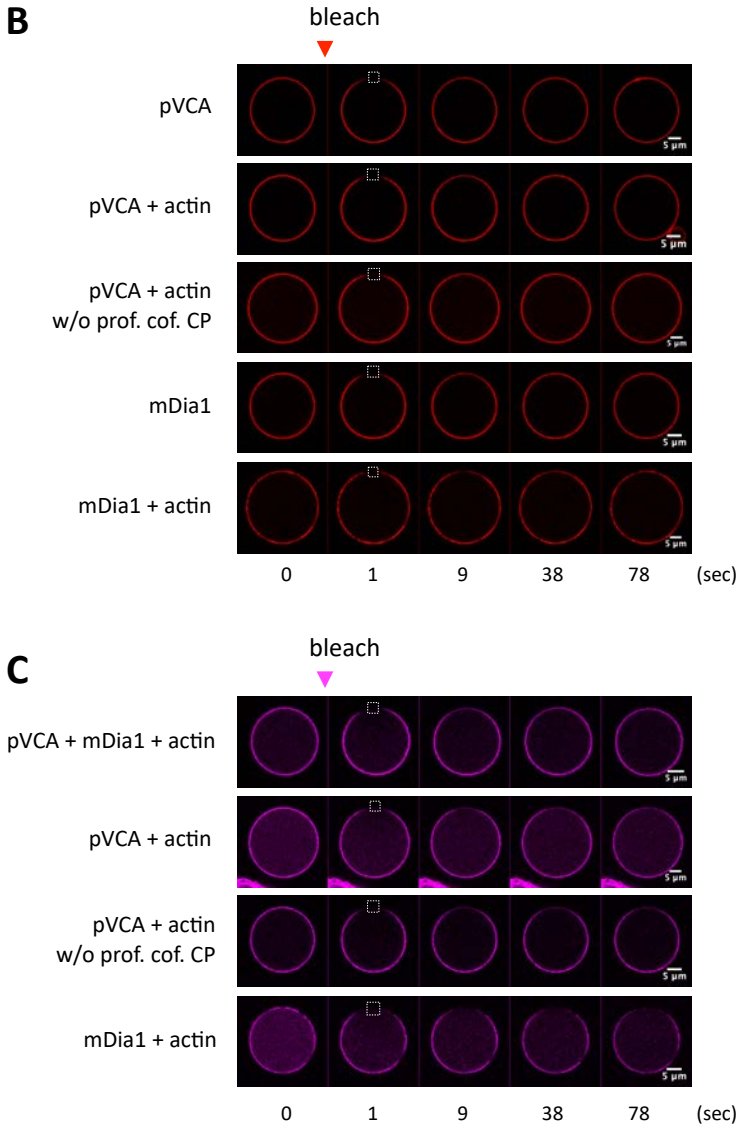

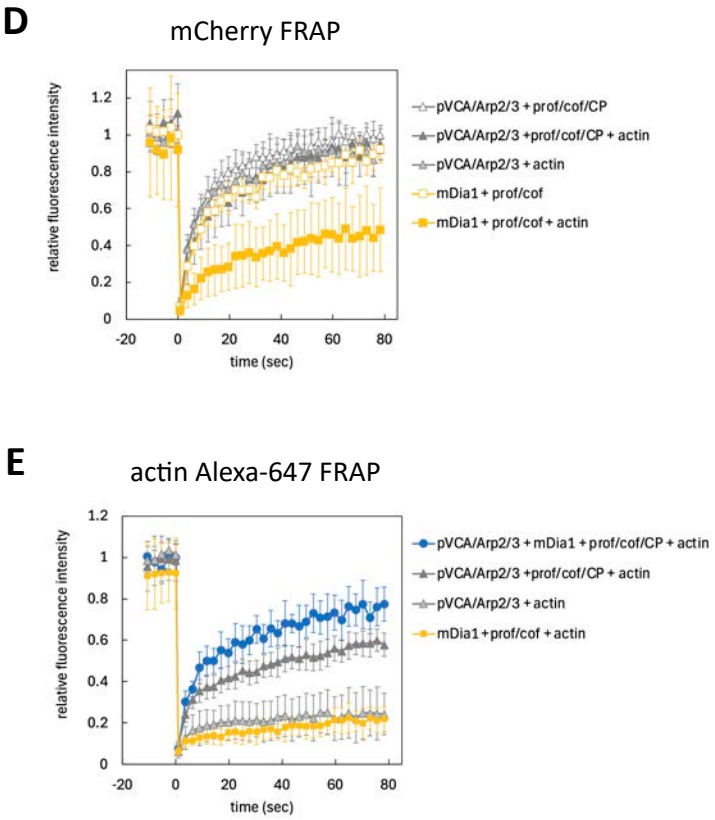

fig. S11. fluorescence recovery after photobleaching (FRAP) analysis of membrane-associated NPFs and actin. (A) Summary table of proteins included in each conditions. In FRAP analysis, SspB-fused NPFs (pVCA and/or mDia1) were tethered to the GUV membrane via the SsrA–SNAP/BG-lipid system. (B, C) Representative confocal images of mCherry-tagged NPFs and actin Alexa-647. The white dashed box indicates the photobleached region. Scale bars, 5 µm. (D, E) Time course of mCherry and Alexa-647 fluorescence recovery at the bleached region. Fluorescence intensities were normalized to those of a non-bleached region to compensate for photobleaching during image acquisition. A subset of data also presented in Fig. G.

Figure S12

A **SUVs only**
(98 mol% POPC, 2 mol% 18:1 PE-PEG2000-benzylguanine)

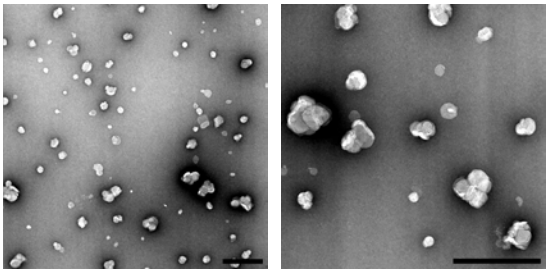

B **pVCA** (pVCA, Arp2/3, CP, profilin, cofilin) ×10 dilution

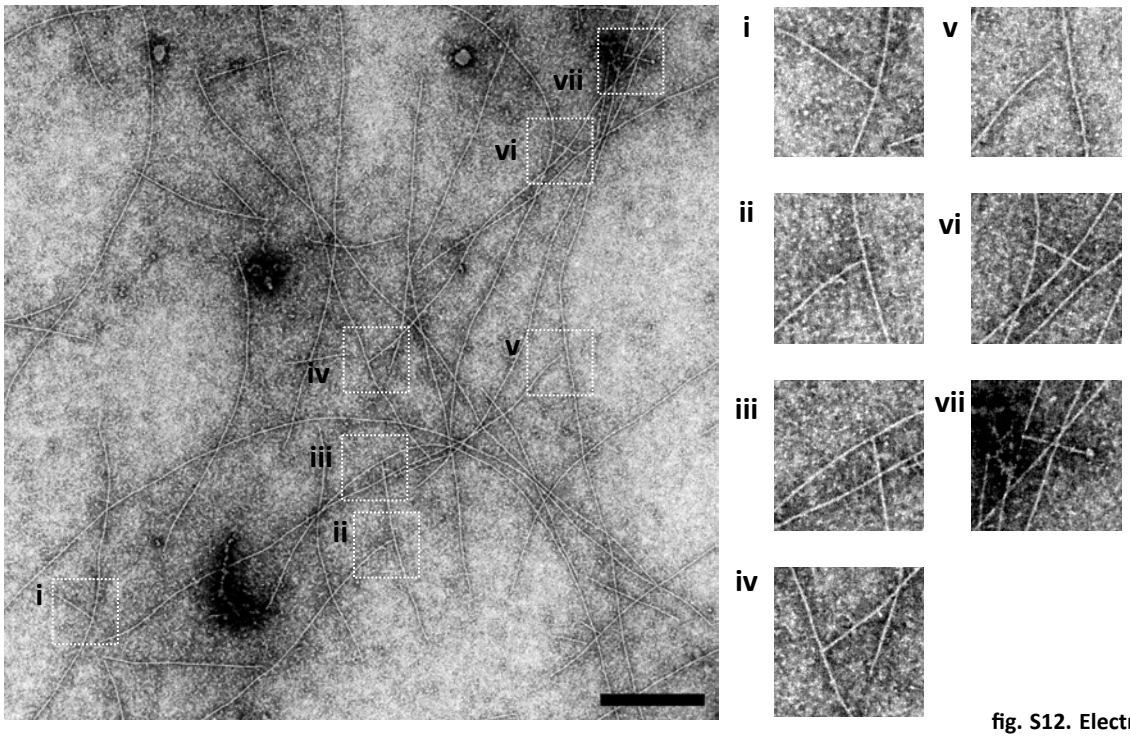

C **pVCA negative control** (Arp2/3, CP, profilin, cofilin) ×10 dilution

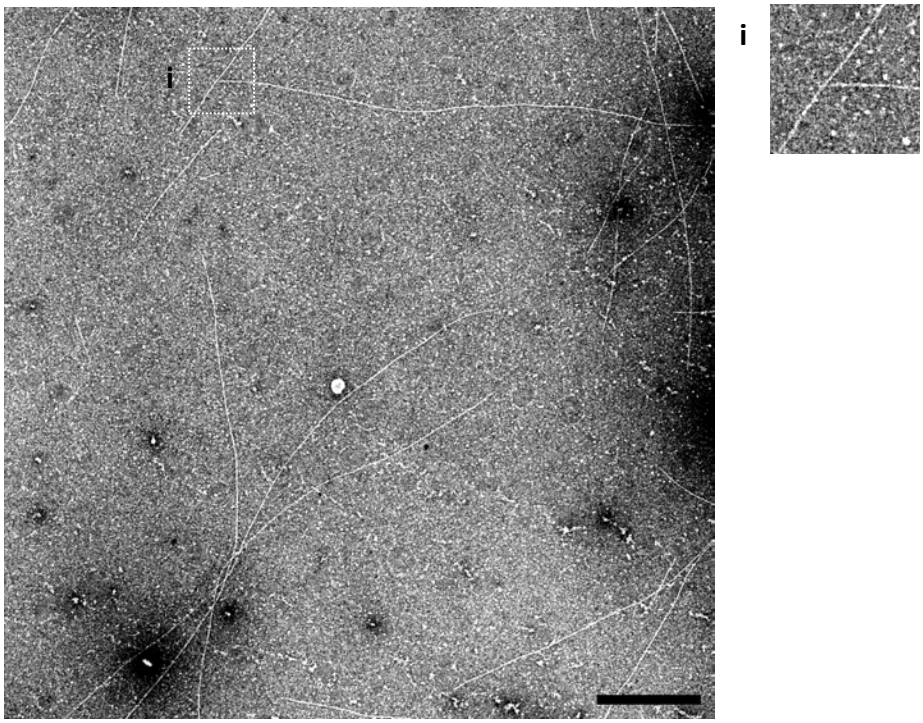

fig. S12. Electron microscopy (EM) analysis of actin filaments. Ultrastructure of small unilamellar vesicles (SUVs) and actin filaments were analyzed by negative staining electron microscopy. (A) Representative EM images of SUVs alone. (B) Representative images of Y-junctions formed in the presence of pVCA, Arp2/3, capping protein (CP), profilin, and cofilin. (C) Negative control sample lacking pVCA (Arp2/3, CP, profilin, and cofilin only). (B, C) To reduce filament overlap, the polymerization reactions were diluted 10-fold prior to deposition onto EM grids. (D) Representative EM images of actin assemblies formed with pVCA or the corresponding negative control lacking pVCA. (E) Representative EM images of actin assemblies formed with pVCA + mDia1, mDia1 alone, or the corresponding negative control lacking mDia1. All samples were deposited onto EM grids and negatively stained prior to imaging. Scale bars are shown in each panel. mCherry-SspB-mDia1-6×His was used as mDia1 in this figure.

D

pVCA (pVCA, Arp2/3, CP, profilin, cofilin)

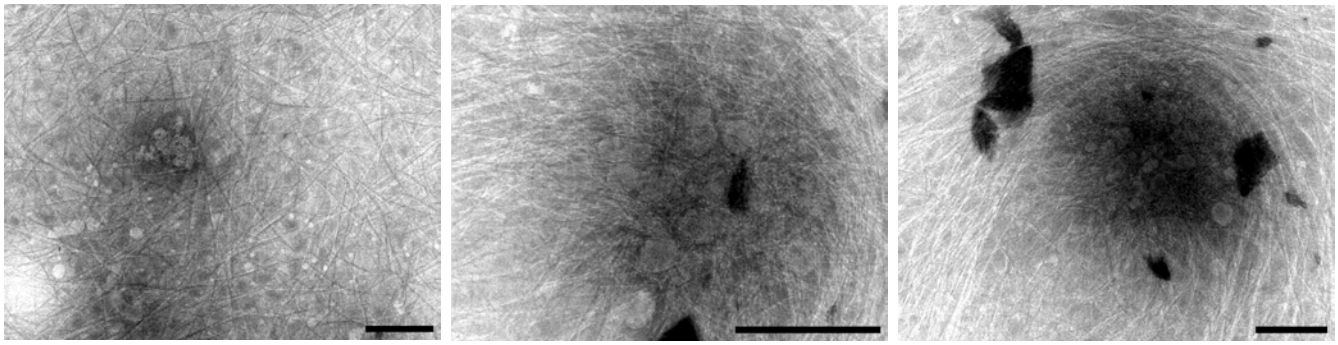

pVCA negative control (Arp2/3, CP, profilin, cofilin)

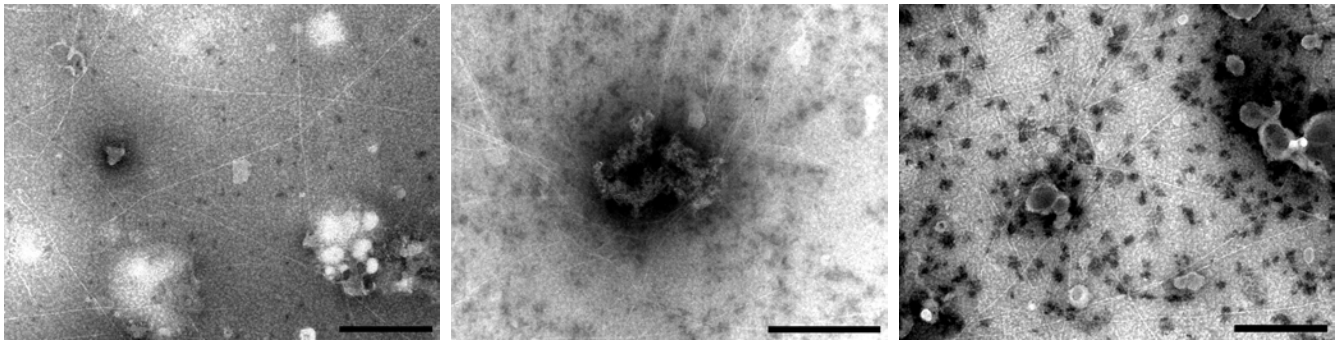

E

pVCA + mDia1 (pVCA, mDia1, Arp2/3, CP, profilin, cofilin)

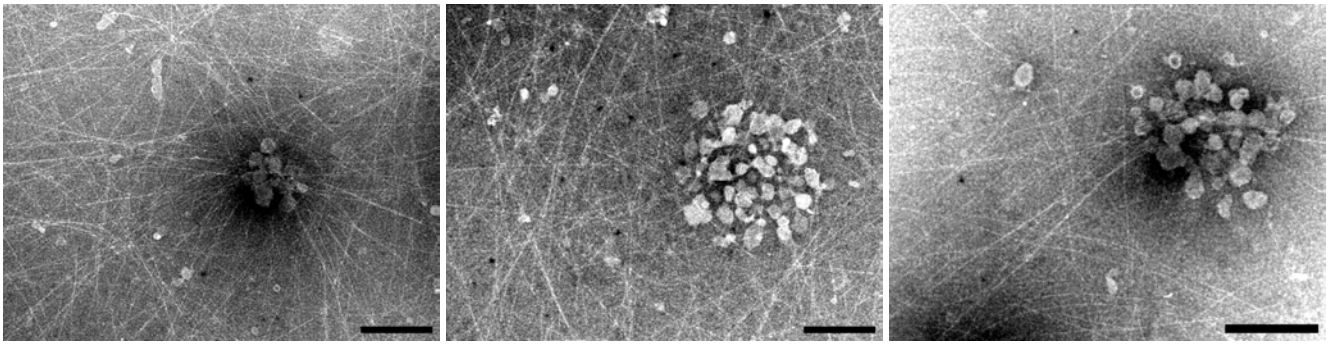

mDia1 (mDia1, profilin, cofilin)

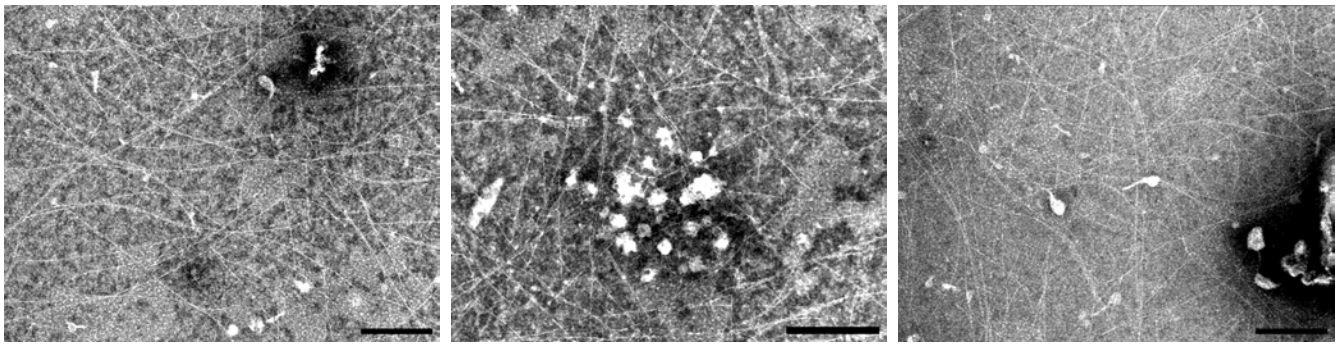

mDia1 negative control (profilin, cofilin)

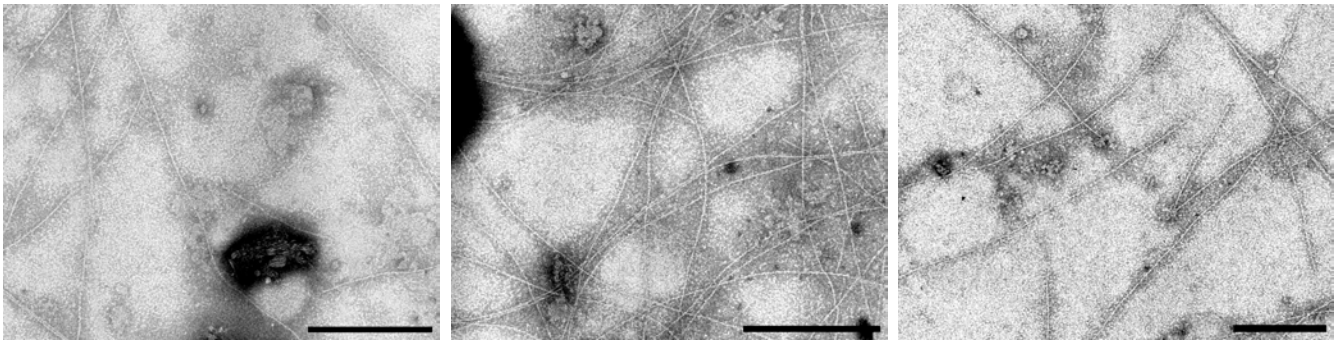

Figure S13

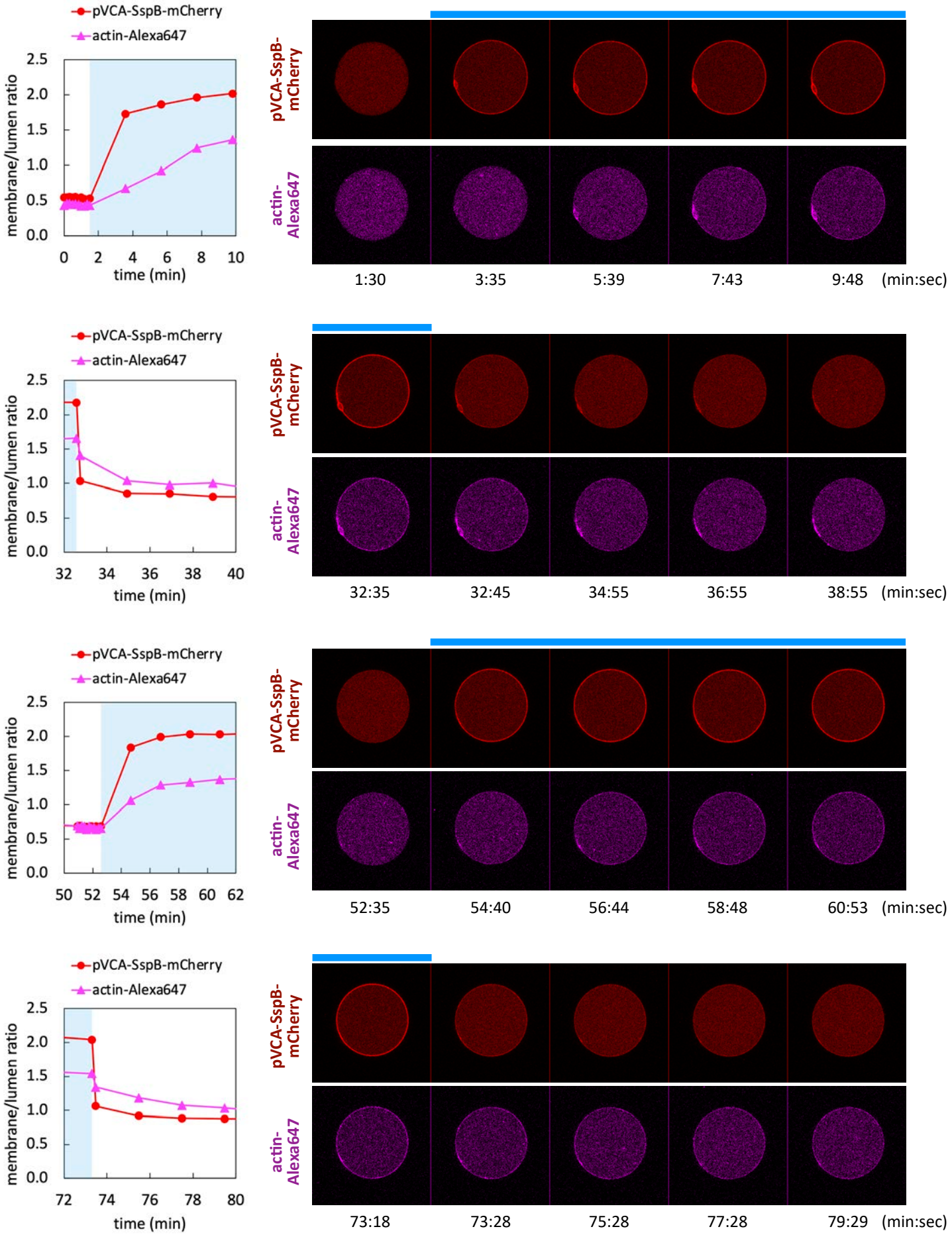
pVCA-SspB-mCherry
actin-Alexa647
membrane/lumen ratio
time (min)
pVCA-SspB-mCherry
actin-Alexa647
1:30
3:35
5:39
7:43
9:48
(min:sec)
32:35
32:45
34:55
36:55
38:55
52:35
54:40
56:44
58:48
60:53
73:18
73:28
75:28
77:28
79:29

Figure S13

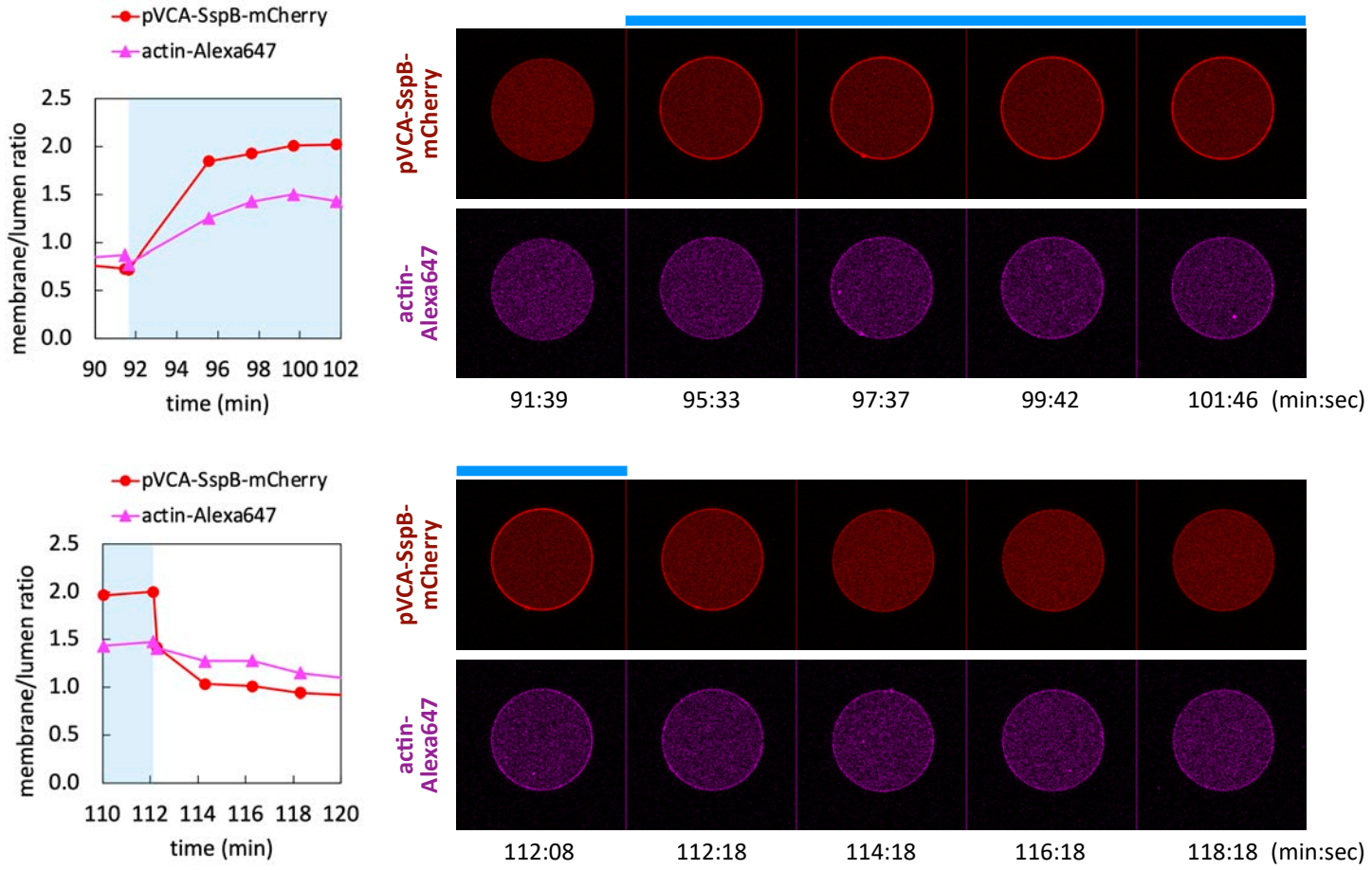

Fig. S13. Representative images of reversible actin polymerization. Confocal images and time course of membrane/lumen ratio of pVCA-SspB-mCherry and Alexa 647-labeld actin. Blue bars on images and blue regions in graphs indicate timepoints with blue light illumination. This figure corresponds with Fig. 2F, G.

Figure S14

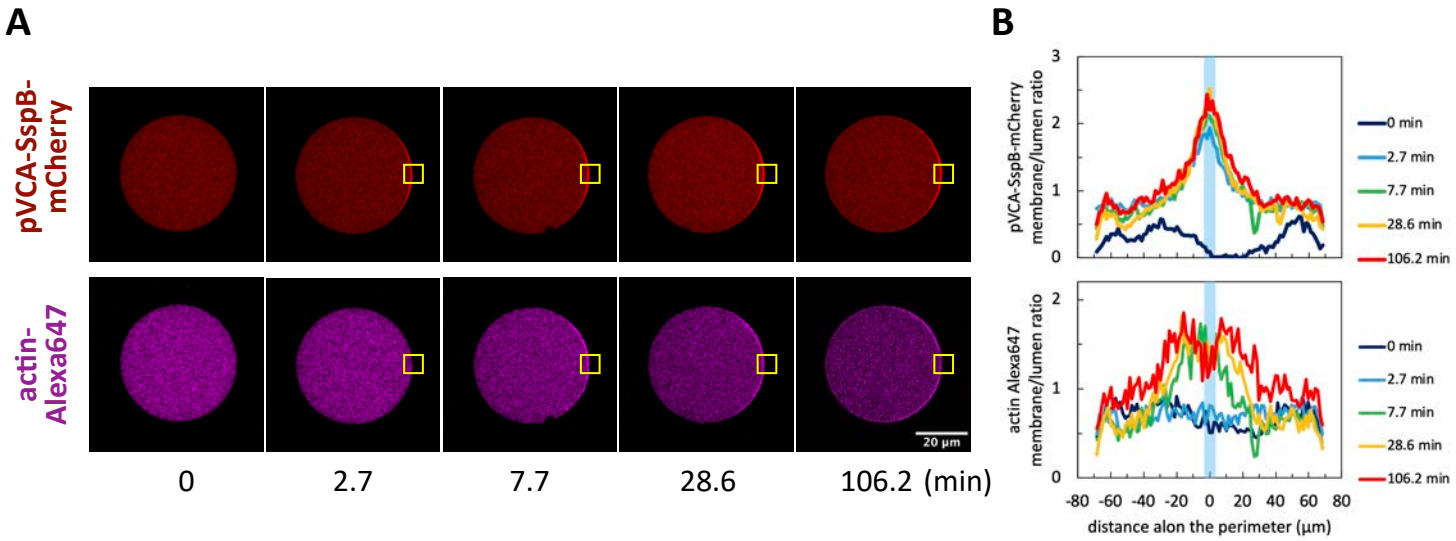

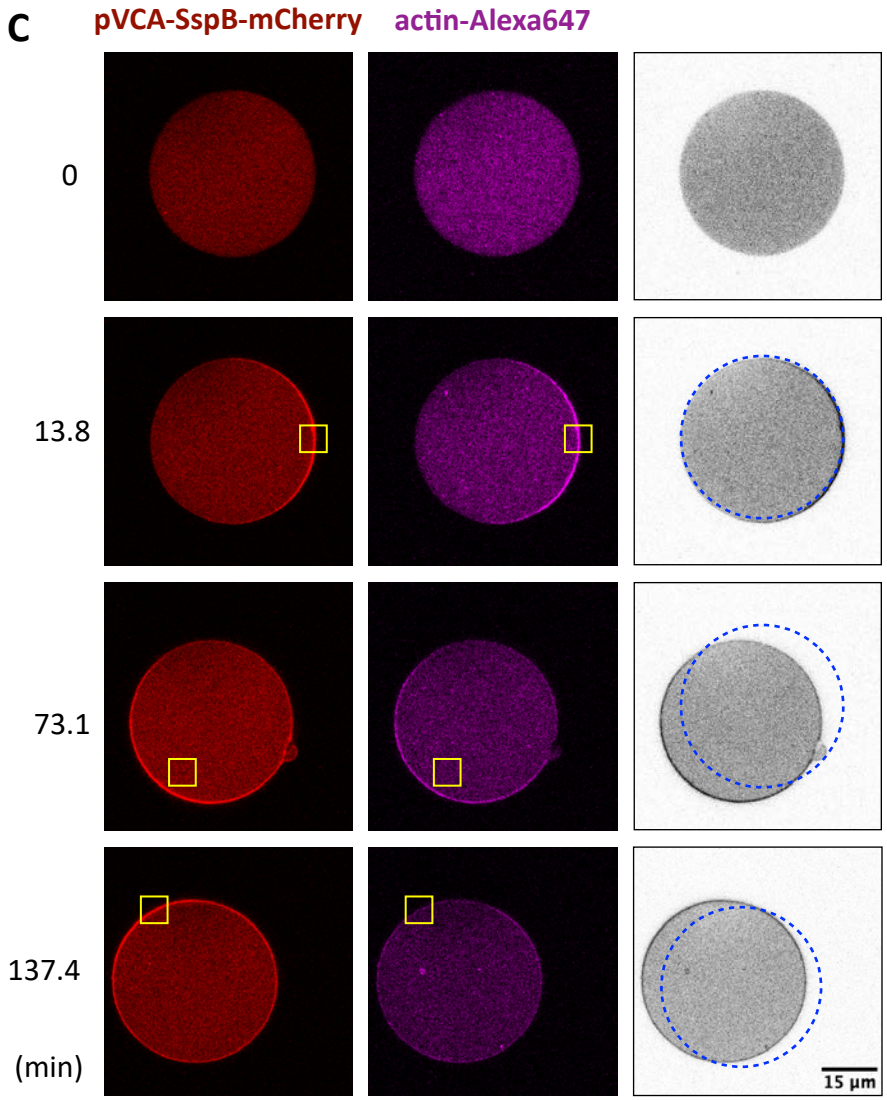

fig. S14. Asymmetric actin polymerization induced by pVCA. (A) Confocal images of local pVCA recruitment and actin polymerization. Yellow boxes indicate areas of blue light illumination. (B) Membrane/ lumen ratio of mCherry-tagged pVCA and actin Alexa-647 for the images in (A). The distance is measured from the center of blue light illumination along the perimeter of the GUV. (A, B) The data corresponds to Fig. 3B and C. (C) Confocal images of local pVCA recruitment accompanied by vesicle movement toward light stimulation. Gray scaled images were created by averaging pVCA and actin images. Dotted circles indicate positions of vesicles in the images of one above.

Figure S15

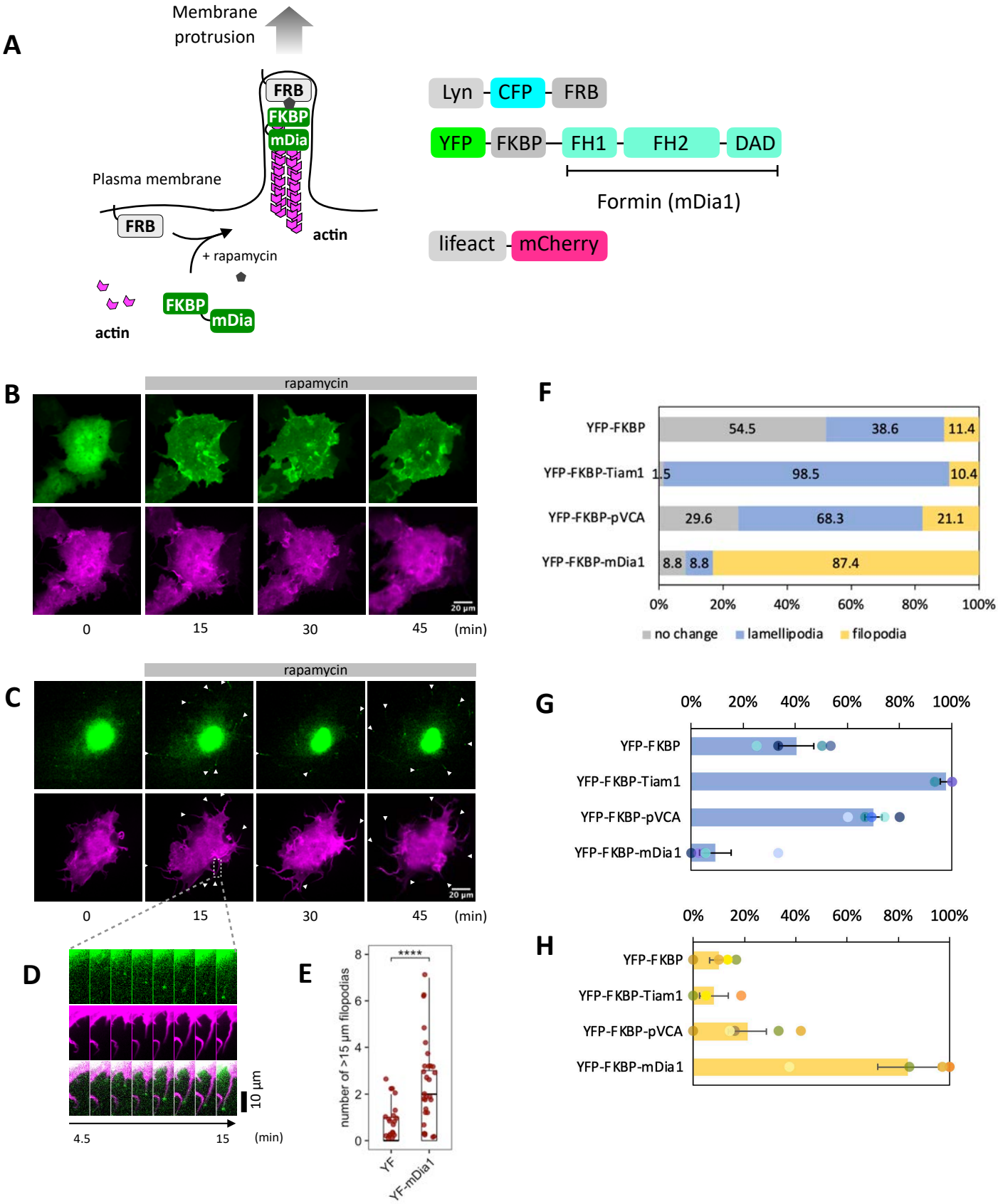

Fig. S15. Quantitative analysis of mDia1-induced filopodia formation in Cos7 cells. (A) Schematic representation of chemically-inducible mDia1 translocation and membrane protrusions. (B, C) Confocal images of plasma membrane recruitment of mDia1 and subsequent filopodia formation. Cos7 cells were transfected with Lyn-ECFP-FRB, Lifeact-mCherry, and either of YFP-FKBP or YFP-FKBP-mDia1. At time 0, 100 nM rapamycin was added. Green: YFP-FKBP or YFP-FKBP-mDia1. Magenta: Lifeact-mCherry. (B) YFP-FKBP control. (C) YFP-FKBP-mDia1. (D) Zoomed-up view of filopodia extension. Images were acquired every 1.5 minutes. The bottom is merged image. (E) Quantification of mDia1-induced filopodia. Number of filopodia whose length is longer than 15 µm was counted. Box whisker plots represent median, 1st, 3rd quartiles and 1.5×inter-quartile range. P-values: ****: < 0.0001. Wilcoxon rank sum test. YF (YFP-FKBP): n=36 cells. YF-mDia1 (YFP-FKBP-mDia1): n=33 cells. (F–H) Quantification of the phenotypes observed after plasma membrane translocation of mDia1 (n=159 cells), pVCA (n=142 cells), Tiam1 (Rac1 GEF) (n=67 cells), and control protein YFP-FKBP (n=44 cells).

Figure S16

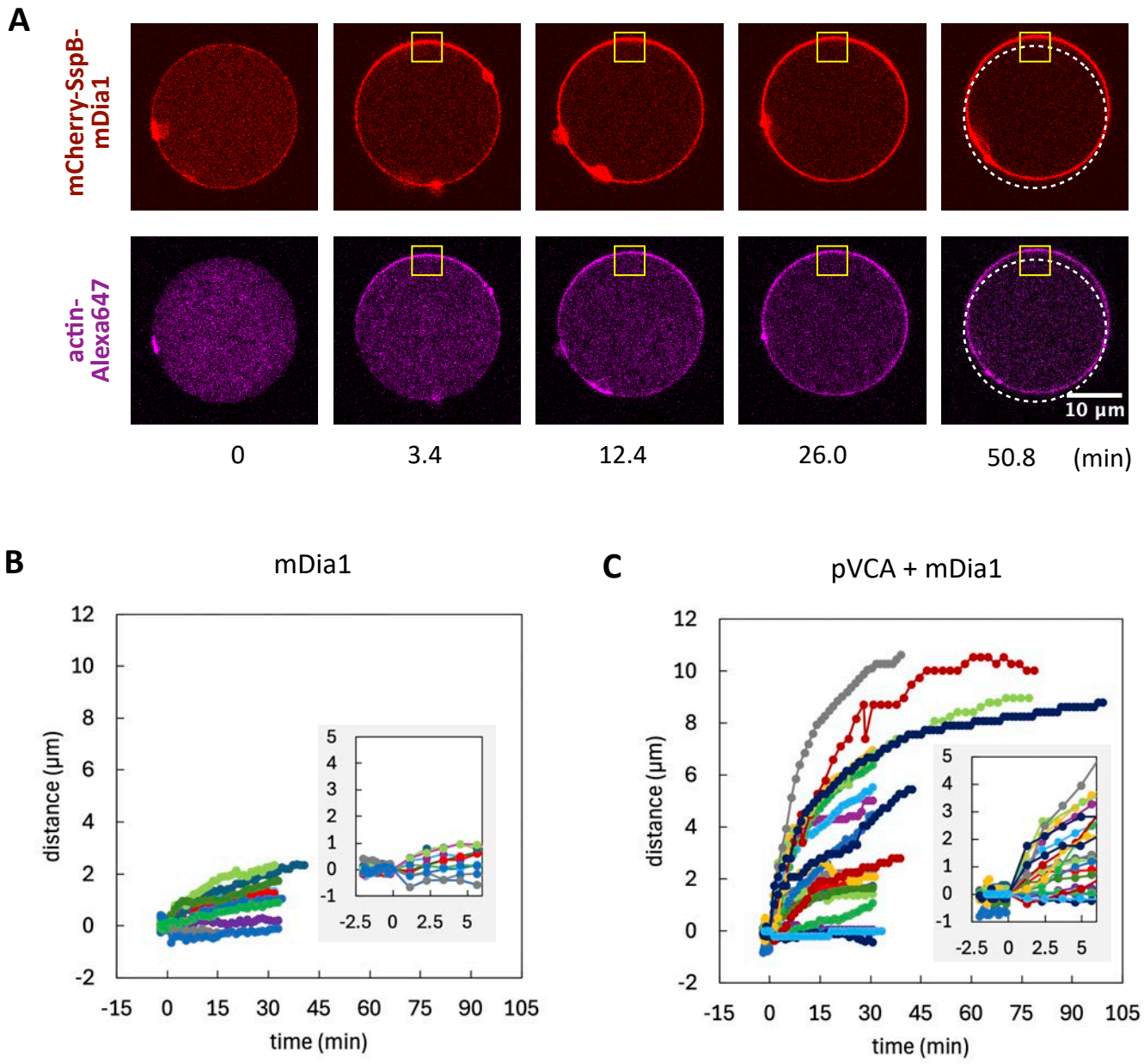

Fig. S16. mDia1-mediated GUV movement and the comparison between mDia1 and pVCA + mDia1 system. (A) Representative images of mDia1-mediated GUV movement. Yellow boxes indicate the area of blue light stimulation. Dotted lines indicate the initial position of the GUV. (B, C) Time course of the distance the front (illuminated) side of GUV membrane moved forward. Each line represents each GUVs. Insets show the initial response.

Figure S17

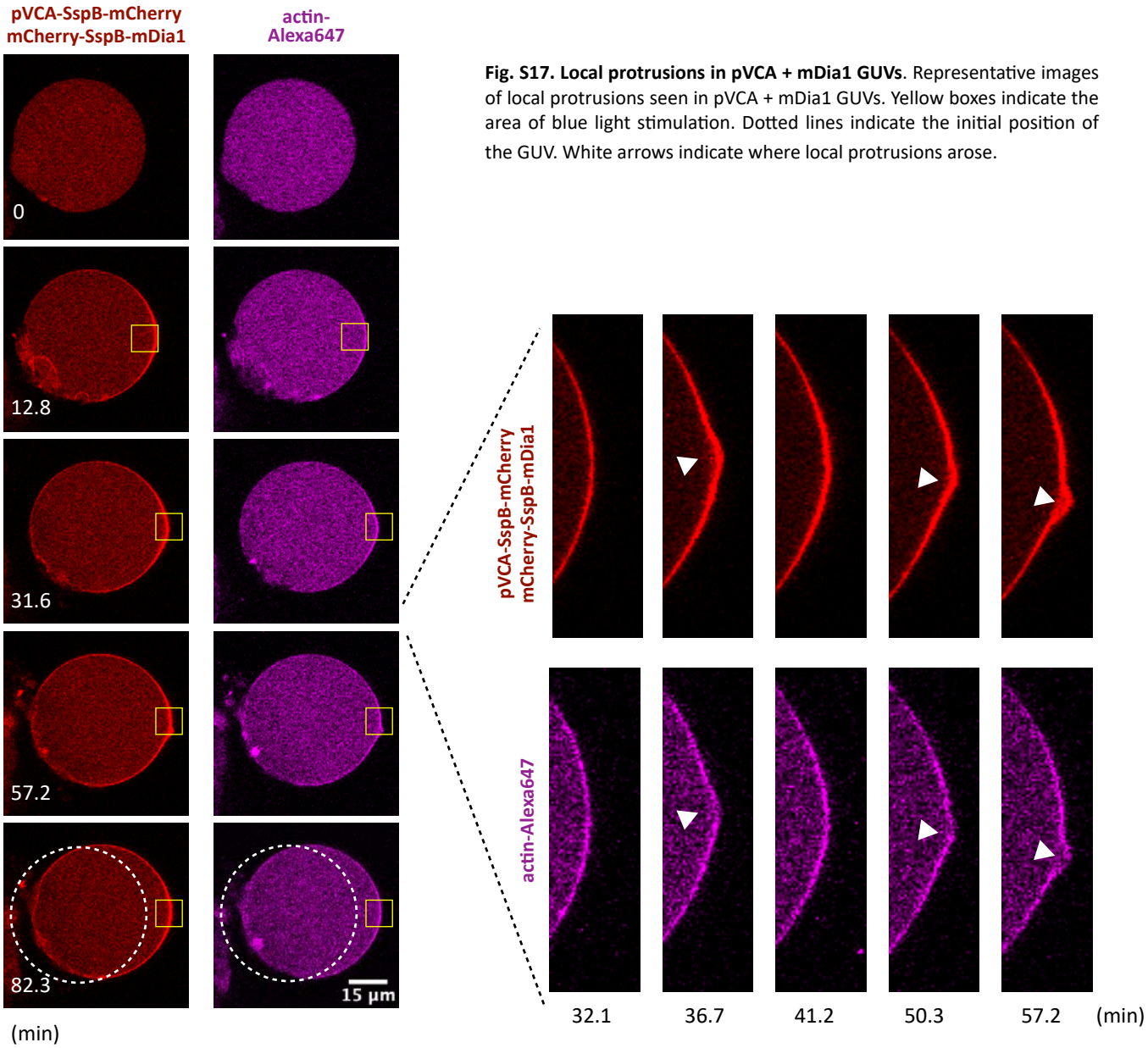

Fig. S17. Local protrusions in pVCA + mDia1 GUVs. Representative images of local protrusions seen in pVCA + mDia1 GUVs. Yellow boxes indicate the area of blue light stimulation. Dotted lines indicate the initial position of the GUV. White arrows indicate where local protrusions arose.

Figure S18

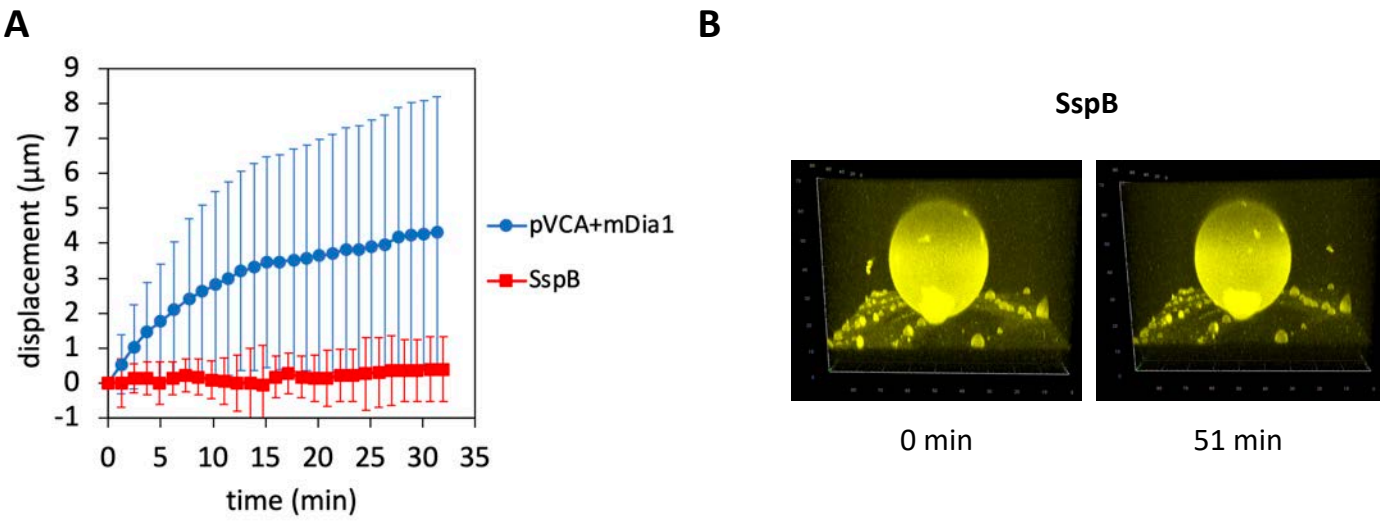

Fig. S18. Lack of vesicle movement and shape change with mCherry-SspB. With pVCA-SspB-mCherry and mCherry-SspB-mDia1 being replaced with mCherry-SspB, GUVs neither moved nor changed their shape after blue light illumination. (A) Time course of the distance the front (illuminated) side of GUV membrane moved forward. pVCA + mDia1 GUVs: n=6 vesicle. SspB GUVs: n=4 vesicles. Error bars indicate 95% CI. (B) 3D reconstitution of iLID-YFP-SNAP images before and after blue light illumination.

Figure S19

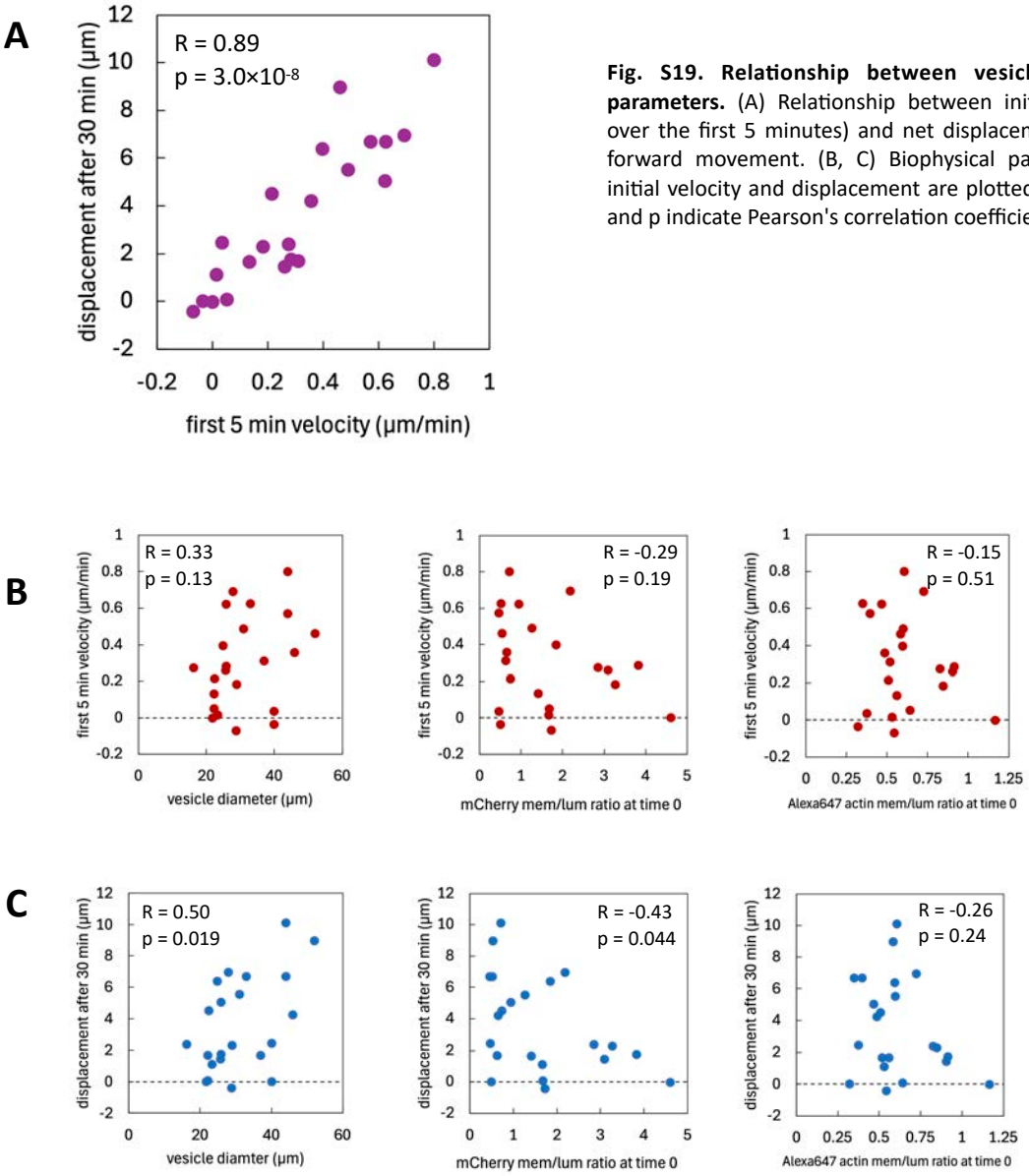

Fig. S19. Relationship between vesicle motion and biophysical parameters. (A) Relationship between initial velocity (average velocity over the first 5 minutes) and net displacement after 30 minutes of GUV forward movement. (B, C) Biophysical parameters are plotted against initial velocity and displacement are plotted in (B) and (C), respectively. R and p indicate Pearson's correlation coefficient and its p-value.

Figure S20

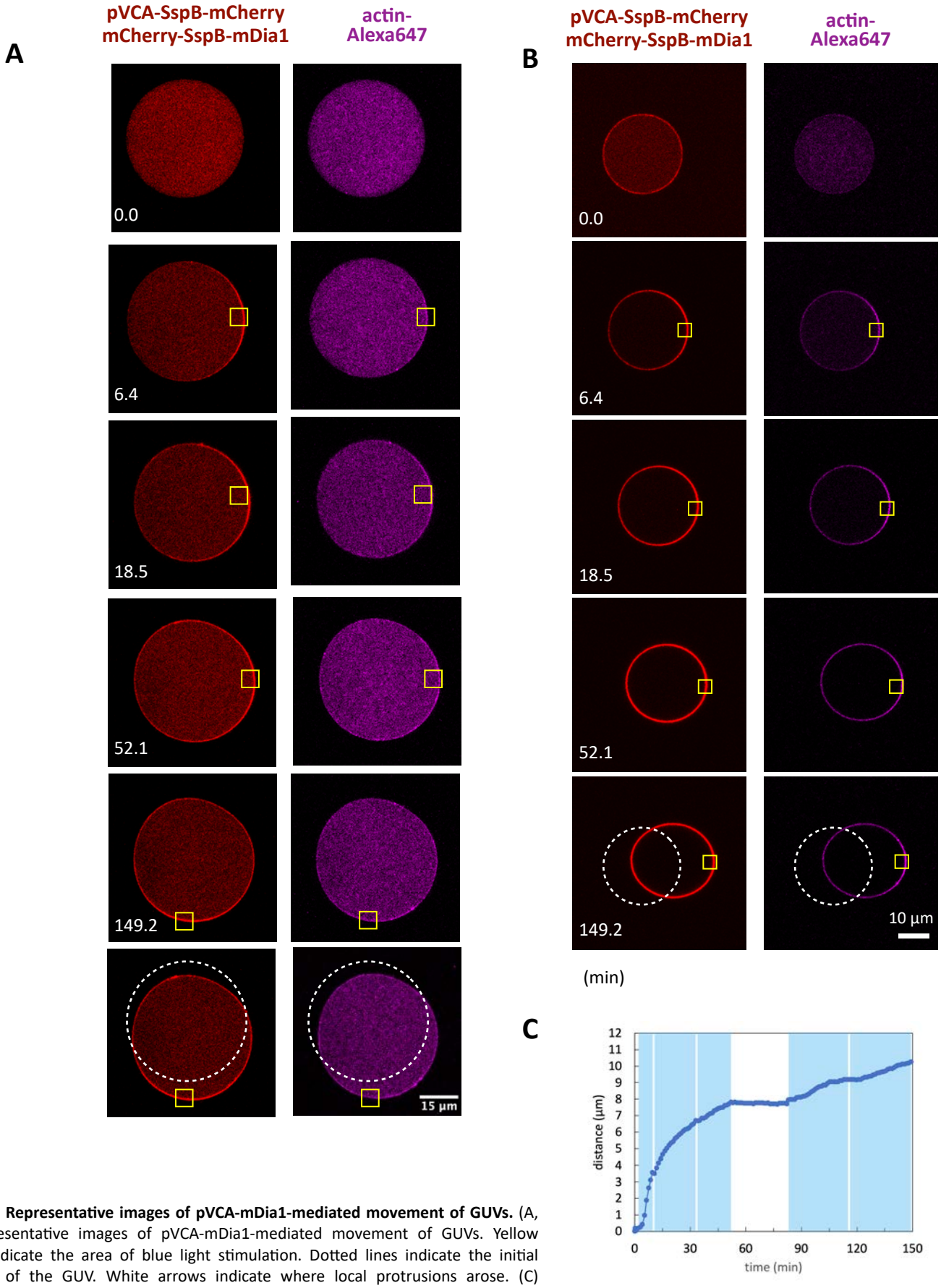

Fig. S20. Representative images of pVCA-mDia1-mediated movement of GUVs. (A, B) Representative images of pVCA-mDia1-mediated movement of GUVs. Yellow boxes indicate the area of blue light stimulation. Dotted lines indicate the initial position of the GUV. White arrows indicate where local protrusions arose. (C) Distance the front side of GUV membrane moved forward. Data was quantified from the images of (B). Blue areas indicate the periods of blue light stimulation.

Figure S21

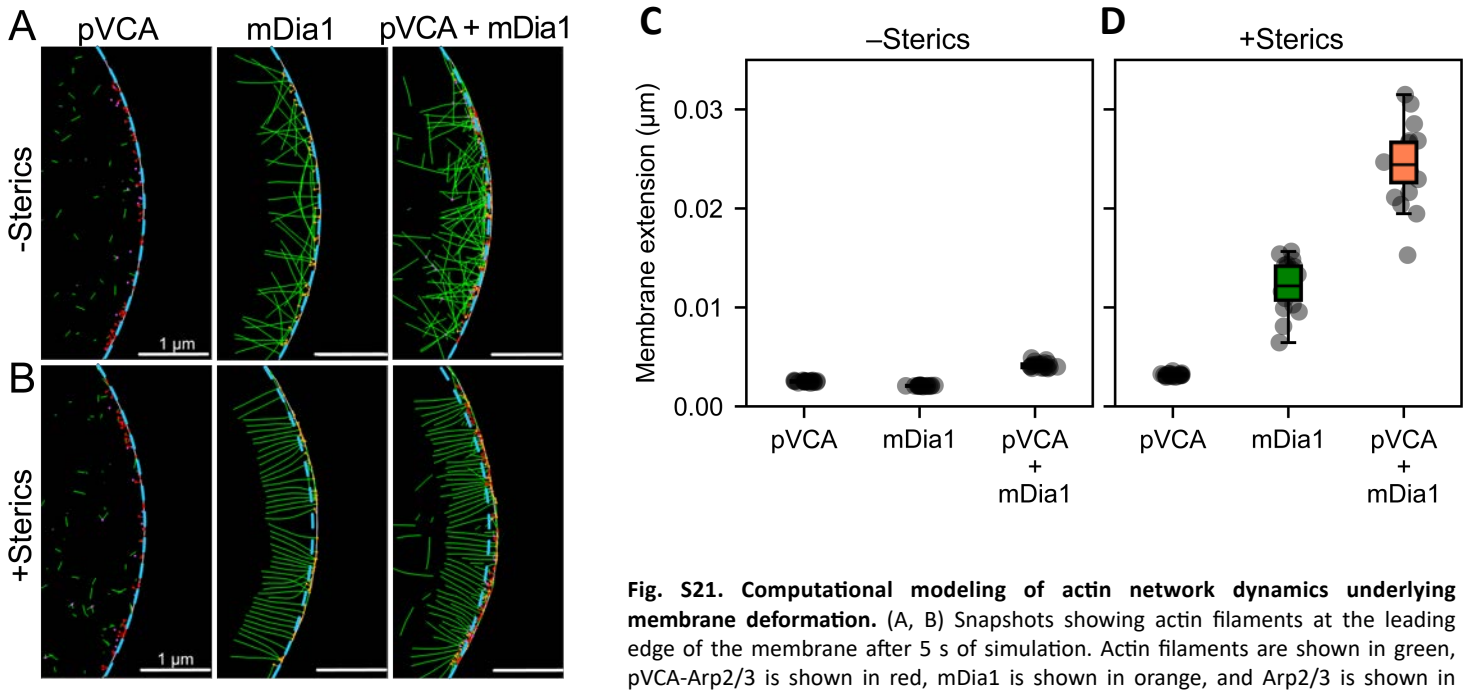

Fig. S21. Computational modeling of actin network dynamics underlying membrane deformation. (A, B) Snapshots showing actin filaments at the leading edge of the membrane after 5 s of simulation. Actin filaments are shown in green, pVCA-Arp2/3 is shown in red, mDia1 is shown in orange, and Arp2/3 is shown in magenta. The membrane location at t = 0 is shown with the cyan dotted line to highlight the extent of membrane deformation. Simulations without and with inter-filament steric interactions are shown in A and B, respectively. (C, D) Box-whisker plots showing distributions of the membrane extension for the different actin binding proteins. Results for networks without and with inter-filament steric interactions are shown in A and B, respectively. Each box plot is constructed using 20 independent simulation trajectories. Error bars represent standard deviation about the mean.